PFEIFFER VACUUM

The turbopump for photonic applications

The highest level of compression, especifically for light gases. Ideal for UHV applications.

Are you looking for a perfect vacuum solution? Please contact us:
Pfeiffer Vacuum GmbH · Germany · T +49 6441 802-0 · www.pfeiffer-vacuum.com

LASER & PHOTONICS REVIEWS
www.lpr-journal.org

Advances in Ex Situ Tissue Optical Clearing

Paweł Matryba, Leszek Kaczmarek, and Jakub Gołąb**

Examination of whole organs with subcellular resolution in health, disease, and during development is necessary to decipher their biological complexity. However, until recently, this has been virtually impossible due to the natural opacity of organ tissue. Recent progress in tissue optical clearing (TOC) has overcome this limitation by turning organs into transparent, light-permitting specimens. At least 20 original TOC methods have been developed in less than a decade, which were followed by hundreds of attempts that were aimed at their optimization and practical application. The majority of proof-of-concept studies have focused on the brain. However, it is apparent that TOC might be equally valuable when applied to peripheral organs or even the whole body. The progress in TOC for peripheral organs is delineated in an organ-by-organ fashion and whole-body clearing approaches are discussed. Additionally, physical and optical approaches for TOC affecting the optical properties of the samples and image quality are discussed to explore their advantages, limitations, and future possibilities.

1. Introduction

The importance of studying anatomy, being a key to decipher organism physiology, was already recognized by the first physicians in ancient Egypt and Greece and continuously accepted thereafter, as encapsulated by the words of Jean François Fernel, a French renaissance physician: "Anatomy is to physiology as geography is to history; it describes the theatre of events."[1] Thus far, the knowledge of the structure of organs and tissues mainly progressed due to two general approaches: histological examination and gross imaging techniques, such as magnetic resonance imaging (MRI), positron emission or computed tomography (CT). While gross imaging techniques allow for intravital imaging and are indispensable in both research and everyday medical practice, their spatial resolution is modest and as yet not reaching the cellular resolution.[2,3] In contrast, a wide spectrum of routine histological procedures allows for precise imaging of subcellular structures. However, examination of micrometer thick tissue slices lacks spatial context and might often contribute to incomplete or inaccurate description. Serial histology followed by reconstruction of 2D sections aims at generating detailed images of the entire organs. Yet, it provides a view that is limited to one cutting plane and one round of staining, and furthermore, is time-consuming and arduous to perform in the not state-of-the-art research facilities. Moreover, it is not free from artifacts generated during the process of tissue slicing.[4,5]

The gap between high spatial versus cellular resolution was recently filled by modern tissue optical clearing (TOC) techniques (greatly supported by development of light sheet fluorescence microscopy, LSFM[6]), the goal of which is to transform tissue into translucent specimen, suitable to perform optical, instead of physical, sectioning and therefore to image the entire organ, while preserving its structure.[7] Based on the chemicals used, the TOC methods were first classified by Richardson and Lichtman[8] into solvent-based, aqueous-based, and hydrogel embedding techniques. This was later extended in Silvestri's taxonomy nominating four main categories of: organic solvents, hyperhydrating solutions, high-refractive index aqueous solutions, and tissue transforming techniques,[9] the classification that covers all of the existing techniques. Recently, Yu et al.[10] proposed a scheme for application of TOC based on the size and age of the animal. TOC can be also classified into techniques for either ex situ or in vivo clearing, with the latter being extensively utilized for in vivo brain, skin, and blood flow imaging research,[11–14] and where pioneering studies relied on the application of glucose,[15,16] glycerol,[17] or dimethyl sulfoxide (DMSO)[18] as the optical clearing agents (OCAs). Progress in this vibrant research area was recently discussed in comprehensive reviews by Genina et al.[19] and Bashkatov et al.[20]

The first TOC methods for fixed, dissected samples were developed and optimized solely for the nervous tissue[21–26] (**Figure 1**) and this trend of introducing novel techniques by exhibiting their applications to brain research is still evident.[27–31] Nervous tissue also served as a reference point for thorough reviews regarding chemical properties of TOC.[7,8,32–34] However, it was shortly revealed that organs other than the brain might benefit from

P. Matryba, J. Gołąb
Department of Immunology
Medical University of Warsaw
5 Nielubowicza Street, 02-097 Warsaw, Poland
E-mail: p.matryba@nencki.gov.pl; jakub.golab@wum.edu.pl
P. Matryba, L. Kaczmarek
Laboratory of Neurobiology
BRAINCITY, Nencki Institute of Experimental Biology of Polish Academy of Sciences
Pasteura 3, 02–093 Warsaw, Poland

The ORCID identification number(s) for the author(s) of this article can be found under https://doi.org/10.1002/lpor.201800292

DOI: 10.1002/lpor.201800292

applying TOC, the apogee of which was demonstrated by introduction of whole-body clearing protocols opening novel avenues for studying systemic diseases within the entire, unsectioned organism with cellular resolution.[35–40]

Here, we aim to update TOC taxonomy and present approaches either implemented or specifically developed for ex situ imaging of peripheral organs, in an organ-by-organ fashion. First, we begin with an overview of pioneer methods of either clearing category that are organic solvents, hyperhydrating solutions, high-refractive index aqueous solutions, and tissue transforming techniques, their general limitations, and advantages. Next, we discuss how physical and optical approaches to TOC affect optical properties of the sample and image quality. Finally, we present TOC adopted for particular organs and whole-body clearing and close by presenting riveting applications of OCAs, which expand the TOC utility beyond animal tissues. We hope that this literature analysis will help to systematize briskly developing area of TOC and give the researchers a clear view on to what extent TOC can be applied to their studied organ of interest, its limitations, and will therefore be helpful in selecting a proper approach from the plethora of already available methods.

Paweł Matryba is a Ph.D. student at the Medical University of Warsaw. Since 2013, he has been involved in projects focused on development and optimization of tissue-clearing techniques. His active projects aim to decipher T-cell-mediated immunity within cleared organs of the immune system.

Leszek Kaczmarek is a professor of neurobiology at the Nencki Institute, Warsaw, Poland. His research aims to understand the brain–mind connection. At the molecular and cellular levels, a phenomenon named synaptic plasticity appears to provide plausible explanation for those phenomena.

Jakub Gołąb is a professor of immunology and head of the Department of Immunology at the Medical University of Warsaw. His research interests involve mechanisms of tumor immunosurveillance and, in particular, identification of novel mechanisms that mitigate the antitumor effects of T cells. Additional areas of his research include photodynamic therapy of cancer and the use of monoclonal antibodies.

2. Approaches to TOC

As thoroughly reviewed by Richardson and Lichtman,[8] there are multiple factors obstructing light penetration through biological specimens, that is, the presence of light scatterers (mainly lipids, cytoskeleton, collagen, and elastin fibers) and absorbers (heme, melanin, lipofuscin), their inhomogeneous distribution and differences of refractive indices (RI) between tissue compartments. However, successful application of TOC requires that the researchers find a balance between effective elimination of the mentioned factors and preservation of tissue integrity, fluorescence of endogenously encoded fluorophores and even light-scattering lipids, when, for example, whole brain tracing of individual axons is desired. Moreover, the imaging medium must be highly transmissive to laser light itself. Therefore, numerous approaches were already proposed to meet those criteria while enhancing optical properties of tissues.

2.1. Overview of the Original TOC Techniques

2.1.1. Organic Solvents

Solvent-based clearing relying on sample dehydration in alcohol gradient and further sample incubation in RI matching solution composed of methyl salicylate, benzyl benzoate and wintergreen oil, was first proposed by Spalteholz in 1911.[41] Additionally, to decrease light absorption by endogenous pigments, a bleaching step of pigments oxidation with hydrogen peroxide was introduced. This general strategy endured for more than a century with slight, but essential, modifications.

Andrew Murray developed the formula of improved RI matching solution consisting of 1:2 mixture of benzyl alcohol:benzyl benzoate (BABB, aka Murray's Clear), the utility of which for the clearing of *Xenopus* embryos was tested by Dent et al.,[42] and which currently warrants excellent tissue transparency of the majority of murine organs.[43] Dodt's laboratory performed the first study coupling ethanol dehydration, BABB-mediated RI matching and ultramicroscopy to image whole brains of 3–5 week-old mice.[22] Inability to use this method for adult organs containing high amount of lipids stimulated the same group to introduce dichloromethane (DCM), as a delipidating agent, and tetrahydrofuran (THF) as both delipidating and dehydrating heterocyclic solvent, which allowed to study axon regeneration in the model of central nervous system injury in both young and adult mice.[23] However, as the imaging of the adult murine brain was still suboptimal, Becker et al.[44] screened a number of both dehydration and clearing agents and introduced superior clearing protocol in which BABB was replaced with dibenzyl ether (DBE) during RI-matching step. Building upon this chemical combination, Ertürk et al.[45] described a pipeline for 3D imaging of solvent-cleared

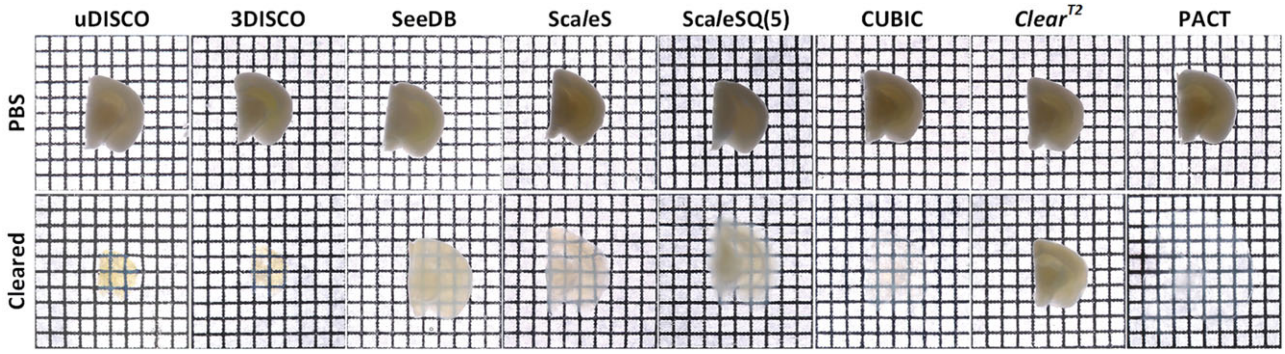

Figure 1. The vast majority of TOC methods were first developed for brain research. Typical results obtained by TOC of 2-mm-thick PFA-fixed mouse brain slices. Apparent differences in level of transparency, as inspected by eye, are correlated with delipidating capability of each method. High delipidation: uDISCO, 3DISCO, CUBIC, PACT; medium delipidation: Sca*l*eSQ(5); low or no delipidation: SeeDB, Sca*l*eS, Clear^{T2}. Grid width: 1.45 mm. Reproduced under the terms of the CC-BY Creative Commons Attribution 3.0 Unported license (https://creativecommons.org/licenses/by/3.0/).[337] Copyright 2018, The Authors. Published by SPIE.

organs (3DISCO) and achieved remarkable transparency of not only adult brains, but also other peripheral organs such as lung, lymph node, or mammary gland.

A few additional limitations of solvent-based technique remained to be answered at that time, mainly rapid decay of fluorescence signal (which restrained clearing of transgenic animals harboring less robust fluorophores) and immunolabeling of large, millimeter-to-centimeter wide samples. The first issue was resolved in FluoClearBABB method described by Schwarz et al.,[46] who showed that replacement of ethanol/THF by 1-propanol and especially *tert*-butanol with a fixed, alkaline pH, provides superior stability of fluorophores over weeks-to-months (vs 1–2 days for most 3DISCO-treated samples). Although the exact explanation of *tert*-butanol-mediated fluorescence stability was not provided, we believe this should be attributed to kosmotropic nature of this alcohol, which stabilizes intramolecular interactions in proteins and thus offers milder process of dehydration when compared with small molecules of either methanol or ethanol[47] that can easily penetrate, and thus degrade, many proteins.[48] Moreover, *tert*-butanol is unique among other organic solvents as it preserves proteins, rather than denaturing them,[48] with the intriguing exception of hemoglobin denaturation.[49]

The issue of insufficient immunolabeling was addressed in iDISCO (immunolabeling-enabled 3DISCO) method by Renier et al.,[50] who achieved complete immunolabeling of adult mouse brain within 2–3 weeks, when additional methanol pretreatment and permeabilization steps were performed prior to delipidation and clearing. iDISCO immunolabeling along with its tuned formula, iDISCO+,[51] are a robust protocols applicable to whole-mount staining and imaging even of human embryos and fetuses.[52] By building upon FluoClearBABB, Pan et al.[36] presented ultimate DISCO (uDISCO) whole-body clearing in which a dehydrating agent, *tert*-butanol, was pumped through circulatory system of the sacrificed animal. Two prominent features of uDISCO are: 1) significant, up to 65% reduction of organ volume, which is essential for whole-body LSFM imaging, and 2) robust preservation of transgenically expressed fluorescent proteins (XFPs), achieved not by alkalization of solutions (as in original FluoClearBABB), but by replacing standard BABB with BABB-D, a mix of BABB, diphenyl ether and scavenger of peroxides—tocopherol. A group led by Dan Zhu has recently reported that application of alkaline dehydrating agents (THF or *tert*-butanol) as well as alkaline RI-matching BABB-D, along with incubations and sample storage performed at 4 °C, might increase fluorescent signal preservation even further.[53,54] Orderly screening resulted in description of FDISCO—a protocol that relies on sample dehydration with alkaline (pH 9.0) THF and DBE-mediated RI-matching. With all of the steps performed at 4 °C, such design allows for substantially better preservation of many tested fluorescent proteins and chemical fluorescent tracers.[54] These complex relations between chemicals used in each organic solvent method are depicted in **Figure 2**.

In aggregate, it is currently possible to perform solvent-based clearing which will: 1) yield remarkable transparency, 2) preserve XFPs fluorescent signal, 3) allow whole-mount immunostaining, and 4) be completed within hours to days. On the other hand, such clearing prevents analysis of lipids, which are being dissolved during the procedure and relies on handling of toxic chemicals which are also hazardous for microscopic glues and therefore sample imaging requires specific mounting approaches. To allow even further unobstructed imaging, recent protocols couple blood decolorizing agents with subsequent application of organic solvents,[39,55] with new approaches being still under investigation for heme-rich tissues.[56] Although the issue of toxicity was recently resolved by application of ethyl cinnamate (food flavor) as RI matching and imaging solution,[57] its application was first presented for kidney and will be further discussed in Section 3.14.

2.1.2. Hyperhydrating Solutions

Serendipitous observation that 4 M urea makes polyvinylidene fluoride membranes transparent led to a pioneering work by Hama et al.,[24] who proposed the idea of tissue hyperhydration, instead of solvent-based dehydration, to homogenize its microenvironment and finally decrease scattering of light. Conscientious screening of other chemicals, in addition to urea, resulted in development of Sca*l*e, a method opening at that time a new avenue for studying murine brain connectomics and embryos with robust green fluorescent protein (GFP) signal

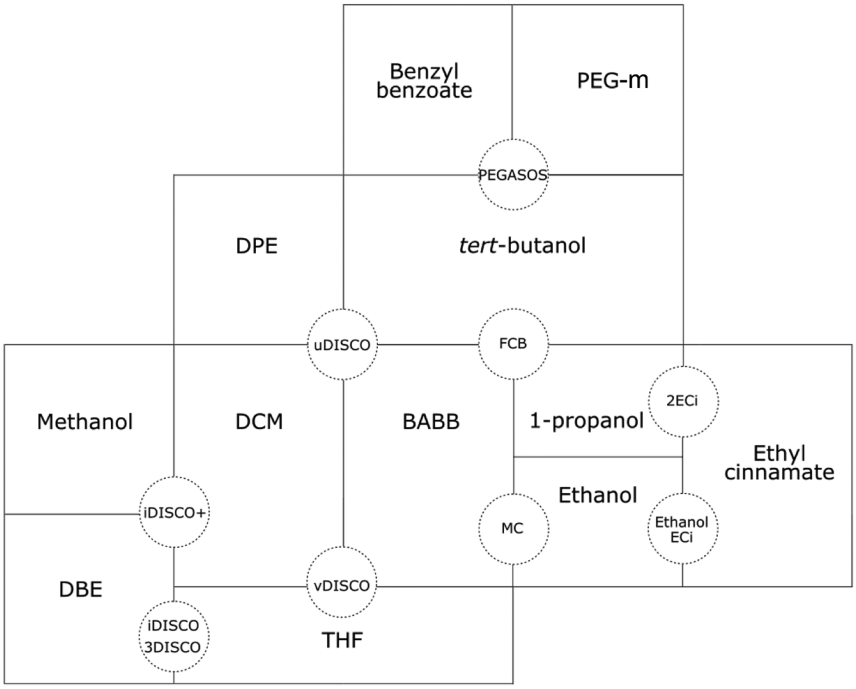

Figure 2. Relations between organic-solvent TOC methods. Names of the main chemicals that are used in each method are indicated in the center of each block (methanol, DBE, etc.). Names of the methods are provided in the circles. All of the chemicals in contact with dashed lines are used in the indicated method; for example, DBE, DCM, and THF are utilized in 3DISCO and iDISCO methods. FCB, FluoClearBABB; MC, Murray's clear; PEG-m, poly(ethylene glycol) methacrylate/poly(ethylene glycol) diacrylate; 2ECi, 2nd generation of ECi. See the text for the remaining abbreviations.

preservation and feasible immunolabeling. The main limitations of the original Sca*l*e that remained, were the time of incubation (ranging from days to 6 months for embryonic day E13.5 mouse embryos) and, although isotropic, significant tissue expansion (which doubled tissue volume). Both of these were, at least partially, addressed by the following study by Susaki et al.,[26] who again performed profound screening of chemicals and, using Sca*l*e as a scaffold, described CUBIC pipeline (*c*lear, *u*nobstructed *b*rain *i*maging *c*ocktails and *c*omputational analysis). Shortly after, the same group observed one of the CUBIC constituents (*N*,*N*,*N*′,*N*′-tetrakis(2-hydroxypropyl)ethylenediamine, Quadrol) to effectively elute endogenous chromophores, mainly heme,[58] which granted successful clearing and imaging of blood-rich organs such as heart and spleen, even whole body of adult mouse.[59] Formerly depicted limitations were also addressed by Hama et al.,[60] who presented upgraded Sca*l*e to preserve integrity of brain tissue structure—Sca*l*eS, in which the urea-driven hyperhydration is compensated by dehydration caused by sorbitol, resulting in almost negligible size alteration. When compared with CUBIC, the authors claimed Sca*l*eS to better preserve both fluorescence intensity and tissue microstructure, as confirmed by post-clearing transmission electron microscopy (TEM), the observation which might be attributable to difference in Triton X-100 concentration between these methods (15% vs 0.2%, respectively). Recently, a group led by Ueda performed additional comprehensive screening of chemicals and reported even more potent palette of reagent cocktails for delipidation, decoloring, RI matching, decalcification and controlled tissue expansion.[61,62]

Clear^{T} and Clear^{T2} are yet other hyperhydrating approaches, that rely on tissue incubation in formamide gradient. The main advantages of both of these protocols include short clearing time, taking minutes-to-hours for embryos, and abandoning of detergents/solvents making them compatible with lipophilic dyes.[63] Although the utility of Clear$^{T/T2}$ for TOC of dissected adult organs is limited and requires further optimization,[28] application of such mild clearing agent that does not disrupt the sample, might be beneficial for the assessment of drugs distribution to spheroids or their cellular death upon the treatment.[64,65]

To summarize, hyperhydrating TOC methods utilize non-toxic compounds, are compatible with immunolabeling, in general prevent both quenching of fluorescently tagged proteins and significant tissue deformation. In addition, CUBIC is characterized by its decolorizing capability. The major drawbacks of such remain modest transparency (when compared with solvent-based cleared specimens) and relatively long incubation times taking days to weeks to complete.

2.1.3. Tissue Transforming Methods

Tissue embedding in acrylamide/bisacrylamide solution, proposed by a group led by Deisseroth, results in its transformation into tissue-hydrogel matrix hybrid.[21] A technique, called CLARITY (Clear Lipid-exchanged Acrylamide-hybridized Rigid Imaging/Immunostaining/In situ hybridization-compatible Tissue-hYdrogel) relies on the formation of rigid mesh inside the tissue, which stabilizes proteins and nucleic acids,[66] while enabling subsequent removal of lipids with strong detergents, such as sodium dodecyl sulfate (SDS), which is also capable of tissue decolorization. The first proof of concept CLARITY protocol

was challenging to perform due to utilization of electrophoretic tissue clearing (ETC) for lipid extraction, resulting in a variable clearing quality and frequent heat-induced tissue damage. Since then, plenty of modifications appeared,[67–69] for example, the passive clarity technique (PACT) and perfusion-assisted agent release in situ (PARS),[38] stochastic electrotransport[70] including optimization of acrylamide, bisacrylamide and/or reaction initiator concentration,[71,72] investigation of new types of polymers to reduce relatively long passive clearing times,[73] resigning from using ETC or even skipping the step of hydrogel formation[74] and establishing inexpensive mounting media solutions, which now allow to obtain robust and scalable results.[75]

Resigning from ETC limits penetration depths for immunostaining. This issue was addressed in SWITCH method developed by Murray et al.[76] A novel idea behind SWITCH is fixation with both paraformaldehyde/glutaraldehyde and introduction of two solutions, SWITCH-off, which prevents molecules, antibodies from reacting with tissue, but allowing free diffusion of these, followed by SWITCH-on, reviving tissue's reactivity with already well-penetrated molecules. Such approach allowed the researchers to obtain durable tissue matrices and to perform 19 rounds of uniform antibody stainings in large tissue samples. Since 1) paraformaldehyde/glutaraldehyde fixation might significantly decrease signal-to-noise ratio of images (because of autofluorescent byproducts generated from glutaraldehyde) and 2) SWITCH-off is a low pH solution (prone to XFP denaturation and transcript hydrolyzation), the authors searched for another fixative based on SWITH idea that could guarantee simultaneous XFP, epitope and transcript retention. Based on the profound molecular dynamics simulations and further hands-on tests, they found polyglycerol 3-polyglycidyl ether to fulfill all of the mentioned criteria and stabilize GFP even after tissue exposure to heat at 70 °C for 24 h.[77] This new fixation method, named SHIELD (stabilization to harsh conditions via intramolecular epoxide linkages to prevent degradation) consists of three easy-to-prepare solutions (SHIELD-perfusion, -OFF and -ON) that transforms tissue into rigid samples that are later compatible with TOC. SHIELD-processed brain samples exhibit remarkable XFP and epitope retention (all of the 53 tested antibodies were compatible) and allows for successful detection of various mRNAs via fluorescence in situ hybridization while retaining high signal-to-noise ratio.

Hydrogel tissue hybridization also opens new avenues for achieving controllable tissue swelling[78] which, by increasing linear organ dimension (currently by the factor of ≈4–5 up to 20), results in expansion, super resolution microscopy.[79,80] The relations between chemicals used in tissue transforming TOC techniques are depicted in **Figure 3**.

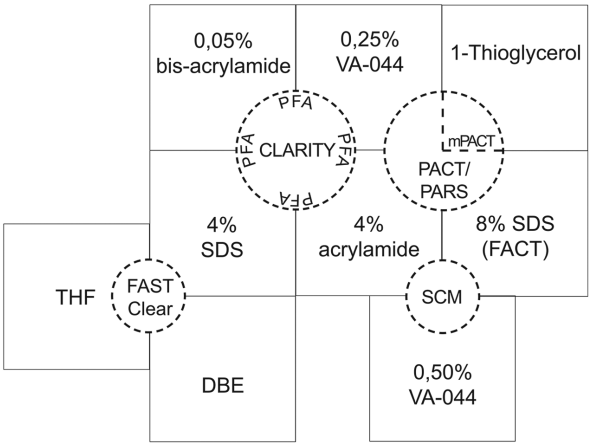

Figure 3. Relations between tissue-transformation TOC methods and their derivatives. Names of the main chemicals that are used in each method are indicated in the center of each block (SDS, acrylamide, etc.). Names of the methods are provided in in the circles. All of the chemicals in contact with a dashed line are used in the indicated method; for example, 4% acrylamide, 0.50% VA-044, and 8% SDS are utilized in SCM. Note that FACT (fast free-of-acrylamide clearing tissue) and FASTClear (free-of-acrylamide SDS-based tissue clearing) are not tissue-transformation TOC methods sensu stricto but were included as derivatives of PACT. Chemically speaking, the mPACT method is PACT with addition of 1-thioglycerol. SDS, sodium dodecyl sulfate; VA-044, 2,2′-azobis[2-(2-imidazolin-2-yl)propane]dihydrochloride, mPACT, modified PACT. See the text for the rest of abbreviations.

2.1.4. High-Refractive Index Aqueous Solutions

This heterogeneous group of TOC methods is represented by FocusClear,[81] 2-2′ thiodiethanol (TDE),[82,83] sucrose solutions,[84] SeeDB (See Deep Brain),[25] SeeDB2,[85] FRUIT,[86] UbasM (a urea-based amino-sugar mixture),[27] and C_e3D (clearing-enhanced 3D microscopy),[87] with the latter being developed specifically for lymph node tissue clearing and, therefore, will be discussed in the appropriate subsection. FocusClear is, according to the patent description, an aqueous clearing solution selected from the group consisting of DMSO, diatrizoate acid, ethylenediaminetetraacetic acid, glucamine, β-nicotinamide adenine dinucleotide phosphate, sodium diatrizoate, derivatives of polyoxyalkalene. So far, FocusClear (RI = 1.45–1.46) was used either as imaging medium for CLARITY-cleared samples or as an independent TOC solution and proved to be valuable for imaging of high variety of tissues obtained from, for example, mammals,[88] insects,[89] zebrafish,[90] plants,[91] as well as various types of biomaterials.[92] Unfortunately, the precise formula of this approach is patent-protected and as such, cannot be easily tuned for specific applications.

On the contrary, TDE is a non-viscous solvent which mixes with water well and, therefore, can reach RI between 1.33 (water) and 1.52 (pure TDE)[93] as needed. Thus, it can be used both as a clearing and a mounting medium. SeeDB, composed of increasing gradients of fructose solutions (up to 115% w/v), preserves signal from both fluorescent proteins and lipophilic neuronal tracers. Although as such, it should be perceived as a water-based, hyperhydrating method, it reaches a high RI of 1.49. Its modification, SeeDB2 goes further beyond that value, reaching RI ≈1.52 with iohexol/saponin solutions and thus allowing super-resolution mapping of neuronal connectivity.[85] FRUIT is a SeeDB variation with significant amounts of urea added to the fructose solutions. Although it clearly yields higher level of transparency, when compared with SeeDB, its performance is difficult to evaluate on the basis of the provided, limited, fluorescent imaging data.

UbasM protocol relies on two solutions, UbasM solution 1 (Ub-1) (RI ≈1.45) consisting of meglumine, urea, 1,3-dimethyl-2-imidazolidinone and small amount of Triton X-100 and UbasM

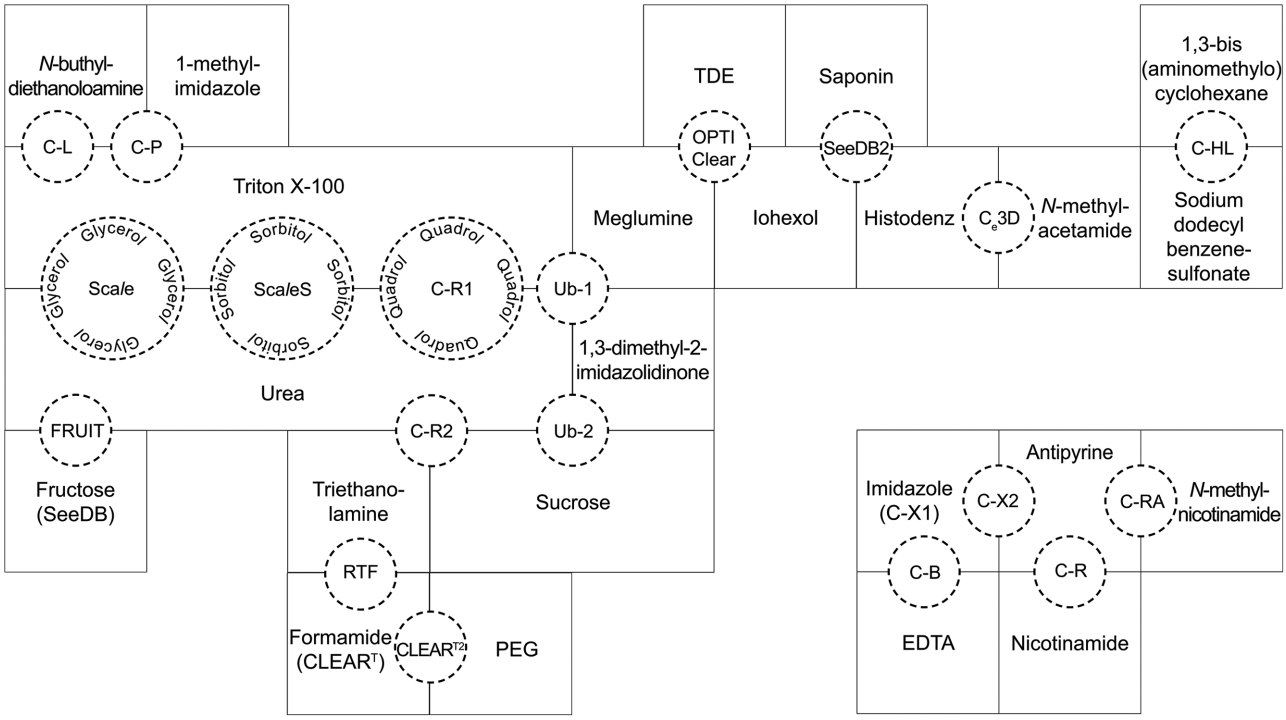

Figure 4. Relations between hyperhydrating and high-refractive-index aqueous solutions. Names of the main chemicals that are used in each method are indicated in the center of each block. Names of the methods are provided in the circles. All of the chemicals in contact with a dashed line are used in the indicated method; for example, Triton X-100, urea, and sorbitol are the main components of Sca*l*eS. Note that some of the clearing solutions consists of one chemical and these were put into a bracket; for example, SeeDB is based on gradient of fructose solutions, CUBIC-X1 is made from imidazole. RTF, rapid clearing method based on triethanolamine and formamide; C-R1, C-R2, CUBIC reagent 1 and CUBIC reagent 2; C-B, CUBIC-B for decalcification; C-P, CUBIC-P for delipidation and rapid decolorization; C-L, CUBIC-L for delipidation and decolorization; C-HL, CUBIC-HL for rapid delipidation and rapid decolorization; C-R, CUBIC R for RI matching; C-RA, CUBIC-RA for RI matching, preserves fluorescent signal better than CUBIC-R; CUBIC-X1, C-X2: CUBIC reagents for brain expansion microscopy, the first and second reagent, respectively.

solution 2 (Ub-2) (RI = 1.47–1.48) made of urea, 1,3-dimethyl-2-imidazolidinone and sucrose. While the Ub-1 contributes to significant tissue expansion (achieving ≈120–160% volume of the original sample), this effect is reversible upon PBS wash of tissue and its soaking in Ub-2 (≈95–115% volume of the original sample). When compared to CUBIC, UbasM requires similar clearing time and provides comparable fluorescent signal intensity, but results in improved preservation of membrane integrity and compatibility with lipophilic fluorescent dyes, as confirmed by comparative DiI labeling. The relations between chemicals used in both hyperhydrating and high-refractive index aqueous solutions are shown in **Figure 4**.

To conclude this overview of the all original tissue clearing methods from chemical perspective, we propose an updated taxonomy of all of the described approaches for ex situ TOC (**Figure 5**).

2.2. Physical Factors Affecting TOC

2.2.1. Temperature and Electric Field

As the first TOC studies (sucrose, BABB, Sca*l*e) relied on inherently slow diffusion of OCAs, it was reasonable to test whether increased temperature during the clearing might substantially enhance molecular movement of OCAs without introducing tissue deformation. The most detailed picture of temperature influence on TOC was examined with CLARITY-related protocols. Yu et al.[94] found almost linear positive correlation between incubation temperature and clearing time for PACT-processed 1-mm thick mouse brain slices (**Figure 6**a). Incubation at 52 and 57 °C made the samples fragile and caused a pronounced decrease in the mean GFP fluorescence, while clearing at both 42 and 47 °C preserved the fluorescent signal and retained substantially shorter clearing times (Figure 6b), when compared with 37 °C, which was proposed in original PACT. As images captured from tissues processed at 47 °C were characterized by the highest normalized contrast (Figure 6c), it was considered to be the optimal temperature for such passive clearing. A slightly higher temperature was proposed by Sindhwani et al.,[95] who achieved the same normalized optical density at 647 nm within 10 days of passive CLARITY at 50 °C versus 28 days at 37 °C (**Figure 7**). As the initial CLARITY technique relied on electrophoresis instead of passive immersion in OCAs, Epp et al.[71] examined temperature and duration of electrophoresis to minimize the originally observed electrophoresis-induced tissue damage. They observed that although 5 days of brain electrophoresis performed at 55 °C leads to almost complete transparency (**Figure 8**a), it also disrupts its structural integrity. Further optimization using ArcTRAP-tdTomato mice brain samples revealed, that 4 days

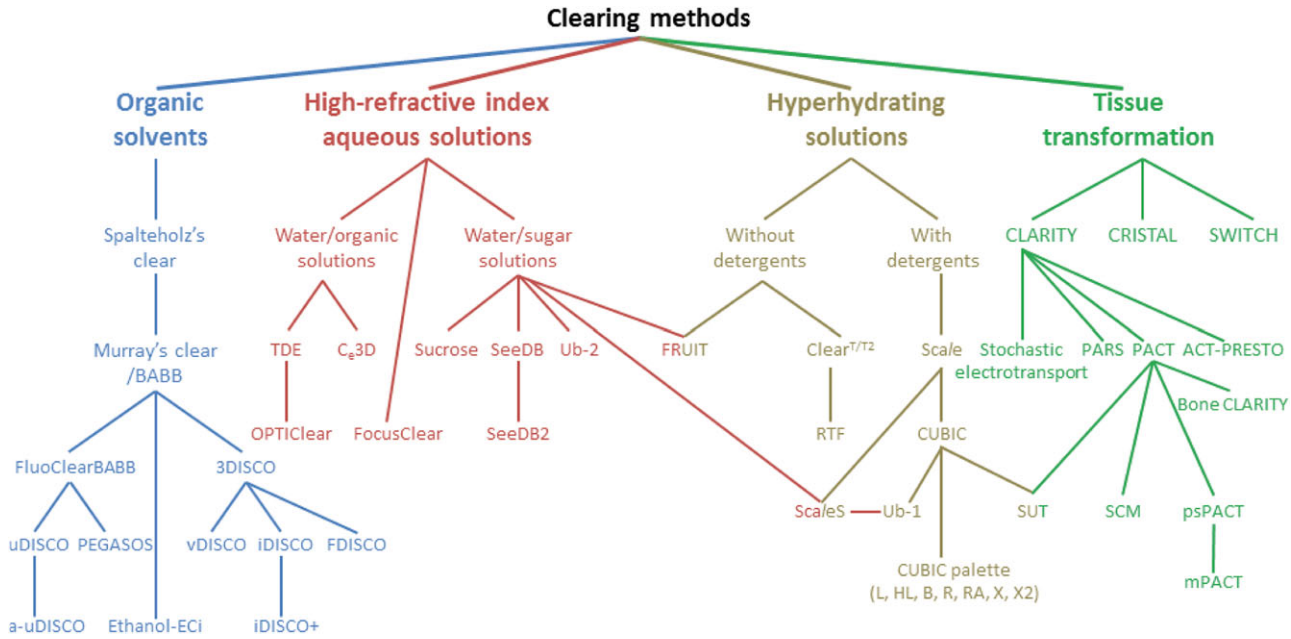

Figure 5. Up-to-date representation of clearing protocols. Within 2 years of the first proposed clearing protocol taxonomy,[9] the number of these had more than doubled, but they can still be classified into four main categories. See the text for description of each method.

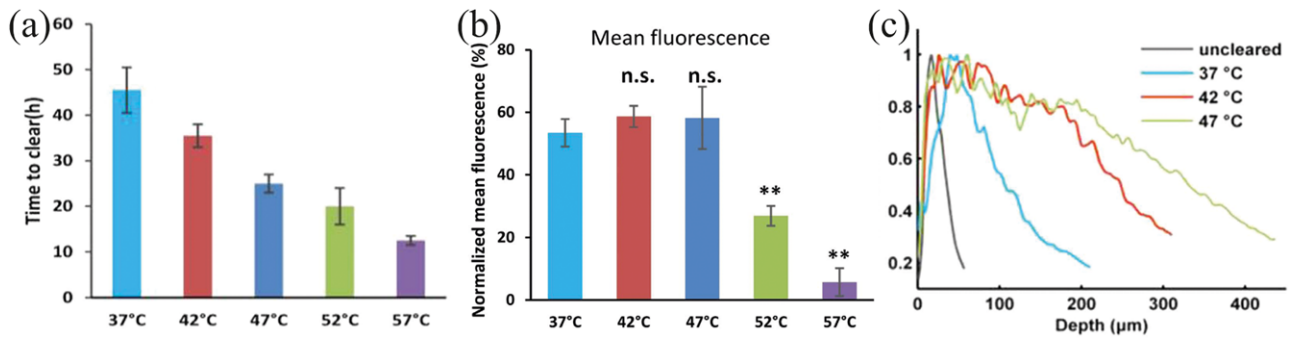

Figure 6. Optimization of PACT brain clearing temperature. a) Increase of temperature during the incubation step is inversely proportional to the clearing time, but b) starting from 52 °C, a significant loss of fluorescence stability is observed. c) Incubation at 47 °C provides the highest normalized contrast over 400 μm depth. Reproduced under the terms of the CC-BY Creative Commons Attribution 4.0 International License (http://creativecommons.org/licenses/by/4.0/).[94] Copyright 2017, The Authors. Published by Springer Nature.

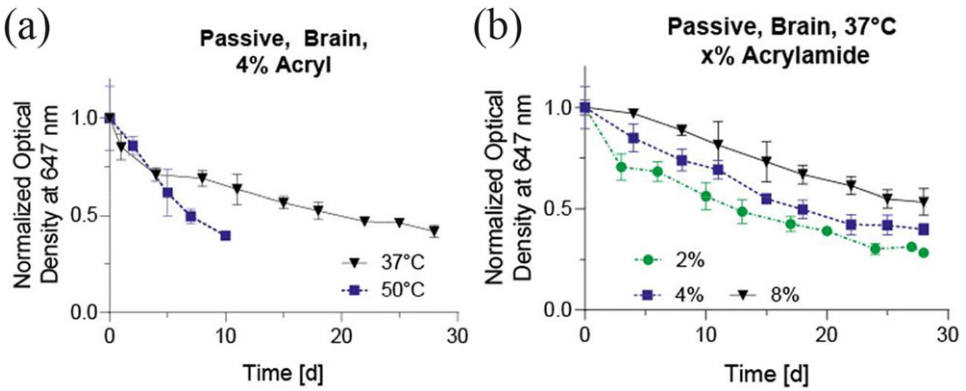

Figure 7. a,b) Optimization of passive CLARITY clearing conditions in the brain reveals that: a) the same optical density is achievable after 28 days of clearing at 37 °C and 10 days at 50 °C, while b) the lower the acrylamide concentration, the better the sample transparency after a given amount of time. Adapted with permission.[95] Copyright 2017, American Chemical Society.

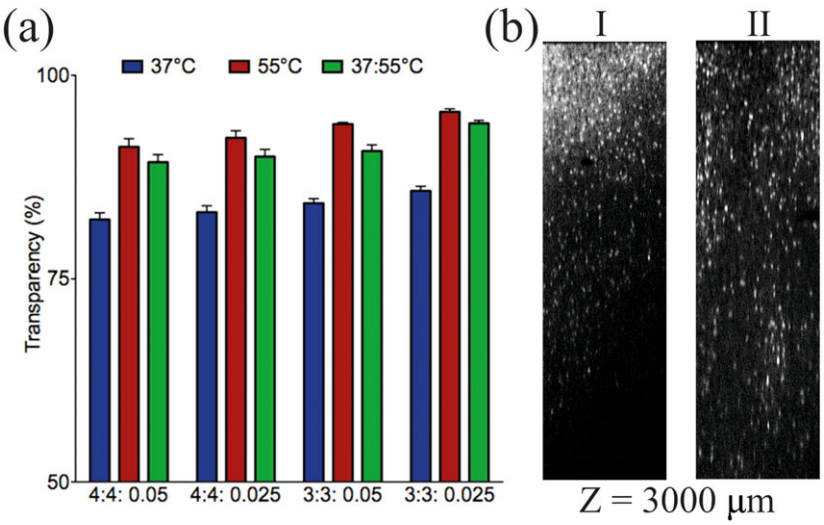

Figure 8. a) Optimization of temperature and hydrogel composition for electrophoretic variant of CLARITY (values under the bar represent concentration of fixative, acrylamide, and bis-acrylamide, i.e., 4:4:0.05—4% PFA, 4% acrylamide, and 0.05% bis-acrylamide). b) 5 days of brain clearing at 37 °C (I) leads to a substantially worse imaging depth of ArcTRAP-tdTomato mouse brain when compared to 4 days at 37 °C followed by 1 day at 50 °C (II). Reproduced under the terms of the CC-BY Creative Commons Attribution 4.0 International License (http://creativecommons.org/licenses/by/4.0/).[71] Copyright 2015, Society for Neuroscience.

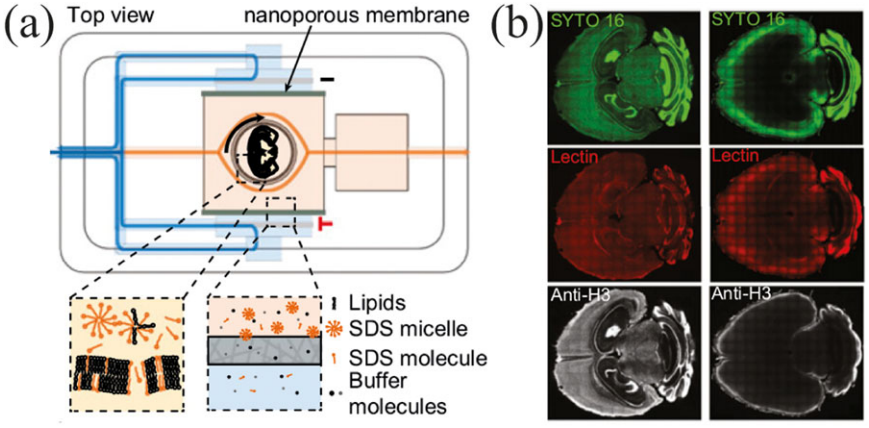

Figure 9. a) Scheme of a device for stochastic electrotransport, which b) ensures homogenous and greatly accelerated brain staining (left column) when compared with a passive protocol. Reproduced with permission.[70] Copyright 2015, National Academy of Sciences.

of electrophoresis at 37 °C followed by 1 day at 55 °C greatly improves imaging depth of endogenous fluorescence, as compared with 5 days at 37 °C (Figure 8b), while retaining tissue structure. This might be explained by the negative correlation between temperature and the volume of SDS micelle. To further overcome limitations of static electrophoresis, Kim et al.[70] developed computational model and proved the efficacy of stochastic electrotransport for CLARITY-processed specimens, in which sample is being continuously rotated in a chamber placed between two parallel electrodes (**Figure 9**a). Stochastic electrotransport accelerates both clearing and staining (which requires only 1 day for uniform and complete distribution of, for example, nuclear stain SYTO 16) and prevents tissue damage (Figure 9b).

Interestingly, although solvent-based clearing protocols are certainly the fastest to complete (e.g., 1–2 days are sufficient to clear adult mouse brain), they still can benefit from application of higher than room temperature (RT). As presented by Schwarz et al.,[46] although FluoClearBABB might be equally effective at both RT and 30 °C for ≈7 weeks old mice, only the clearing at 30 °C is effective for older animals (250 and 673 postnatal days, **Figure 10**a). However, the temperature range is very narrow, as increasing it to 37 °C exerts substantially negative effect on fluorophore stability (Figure 10b). As already described in the overview of original TOC techniques, based on the FDISCO findings it should be assumed that optimal preservation of fluorophores requires both dehydration and clearing with organic solvents not only below 37 °C (as suggested by Schwarz et al.[46]), but even at 4 °C.[54]

The influence of temperature on high-refractive index of aqueous and hyperhydrating solutions is not well documented. However, clearing is usually done at 37 °C, which might accelerate distribution of OCAs by reducing their dynamic

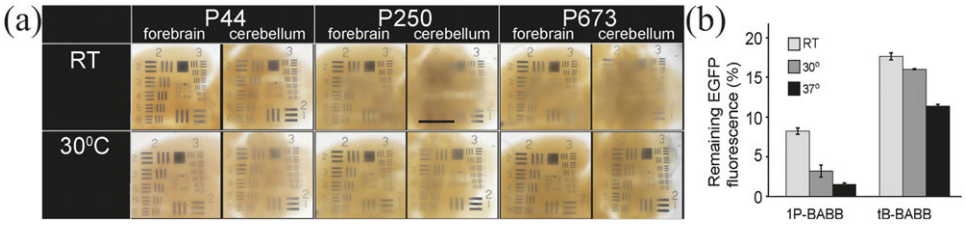

Figure 10. a) Increased temperature improves FluoClearBABB efficacy, especially in older (P250, P673) animals, but b) results in worse fluorescence stability. Reproduced under the terms of the CC-BY Creative Commons Attribution 4.0 International License (http://creativecommons.org/licenses/by/4.0/).[46] Copyright 2015, The Authors. Published by PLOS.

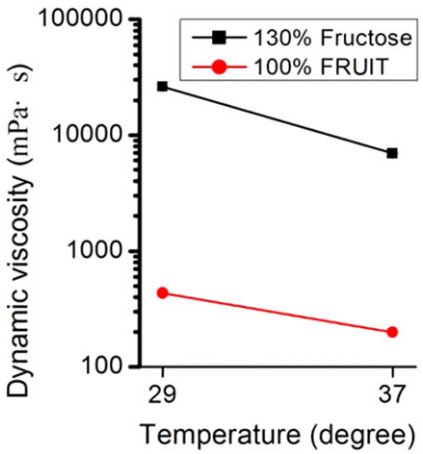

Figure 11. Dynamic viscosity is inversely proportional to temperature of hyperhydrating solution—FRUIT, which facilitates its molecular diffusion, improves clearing efficacy. Reproduced under the terms of the CC-BY Creative Commons Attribution 4.0 International License (http://creativecommons.org/licenses/by/4.0/).[86] Copyright 2015, The Authors. Published by Frontiers Media.

viscosity (**Figure 11**), but reduce the stability of genetically encoded fluorescent proteins on the other hand.[62]

2.2.2. Tissue Swelling and Expansion

Expanding tissue volume with water-containing clearing solutions (such as Sca*l*e or CUBIC reagent 1) enhances propagation of light by three main mechanisms: "dilution" of light scattering and absorbing molecules, partial solvation of extracellular matrix proteins, and finally global lowering, thus homogenization, of RI. Moreover, physical expansion results in increased image resolution. Although expansion observed in Sca*l*e and CUBIC was initially perceived as a drawback that might deform sample architecture and was reversed by Sca*l*eS and CUBIC reagent 2, respectively, a recent study by Murakami et al.[62] presented 3D single-cell-resolution whole-brain atlas based on controlled tissue expansion. This group performed screening of 1691 potentially water-soluble chemicals. 10% (w/w) solution of every chemical was applied on 9% gelatin gel and absorbance at 975 nm was measured (as water absorption of near infrared shows a peak around 975 nm, **Figure 12**a). Finally, 20% imidazole was selected as the expanding reagent (CUBIC-X1); however, the low RI of this solution (RI = 1.368) prohibited obtaining full optical transparency of murine brain. Thus, additional cocktail with high RI (CUBIC-X2, RI = 1.467) was prepared, consisting of 5% imidazole and 55% of antipyrine, characterized by high molar refractivity. Notably, CUBIC-X2 maintains CUBIC-X1-mediated 10× volume brain expansion and is highly transmissive to light in its visible spectrum (Figure 12b). When accompanied by customized LSFM in which electrically tunable lenses and galvanometer were introduced for the adjustment of the light sheet focus position along the *X*- and *Z*-direction (Figure 12c), respectively, CUBIC-X protocol allowed to scan the entire expanded mouse brain with subcellular resolution and revealed previously unknown areas, for example, in the granule cell layer of dentate gyrus.[62]

Even more intensive expansion microscopy was first proposed by Boyden lab.[96] In the set of experiments, the researchers presented several optimized protocols for nanoscale imaging of proteins,[97] RNA,[98] and clinical specimens.[99] Independently from application, expansion microscopy relies on the sequence of tissue labeling, gel anchoring (composed of, e.g., acrylamide, methylenebisacrylamide and acrylate, serving as a substructure for sample), protein digestion (e.g., with unspecific proteinase K), which loosens tissue structure, and finally expanding of tissue by 4.5× in one dimension, simply by its immersion in water. Therefore, as the water accounts for >99% of the resultant sample, tissue remains transparent with its RI being matched to RI of water. Altogether, expansion microscopy allowed researchers to capture morphology of individual dendritic spines using conventional Andor spinning disk confocal system with a 40×, 1.15 NA water immersion objective. In addition, such expanded samples were also compatible with traditional super-resolution microscopy—PALM. The same group has recently presented iterative expansion microscopy, in which the first hydrogel mesh is being replaced and tissue becomes again expanded by the second hydrogel mesh.[100] This led to spectacular total linear sample expansion by ≈16–22×, resulting in ≈25 nm effective resolution achieved with ≈300 nm diffraction-limited objective lens (**Figure 13**a).

As the expansion microscopy relies on proteinase K-mediated digestion, alternative approach called MAP (magnified analysis of proteome) was developed to omit this step, thus allowing for multiple rounds of immunochemical staining.[78] In order to efficiently expand the tissue by water-mediated swelling of hydrogel mesh, high concentration of acrylamide monomers is used in MAP to prevent crosslinking of proteins (Figure 13b). This approach allowed completion of seven rounds of antibody staining and super-resolution imaging with ≈60 nm lateral resolution, using diffraction-limited microscopes (e.g., 63×, 1.30 NA glycerol-immersion objective with the Leica TCS SP8 system, Figure 13c–e).

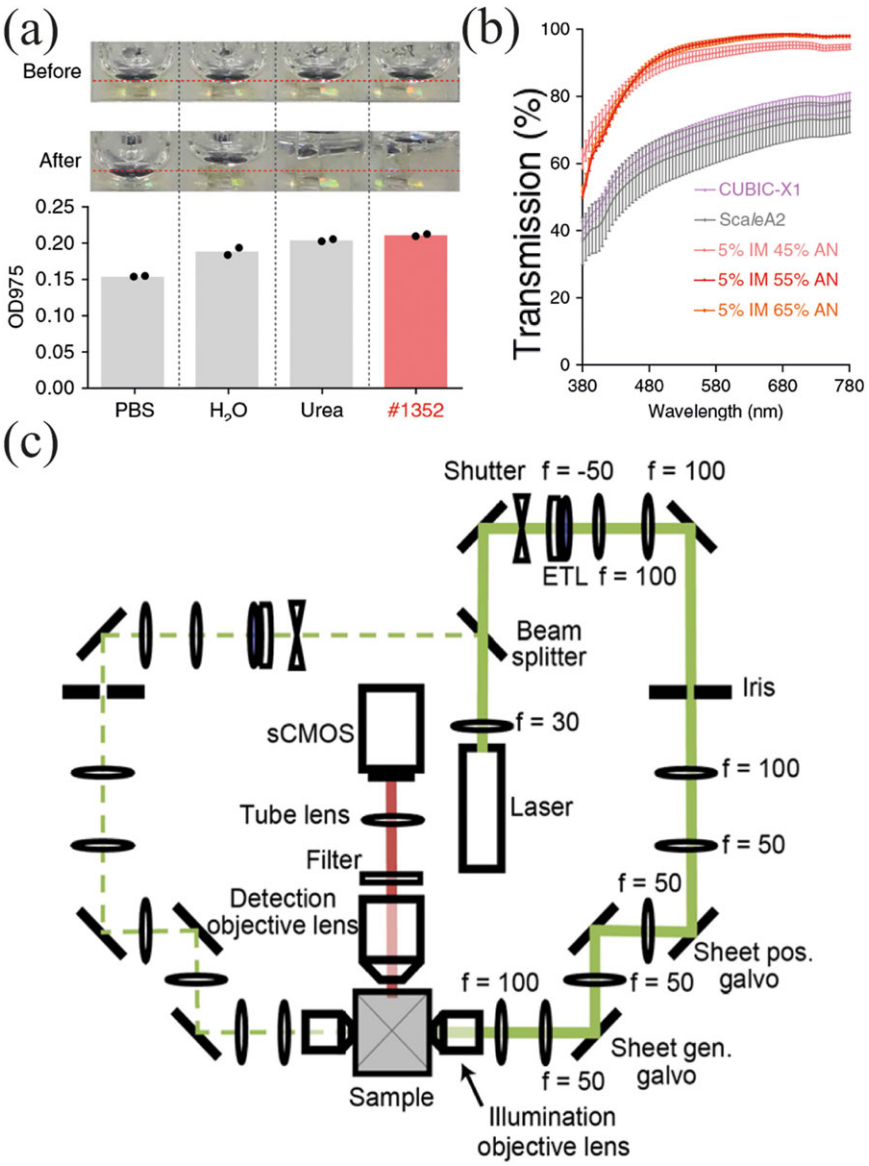

Figure 12. a) Initial chemical screening of chemicals with potential tissue-expanding properties was done based on the optical density of gelatin at 975 nm. b) CUBIC-X solutions are highly transmissive to light in the visible spectrum. c) Customized LSFM with electrically tunable lenses and galvanometer scanners for repetitive autofocus across a large, expanded brain. Reproduced with permission.[62] Copyright 2018, Springer Nature.

2.2.3. Tissue Shrinkage

Although counterintuitive, tissue shrinkage, which per definition decreases image resolution, also proved beneficial for some TOC applications. Tissue shrinkage is an inherent feature of organic solvent-based clearing, in which tissue undergoes dehydration in increasing gradients of alcohol. High imaging performance is mainly due to three factors: effective lipid solvation, matching of high (>1.50) RI of the remaining proteins and alignment of scatterers. Thus, while 65% brain volume reduction obtained with uDISCO approach greatly accelerated the imaging process, it did not prevent Ertürk's team from visualizing dendritic spines throughout the entire mouse brain (**Figure 14**). Interestingly, the transparency of uDISCO-cleared samples allows to perform successful light sheet imaging even with commercially available objectives not corrected to RI of BABB-D (uDISCO imaging solution, RI = 1.56), but to RI of water (RI = 1.33) and CLARITY (RI = 1.45, Figure 14a–d). The extreme shrinkage of hydrogel-processed tissue slices was recently presented by Kim et al.[101] in the approach called BrainFilm (**Figure 15**a). The authors found that 1–3 mm thick tissue slices, when placed between home-made assemble kit (made of cellophane papers and cover glass among others, Figure 15b) and dried at 55 °C in an oven, can be compressed to up to 90% in *Z*-axis. To prevent lateral distortion, tissues were surrounded by hydrogel layer during the compression step which, in case of 1-, 2- and 3-mm brain slices, resulted in only 6.80%, 6.45%, and 8.44% average distortion, respectively (Figure 15e). The main advantage of BrainFilm is

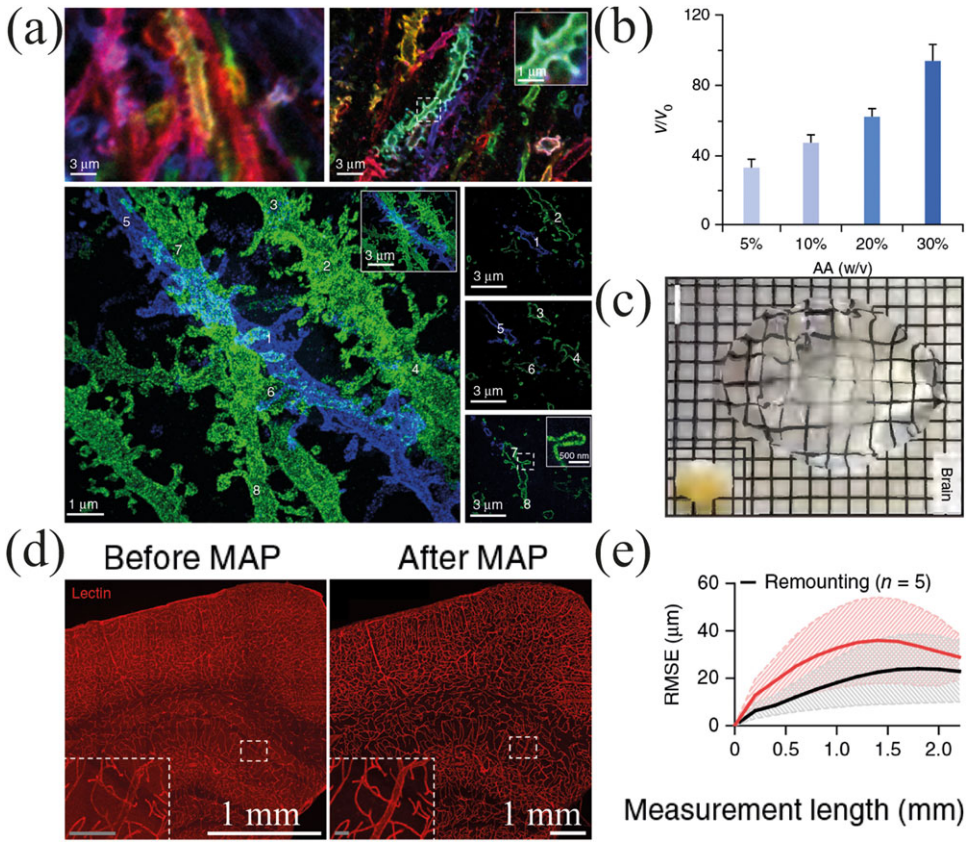

Figure 13. a) Confocal images of a mouse hippocampus before expansion (top left), after the first round of expansion (4.5×, top right) and after the second round of iterative expansion (20×, middle). Reproduced with permission.[100] Copyright 2017, Springer Nature. b) The higher the concentration of acrylamide used in a MAP protocol, the greater tissue expansion (tested on 1-mm-thick coronal slices, *V*, volume after expansion; V_0, volume before expansion). c) White-field image of MAP-processed mouse brain. d) Lectin staining before and after MAP and e) corresponding distortion analysis presented as a root-mean-squared measurement error (≈4 %). Scale bar in (c): 10 mm. Reproduced with permission.[78] Copyright 2016, Springer Nature.

great reduction of imaging and image post-processing times, as exemplary summation of three images from compressed tissue possesses equivalent information to 20 non-compressed images (Figure 15c,d). Moreover, BrainFilm workflow does not reduce signal-to-background ratio (4.93 ± 0.32 vs 5.09 ± 0.40, p = n.s.).

2.2.4. Power of Hydrogen

Several studies have already investigated the influence of power of hydrogen (pH) on TOC efficacy, with the major concern being preservation of endogenously encoded fluorescent proteins. Although it is feasible to visualize cells with quenched XFPs by performing immunostaining, it indisputably prolongs the procedure, raises its cost and does not guarantee complete epitope recognition. Loss of endogenous fluorescence was especially evident in case of solvent-based clearing methods, that were reported to quench the entire fluorescence within as little as 24 h.[44,45] This was first linked to the tissue deprivation of water molecules, the presence of which was suspected obligatory for the maintenance of XFPs emission.[8] Nevertheless, data obtained by several research groups clearly demonstrated that alkalization of dehydrating solutions (to pH of 9.0–9.5) prevents rapid loss of XFPs stability regardless of chemical used (*tert*-butanol in case of FluoClearBABB[46] and PEGASOS,[55] *tert*-butanol and BABB-D in a-uDISCO,[53] THF in FDISCO,[54] ethanol in ECi,[57] and 1-propanol in 2nd generation of ECi[102]). Based on these, it seems apparent that it is acidic pH of dehydrating solution, not loss of water molecules, that should be attributed for rapid quenching of XFPs. Indeed, this stays in line with the results obtained with extensively studied family of GFP-like proteins[103] showing serious decline in fluorescence intensity in slightly acidic (pH = 6.5) environment, even after few minutes of incubation.[104] Modest alkalization of clearing solutions is also essential for successful performance of CLARITY-related protocols. It is claimed that besides stabilization of XFPs, basic buffers slightly enhance delipidation efficiency by preventing proton buildup at the negatively charged surface of SDS micelles and shows minor tendency to reduce the amount of proteins lost during the clearing in most of the tested acrylamide/bisacrylamide hydrogel compositions (when, e.g., 8% SDS-PBS pH 7.5 and 8% SDS-PBS pH 8.5 were compared).[68] Hyperhydrating and high-refractive index solutions are in general known to preserve XFPs. Noteworthy, the authors of original CUBIC reagents asserted good fluorescence stability of the cleared organs besides

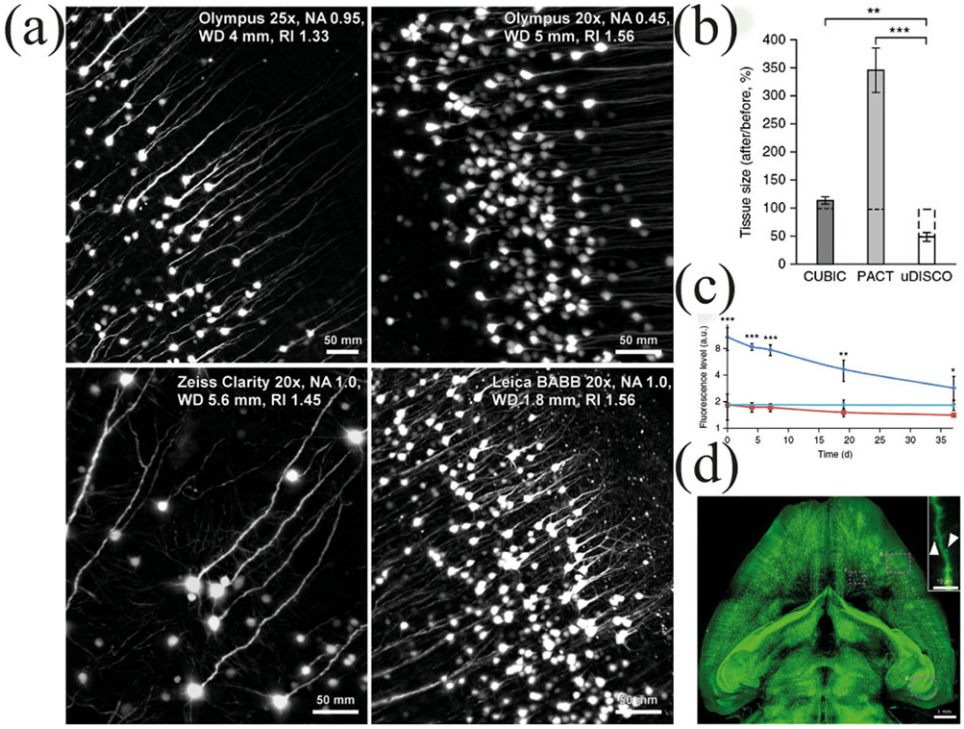

Figure 14. a) Comparison of uDISCO brain imaging efficacy with objectives uncorrected (left panels) and corrected (right panels) to RI of imaging solution. b) Although uDISCO clearing extensively shrinks tissues, it also c) leads to better fluorescence stability (light blue: uDISCO, blue; Sca*l*eS, red: 3DISCO) and d) does not prohibit high-resolution imaging of the entire brain. Scale bar in (a): 50 μm, in (d): 1 mm. Reproduced with permission.[36] Copyright 2016, Springer Nature.

utilization of high amounts of denaturating urea. Again, this seems logical as CUBIC consists of basic aminoalcohols[58] and even 8 M urea at 50 °C was shown to cause negligible GFP denaturation, as long as the pH was alkaline (>7.5).[104] Another way to preserve endogenous fluorescence upon TOC is generation of more stable forms of XFPs. Recently, such ultrastable, monomeric form of GFP was developed by Scott et al.[105] and combined with passive, 5-week long CLARITY, showing much improved fluorescence emission when compared to EGFP.

Interestingly, pH can not only affect the stability of XFPs but also tissue architecture. In a recent study, Tainaka et al.[61] presented that while neutral CUBIC-R (new RI-matching solution consisting of antipyrine and nicotinamide) causes almost no macroscopic deformation to mouse brain, its weakly basic form (pH 8.0–9.0) promotes swelling. All of the aforementioned information inclines TOC to be conducted under controlled and reported pH to ensure acquisition of repetitive results.

2.3. Optical Approaches to TOC

Although optically cleared samples are compatible with a number of microcopy and imaging techniques, such as confocal, two-photon, optical coherence microscopy, scanning laser optical tomography or MRI, just to name a few, it is LSFM which was the most widely used so far. The unique feature of LSFM is that instead of single spot illumination, it generates micrometer-thick sheet of light, which selectively excites the entire focal plane of the specimen. Therefore, it both reduces phototoxicity (i.e., allows for repetitive imaging of less stable fluorophores) and time required for imaging (by ≈2 orders of magnitude as compared to confocal). Recently, excellent tutorial covering LSFM configuration and engineering was presented by Olarte et al.[6]; however, we continue to review recent advances in LSFM developed specifically for cleared organs.

2.3.1. LSFM for Imaging of Thick, Optically Cleared Tissues

Since the first TOC methods were developed, their utility was continuously demonstrated by imaging with light sheet fluorescence microscopy.[22,26,45,106] The first of such studies was performed by Dodt et al.,[22] who coupled BABB-cleared tissues (brain, embryos and *Drosophila melanogaster*) with two sided illumination, thus reaching high imaging speed (0.5–2.0 s per 1 optical slice depending on tissue size) in millimeter-thick samples. However, lack of available objectives corrected for RI of imaging media and solution like adaptive optics,[107] to reduce resulting spherical aberration, significantly influenced imaging resolution and allowed to discriminate dendritic spines only in the excised hippocampi (**Figure 16**a). To reduce aberration while extending Rayleigh range, the same group presented improved laser light sheet generator composed of two units, to first reshape a Gaussian beam profile into elliptical beam and second, to generate light sheet by passing it through two achromatic cylindrical lenses (Figure 16c).[108] Such system granted generation

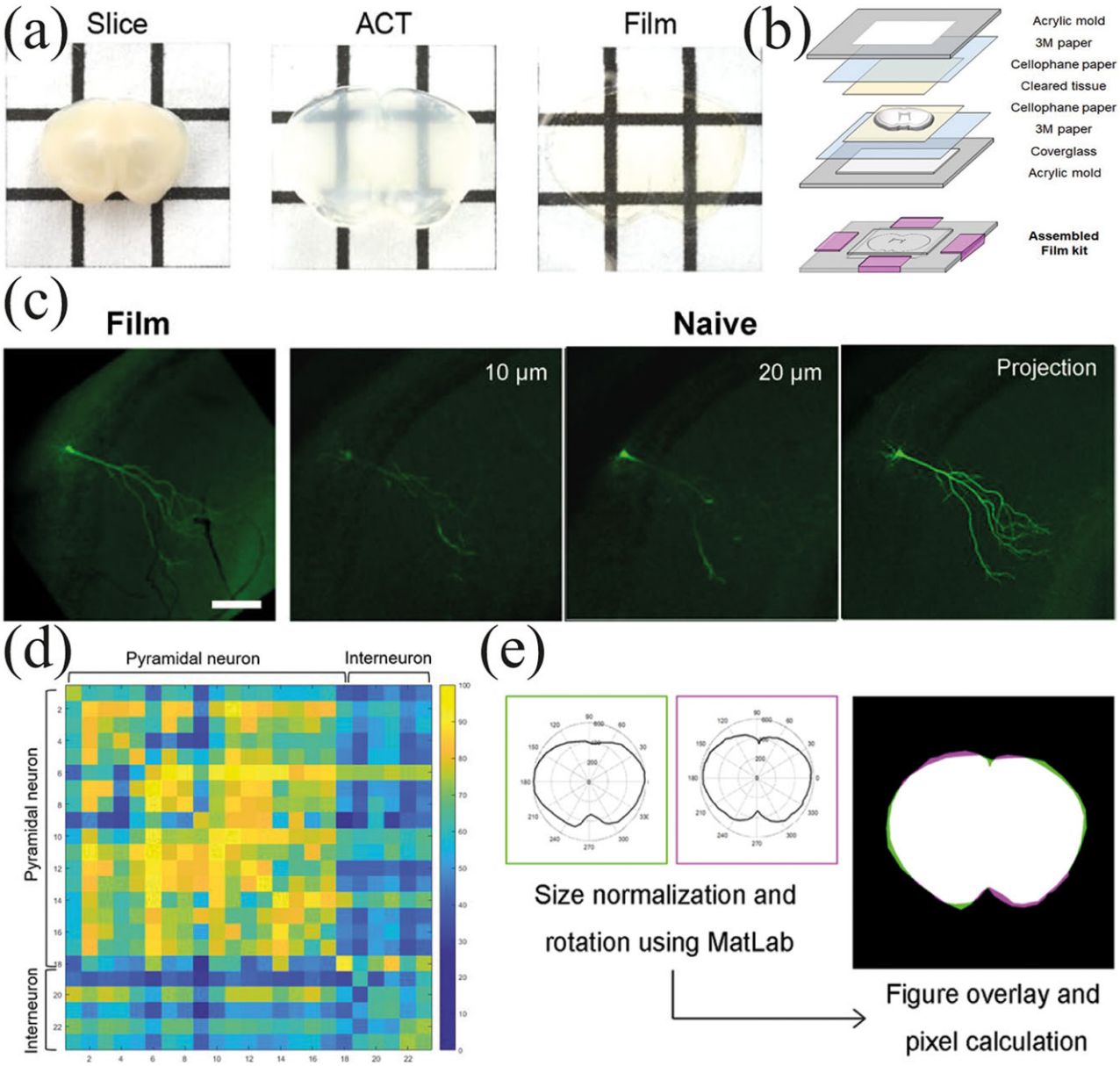

Figure 15. a) BrainFilm efficiently compresses tissue slices and requires b) a straightforward assembly kit. c) A single image of biocytin-labeled neuron provides similar information to the entire stack projection. d) Heatmap representing matching rates between 18 pyramidal and 5 interneurons between stack projection and BrainFilm processing. e) BrainFilm causes only minor distortion of tissue shape. Size of scale bar in (c) not available. Reproduced under the terms of the CC-BY Creative Commons Attribution 4.0 International License (http://creativecommons.org/licenses/by/4.0/).[101] Copyright 2018, The Authors. Published by Springer Nature.

of thin and stable light sheet over >10 mm (Figure 16d) and much improved optical sectioning performance due to the presence of aspherical optical elements reducing aberration (Figure 16b). Very recently, light sheet generation was again optimized by Dodt's group[109] to reduce the thickness of beam (thus enhance isotropy of imaging). Its performance was tested on fully cleared, GFP-harboring *D. melanogaster* (for the first time efficiently depigmented with new solution based on CUBIC and containing 2,2′,2″,2‴(ethylenedinitrilo)-tetraethanol) by multi-view imaging at orthogonal positions. The established protocol, called FlyClear, might serve as a robust platform for insect studies.

The alternative approach for aberration reduction in thick, cleared samples, adaptive optics, was experimentally introduced by Masson et al.[110] Taking advantage of the independent course of illumination and detection pathways in LSFM, the authors were able to apply wavefront sensor adaptive optics (WAO) to correct the latter (**Figure 17**a). Indeed, by using CUBIC and CLARITY for multi cellular tumor spheroids clearing, Masson with colleagues showed improvement of image contrast and peak intensities, when acquired with WAOLSFM (Figure 17c). Moreover, to better reflect improvement of image quality in specimen images characterized by low signal-to-noise ratio, they proposed

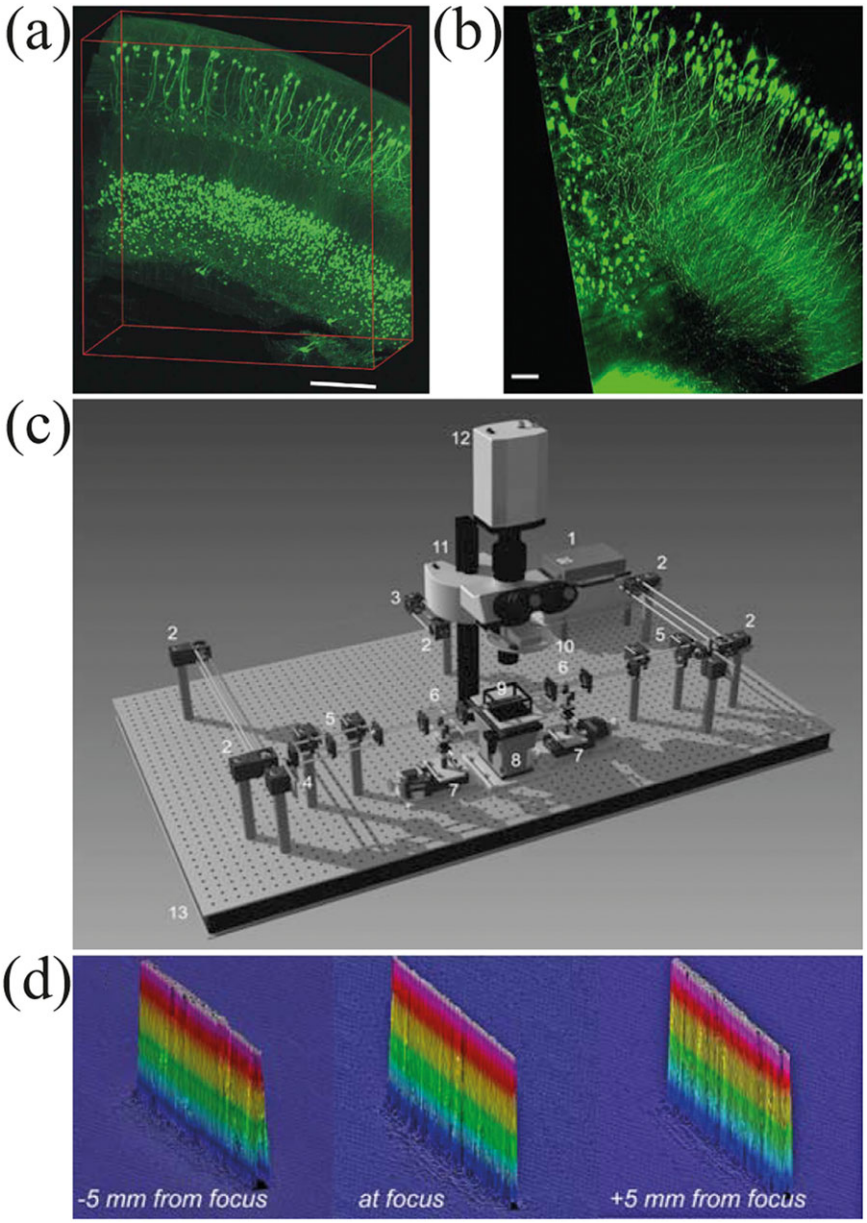

Figure 16. a,b) Comparison of image quality between classic ultramicroscopy (a) and ultramicroscopy with aspheric optics (b), and c) its scheme (1: 488 nm Sapphire Laser, 200 mW; 2: 45° mirrors; 3: 50% beam splitter; 4: laser shutter, laser 2000, Germany; 5: light sheet generator optics part A; 6: light sheet generator optics part B [a movable cylindrical lens]; 7: computer-controlled linear stage for adjustment in the z-direction, 8: computer-controlled elevation stage; 9: specimen container with quartz windows, 10: custom-made computer-controlled filter wheel; 11: customized Leica microscope; 12: scientific grade CCD-camera). d) The presented setup generates a large Rayleigh range. Scale bar in (a): 5 µm, in (b) scale bar size is not available. a) Reproduced with permission.[22] Copyright 2007, Springer Nature. b–d) Reproduced with permission.[108] Copyright 2013, Wiley-VCH.

new metric based on spatial frequencies, relative difference of frequency (RD), defined by

$$\mathrm{RD}(f_r) = \frac{\widehat{U}_{\mathrm{on}}(f_r) - \widehat{U}_{\mathrm{off}}(f_r)}{\widehat{U}_{\mathrm{off}}(f_r)}$$

where $\widehat{U}_{\mathrm{off}}$ and $\widehat{U}_{\mathrm{on}}$ are the radial frequencies of images acquired before and after the (WAO) correction, respectively. Despite no enhancement in image quality, as inspected by the gradient intensity map, RD revealed significant improvement of such (Figure 17b). Other groups also aimed at optimization of LSFM optics for cleared organs and exploited "self-healing," propagation invariant beams, Bessel and Airy beams in particular, which theoretically should outperform Gaussian beam in setting of large field-of-view, turbid specimen imaging. When compared with Gaussian, Airy beam provided both superior image quality and imaging depth (30%, 80 µm) for TDE-cleared, mCherry-harboring kisspeptin neurons in 400 µm thick mouse

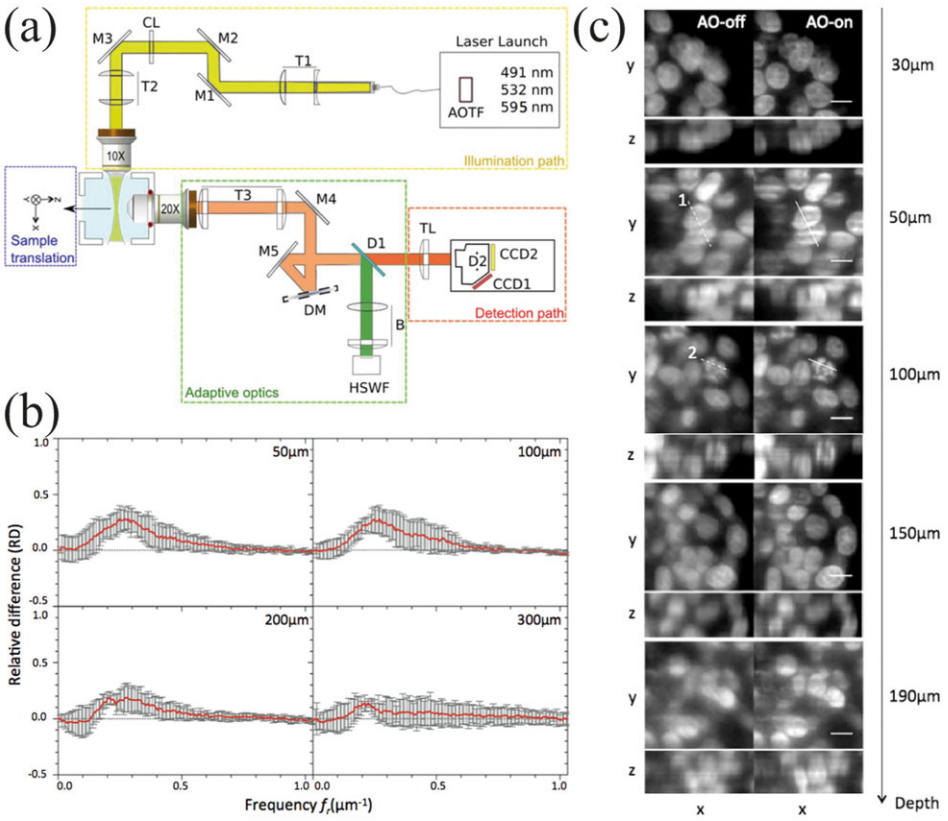

Figure 17. a) Scheme of the WAOSPIM setup. b,c) WAOSPIM-corrected LSFM imaging has enhanced quality as shown by relative difference curves for a particular frequency (positive values indicates effective correction, bars: SD) (b) and images of cleared multi-cellular tumor spheroids (c). AOTF, acousto-optic tunable filter; T1–T3, telescopes; M1–M5, mirrors; CL, cylindrical lens; DM, deformable mirror; D1 and D2, dichroic mirrors; HSWF, Hartmann–Shack wavefront sensor; B, lens system for DM-HSWF pupil conjugation; TL, tube lens; CCD1 and CCD2, coupled charged devices. a) Reproduced under the terms of the CC-BY Creative Commons Attribution 4.0 International License (http://creativecommons.org/licenses/by/4.0/).[107] Copyright 2012, The Authors. Published by PLOS. b,c) Reproduced under the terms of the CC-BY Creative Commons Attribution 4.0 International License (http://creativecommons.org/licenses/by/4.0/).[110] Copyright 2015, Springer Nature.

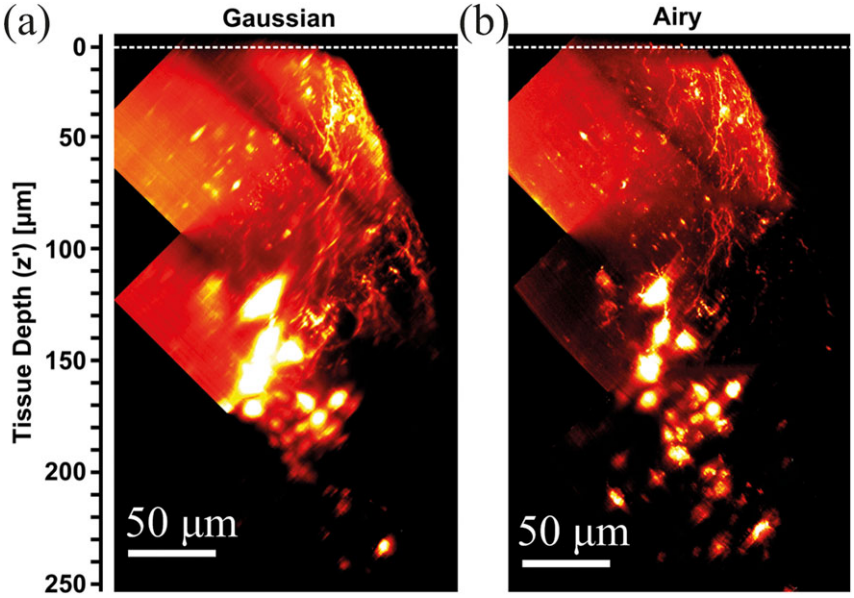

Figure 18. Comparison of Gaussian and Airy LSMs for imaging of fluorescent TDE-cleared brain tissue. a,b) Although Gaussian LSM (a) provides similar imaging depth to Airy LSM (b), the latter provides better image resolution. Dashed white lines indicate the tissue surface. Scale bar: 50 µm. Reproduced under the terms of the CC-BY Creative Commons Attribution 4.0 International License (http://creativecommons.org/licenses/by/4.0/).[111] Copyright 2016, The Optical Society.

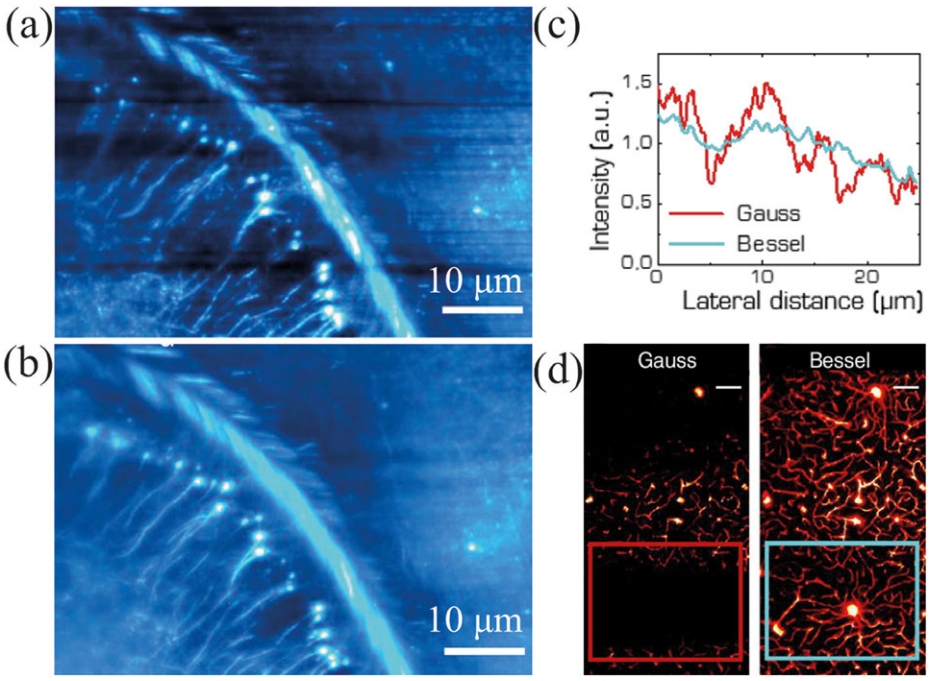

Figure 19. a,b) Comparison of maximum-intensity projection images over 20 μm distance in Thy1-GFP, TDE-cleared mouse brain with Gaussian (a) and Bessel (b) beams. c) Bessel beam provides uniform signal intensity and less stripping artifacts (reflected as drops in red curve). d) Gaussian beam causes undersampling of tetramethylrhodamine-albumin stained blood vessels in the cleared brain. Scale bar in (d): 10 μm. Reproduced under the terms of the CC-BY Creative Commons Attribution 4.0 International License (http://creativecommons.org/licenses/by/4.0/).[112] Copyright 2018, The Authors. Published by Society for Neuroscience.

brain slices (**Figure 18**).[111] The utility of Bessel and Gaussian beams for imaging and quantification of whole-brain vasculature and neuronal fluorescent signal were side-by-side evaluated by Müllenbroich et al.[112] Notably, both setups (Gaussian and Bessel) were characterized by similar lateral and axial full width at half maxima (1.56, 7.83 vs 1.77 and 8.47, respectively); however, utilization of Bessel beam was superior in all tested conditions, as it generated less striping artifacts (usually caused at the brain surface by bubbles or light absorption by bright structures), more homogenous image of deep brain structures, and a more complete picture of vasculature (**Figure 19**). In addition to optics,[113,114] recent studies examined distinct arrangements of illumination and detection pathways in LSFM setup.[115,116] Migliori et al.[115] presented light sheet theta microscopy (LSTM) characterized by a symmetrical, oblique arrangement of two light sheets (**Figure 20**a) to overcome reduction in image quality usually observed toward the medial part of a specimen, when imaged with standard orthogonal single-plane illumination. This conceptual advance yields uniform, high-resolution images across the entire sample, thus reducing the limitations of lateral size of sample, which is especially valuable, when imaging of large tissues is desired. Indeed, LSTM imaging with 4×/0.28 NA/29.5 mm WD (Olympus) illumination and 10×/0.6 NA/8 mm WD (Olympus) detection objectives, by maximizing the angular separation, θ, available in presented setup (≈60°), exhibited high image quality and axial resolution (≈4–6 μm) across the entire field-of-view (Figure 20b). Glaser et al.[116] developed prototype of open-top LSFM for versatile mounting with possible application for rapid intraoperative guidance in surgical oncology or post-operative 3D volumetric pathological analysis of biopsy specimens. Distinctly from LSTM, open-top LSFM relies on oblique arrangement not only of light sheet, but also detection objective (**Figure 21**). To reduce aberration of beams traveling from air into glass and vice versa, hemispherical solid-immersion lens covered with thin oil layer, matching RI between lens and glass-plate sample holder ($RI = 1.464 \pm 0.001$), was included. The advantages of open-top LSFM include high imaging speed (imaging of 4 cm^2 excised breast tissue surface took <1 min) in comparison with routine intra-operative examination of frozen section and great scanning area, restricted only by a travel range of microscope stage (11 × 7.5 cm in presented setup). The same group has recently proposed further optimization of the open-top system in which illumination and collection objectives are below chamber that is filled with RI-matching solution, on top of which are holder and specimen.[117] Interestingly, the authors searched for holder materials that could match the RI of both specimen and its respective RI-matching solution. The exploited concept of RI matching between clearing solution, holder and tissue allowed them to image samples cleared with distinct protocols that span the entire RI range of already published methods (1.33–1.56) with up to 0.5 cm imaging depth. Yet another novel idea for improving the quality of LSFM-obtained images, by solving the problem of typical artifacts (such as already mentioned striping artifacts), was presented by Mayer et al.[118] By using already known hybrid system of two distinct imaging modalities: LSFM with optical projection tomography (called OPTiSPIM), the authors successfully combined LSFM-derived high-resolution fluorescence data with 3D maps of the attenuation to "refill" shadows/striping artifacts (**Figure 22**).

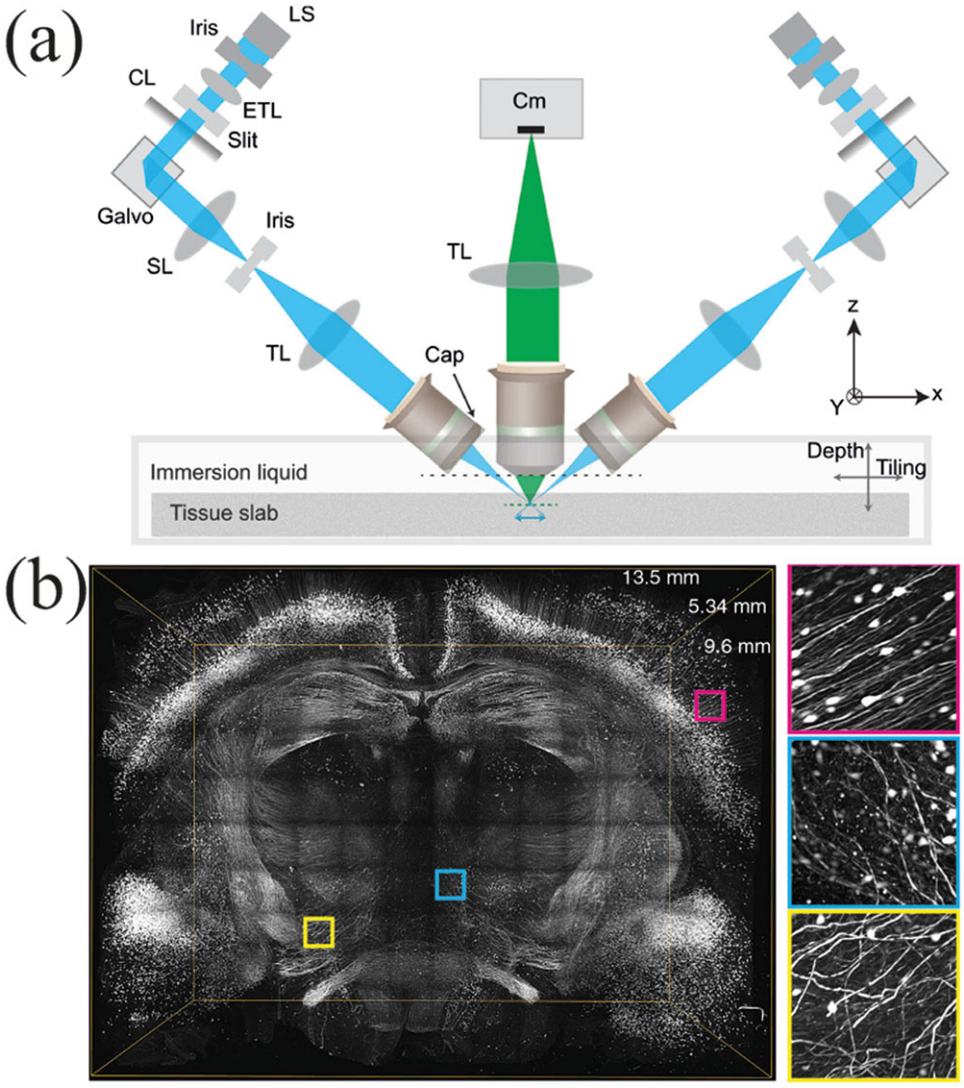

Figure 20. a) Scheme of light sheet theta microscopy, in which two symmetrical light sheets are placed obliquely. b) Oblique arrangement allows imaging with homogenous resolution across the entirety of large samples such as an expanded coronal brain slice. Reproduced under the terms of the CC-BY Creative Commons Attribution 4.0 International License (http://creativecommons.org/licenses/by/4.0/).[115] Copyright 2018, The Authors. Published by BioMed Central.

2.3.2. Non-LSFM-Based Imaging

Notably, it is also beneficial to couple TOC with other than confocal/LSFM imaging techniques, such as optical computed tomography (optical-CT),[119] optical emission computed tomography (optical-ECT) and scanning laser optical tomography (SLOT).[120] These modalities might be perceived as an equivalent of CT which uses visible light, instead of X-ray, during the imaging, with SLOT characterized by less "stray" light, that is, the light that does not follow primary ray path through the optical system.[121] As these techniques reconstruct optical projection images of transmitted light into 3D images of the distribution of optical attenuation, optical-CT was coupled with TOC as early as in 2002 by Sharpe et al.[122] to reduce light scattering and its refraction. Thus, optical-CT was successfully applied to evaluate blood vessels of cleared and stained with light-absorbing inks tissues, such as tumor, heart, or lung.[123] Prominently, optical-ECT and SLOT detects fluorescent labeling, which means that when applied to well cleared samples these might give both CT-like and LSFM-like images almost simultaneously.[120,124]

Coupling TOC with MRI has already allowed to determine the contribution of both lipids and proteins to brain MRI contrast[125] and deepen the understanding of various MRI modalities, such as diffusion tensor imaging.[126] Moreover, recent application of both optical coherence tomography and MRI to brain TOC by Baek et al.[127] provided a new way for quantitative assessment for the measurement of the clearing efficacy for protein-rich and lipid-rich brain regions. Such evaluations along with spectroscopic studies[128] might help elucidate the most optimal clearing conditions/formulas for particular organs of interest.[127] Optical coherence microscopy coupled with CLARITY-processed brain facilitated detection of Congo red–stained amyloid-beta plaques in an animal model of Alzheimer's disease.[129,130] Interestingly, only one day of optical clearing doubled the penetration depth

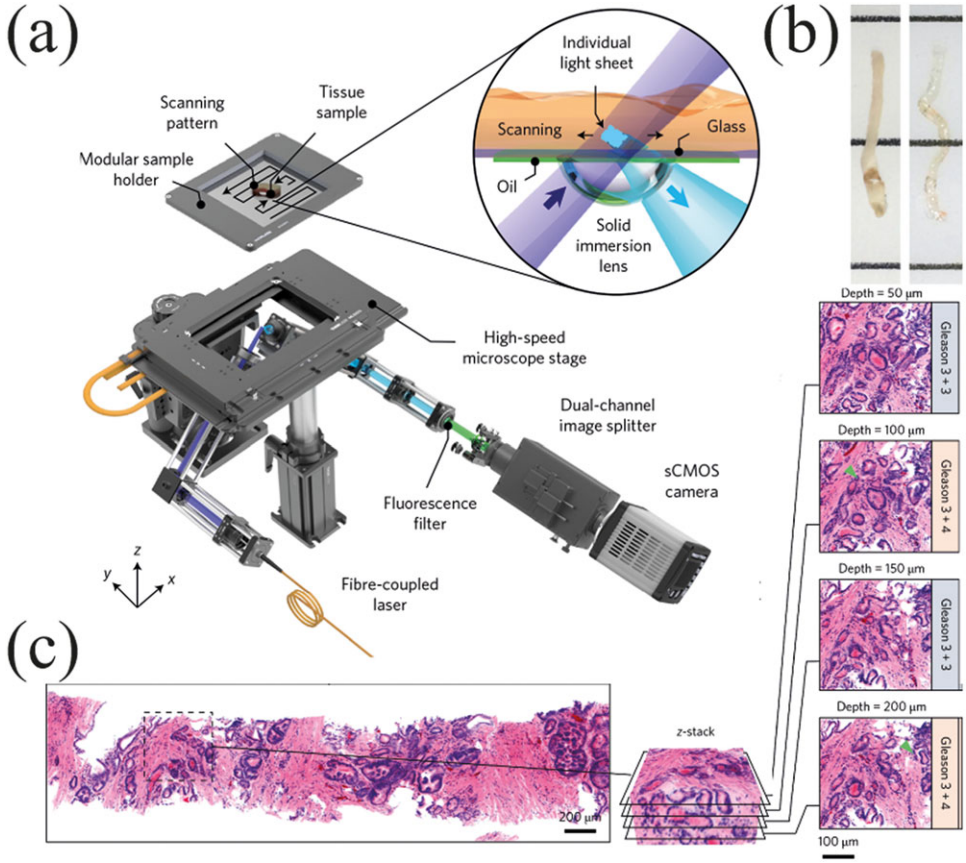

Figure 21. a) Scheme of open-top LSFM that allows for b) rapid imaging of, for example, a cleared prostate biopsy specimen. c) Prostate biopsy was DRAQ5 and eosin stained and image pseudo-colored to resemble an H&E stain. Notably, Gleason score 3 + 4 (as assessed by pathologists) was due to tangential sectioning artifacts, while 3D rendering confirmed it to be 3 + 3. Reproduced with permission.[116] Copyright 2017, Springer Nature.

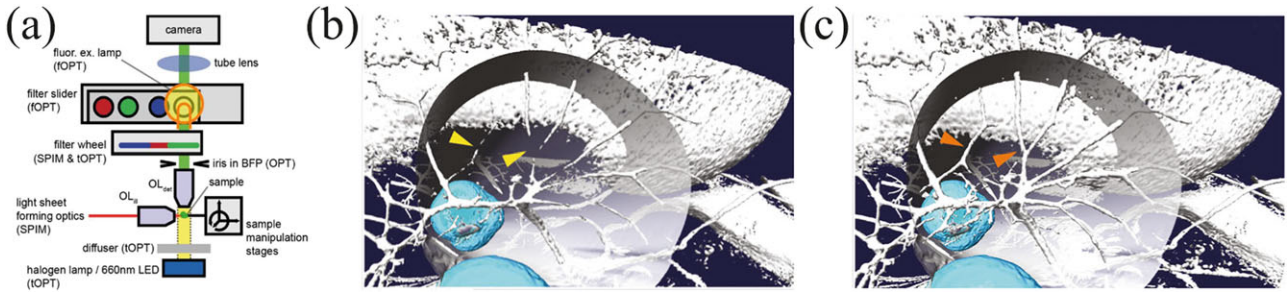

Figure 22. a) Scheme of OPT and SPIM (LSFM) hybrid: OPTiSPIM. b,c) E12.5 embryonic mouse head before (b) and after (c) attenuation correction. Reproduced under the terms of the CC-BY Creative Commons Attribution 4.0 International License (http://creativecommons.org/licenses/by/4.0/).[118] Copyright 2018, The Authors. Published by Springer Nature.

(100 µm vs 200 µm, **Figure 23**). However, as optical coherence microscopy relies on backscattered and backreflected light intensity, further clearing decreased the tissue contrast so that it was no more compatible with imaging. Using SWITCH-cleared brains and optical frequency domain imaging, in which, similarly to optical coherence microscopy, image is obtained from intrinsic scattering of tissue, Ren et al.[131] developed clearing-assisted scattering tomography (CAST). Although not reaching cellular resolution, CAST allows for rapid interrogation of major brain areas and tracts; for example, visualization of the entire mouse hemisphere (depth of 6.2 mm) took 22 min to obtain 13 transverse scans with 350 µm interval (**Figure 24**).

Significantly more time-consuming, but capable of reconstructing the brain-wide morphology of neurons with submicrometer resolution, is a recent platform developed by Economo and Clack et al.[132] In this system, the authors combined brain TOC with two-photon laser scanning microscope integrated with a vibrating microtome and automated designation of tiles (**Figure 25**a). Application of TOC helped them to bypass limitation of classical serial two-photon tomography, in which

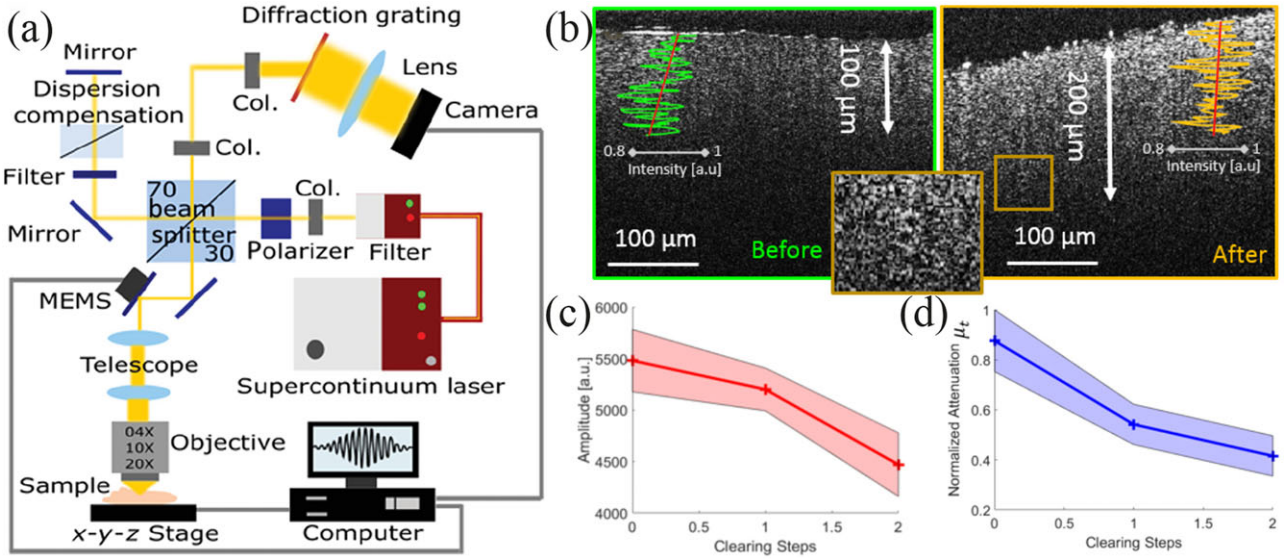

Figure 23. a) A visible-light OCM system. b–d) 2 days of SWITCH brain clearing doubles imaging depth (b) and decreases both mean OCM amplitude (c) and mean global attenuation (d) as normalized to noncleared tissue (shaded bands represent standard deviations). a) Reproduced under the terms of the CC-BY Creative Commons Attribution 3.0 Unported license (https://creativecommons.org/licenses/by/3.0/).[130] Copyright 2018, The Authors. Published by SPIE. b–d) Reproduced under the terms of the CC-BY Creative Commons Attribution 4.0 International License (http://creativecommons.org/licenses/by/4.0/).[129] Copyright 2016, The Optical Society.

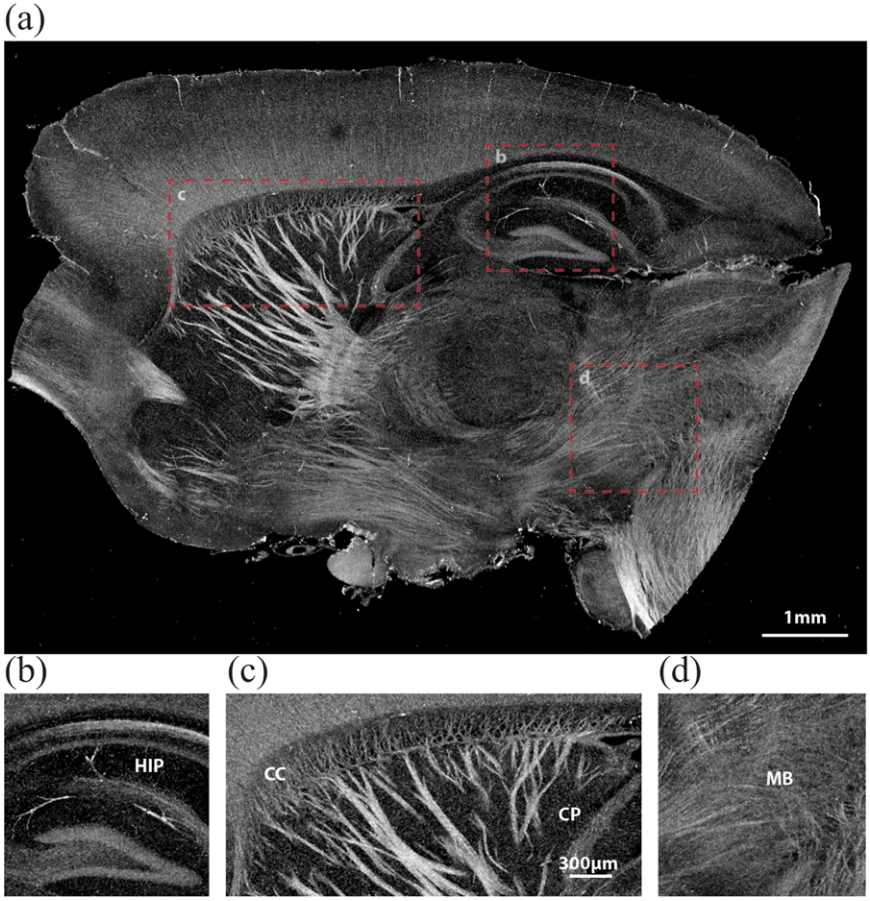

Figure 24. a) A sagittal view of clearing-assisted scattering tomography performed on a mouse brain hemisphere merged from 13 transverse scans acquired with a 350 µm interval. b) HIP, hippocampus, c) CC, corpus callosum; CP, caudoputamen, and d) MB, midbrain. Reproduced under the terms of the CC-BY Creative Commons Attribution 4.0 International License (http://creativecommons.org/licenses/by/4.0/).[131] Copyright 2017, The Authors. Published by Springer Nature.

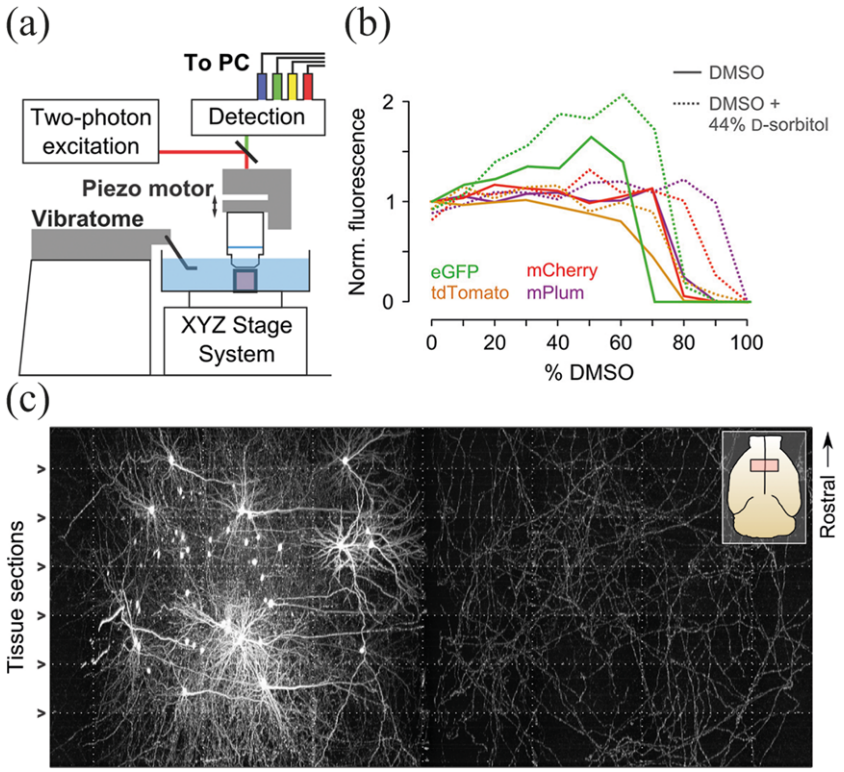

Figure 25. a) Apparatus for automated volumetric two-photon tomography combined with: b) a new TOC reagent based on DMSO and D-sorbitol that preserves fluorescence of purified fluorescent proteins and does not precipitate during long-term imaging, allowing for c) brain-wide reconstruction of neurons. A mouse brain was injected using an adeno-associated virus-based labeling strategy, in which 10–50 motor cortical neurons were being labeled. Dotted lines represent borders between adjacent tiles, left panel: right hemisphere, right panel: left, contralateral hemisphere. Reproduced under the terms of the CC0 1.0 Universal (CC0 1.0) Public Domain Dedication.[132] Copyright 2016, eLife Sciences Publications.

tissue volumes are being snapshot as 2D images separated by as much as ≈50 µm in the axial direction. In particular, TOC increased the maximum imaging depth of single tile for up to 250 µm (limited by the working distance of the objective) and allowed to perform optical sections every ≈1 µm with high signal-to-noise ratio. As the process is lengthy, taking 8–10 days for serial sectioning and imaging of one mouse brain, the authors had to search for TOC solution that 1) preserves fluorescent signal, 2) is resistant to evaporation and precipitation, 3) makes brain tissue compatible with vibratome slicing and does not compromise its fine details. As none of the existing TOC methods fulfilled all of the mentioned criteria (with organic solvents quenching the signal and being incompatible with vibratome slicing and aqueous- and high-refractive index methods prone to cause precipitations) they discovered mixture of DMSO and D-sorbitol to be suited for such long-term imaging and slicing (Figure 25b). Altogether, this approach allowed them to reconstruct voluminous arborizations of diverse neuronal projections within the motor cortex with great detail (Figure 25c).

Stimulated Raman scattering (SRS) microscopy that allows for label-free imaging and distinction of several biological key molecules such as water, collagen, proteins, DNA, sugars, lipids, cholesterol, and their forms (saturated vs unsaturated lipids or α-helices vs β-sheets of proteins) was also recently coupled with TOC to increase the imaging depth oscillating around only ≈100 µm for high-scattering tissues like brain or skin (which is only half of the spheroid length in case of, for example, spheroids from Ras-transformed MCF-10A breast epithelial cells).[133] Wei et al.[133] found that incubation in 8 M urea or tuned formula of 8 M urea with addition of 0.2% Triton X-100 causes remarkable, 10–15-fold increase in the depth limit of SRS (defined as the depth at which the signal-to-background ratio of SRS images reaches 0.5). Using this label-free approach the authors could reveal significant differences in lipid-to-protein ratios between healthy brain and glioblastoma tissues and interestingly, also between glioblastoma tumor cells itself. This approach was also compatible with deuterium oxide (D_2O) probing SRS (in which cell metabolism can be studied by investigation of incorporation of deuterium into newly synthesized macromolecules), which exposed heterogenic metabolic activity between infiltrating and dense tumor cells as well as a major increase in protein synthesis and a minor increase in lipid synthesis in tumor vasculature versus normal vasculature.

3. Application of TOC for Particular Peripheral Organs

3.1. Heart

Heart possesses a formidable challenge for its clearing, as it is made of densely packed cardiomyocytes arranged into three interconnecting layers (subepicardial, middle, and subendocardial). Each cardiomyocyte is surrounded by endomysium, a

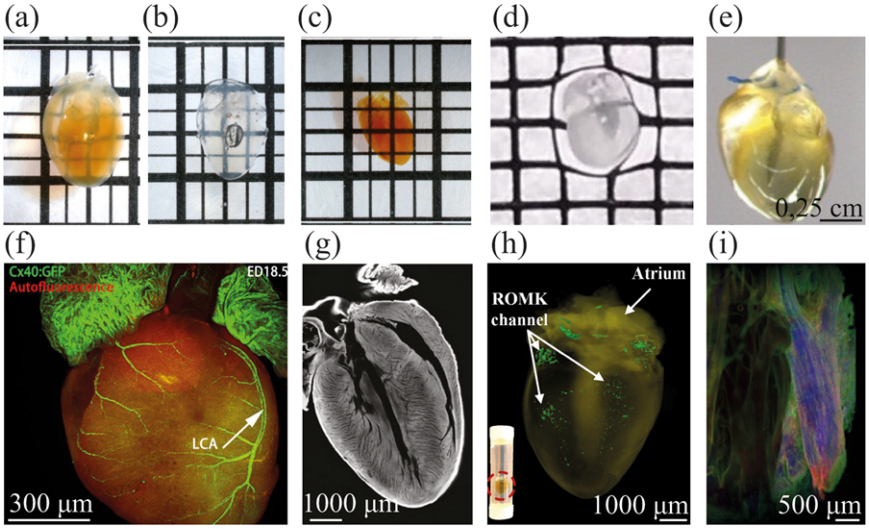

Figure 26. Bright-field and corresponding fluorescence images of cleared murine hearts by: a,f) CUBIC, b) CUBIC-perfusion, c,g) Murray's Clear, d,h) SCM, and e,i) SUT. Although many methods are capable of heart clearing, removal of heme remains the main challenge. Thus CUBIC-perfusion outperforms simple soaking of the heart in CUBIC solution, while addition of cardioplegic solution appear advantageous for organic-solvent clearing (such as Murray's Clear) to ensure that less erythrocytes are entrapped in the walls of the myocardium. TOC of heart can assist visualization of, for example, f) the vasculature, g) the structure of the myocardium, h) GFP-tagged ion channels, and i) proteins labeled by immunochemistry (green: collagen I, red: alpha-tubulin, blue: DAPI). Distance between thickest lines in (a–c) is 1 cm, between lines in (d) is 0.9 mm. a–c) Reproduced with permission.[43] Copyright 2018, Histology and Histopathology. d) Reproduced under the terms of the CC-BY Creative Commons Attribution 4.0 International License (http://creativecommons.org/licenses/by/4.0/).[151] Copyright 2016, The Authors. Published by Springer Nature. h) Reproduced under the terms of the CC-BY Creative Commons Attribution 4.0 International License (http://creativecommons.org/licenses/by/4.0/).[72] Copyright 2017, The Authors. Published by Springer Nature. e,i) Reproduced with permission.[143] Copyright 2018, The Optical Society. f) Reproduced with permission.[141] Copyright 2018, Wiley-VCH. g) Reproduced with permission.[149] Copyright 2015, Future Science Group.

fibrocollagenous connective tissue, while groups of cardiomyocytes are also surrounded by thicker connective tissue—perimysium.[134] In addition, heart contains high amounts of hemoglobin and myoglobin both of which contain heme, an endogenous pigment, which readily absorbs and therefore obstructs penetration of visible light through a cleared, but yet not decolorized, specimen.

The first comparison of five distinct TOC approaches (namely, 3DISCO, CLARITY, Sca*l*e, SeeDB, and CUBIC) to clear embryonic and adult heart was done by Kolesová et al.[135]

The authors concluded that CUBIC was the most suitable protocol, as it cleared both embryonic hearts, embryos and adult hearts, allowing successful imaging and 3D rendering depth of >2.0 mm under general conditions, as also proved by other studies[136,137] (**Figure 26**a,b,f). It might be assumed that the reported CUBIC superiority was caused by its unique decolorizing capability, especially elution of heme chromophore from hemoglobin and myoglobin.[58] The other protocols were suboptimal either because of GFP quenching (3DISCO and CLARITY) or due to a low imaging depth (Sca*l*e, SeeDB). Notably, Kolesová and colleagues[135] also observed that heart immersion in CUBIC reagent 1 alone was sufficient to clear the organ without the need to utilize CUBIC reagent 2 from the original study by Tainaka et al.,[58] the finding confirmed by other groups for other tissues as well.[138,139]

Recently, again using CUBIC method, Nehrhoff et al.[140] established the protocol for whole murine heart clearing and labeling of vasculature (**Figure 27**). Notably, this group also performed TEM analysis, which revealed that BABB-treated heart integrity is severely compromised, when compared with much less extensive deformation observed in CUBIC-treated samples.[140] Transparency achievable in Sca*l*e treated samples, although too low for imaging of adult hearts,[141] is sufficient to study murine hearts at early stages of the embryonic development. As such, application of Sca*l*e by Li et al.[142] allowed to trace lineage of single cardiomyocytes and establish their geometric patterns of division and migration during the trabeculation (a process that increases surface area of myocardium, which is indispensable for proper nutrient and gas exchange) and showed an essential role of *N*-cadherin in maintaining those patterns.

A major drawback of heart clearing by CUBIC is the incubation time, starting from 5 days for embryonic hearts, through 7–14 days for the whole embryos, and finally lasting 30 days for the adult hearts.[135] This significant limitation was recently overcome by Wang et al.,[143] who described SUT (Scheme Update on tissue Transparency). In brief, SUT combines selected chemicals used in CLARITY/PACT methods (8% SDS) and CUBIC (Urea and Triton X-100). Using SUT, the authors reported successful passive clearing of mouse whole-layer left ventricular tissue in 4–6 days, and whole-heart clearing of mouse (40 g body weight, Figure 26e), rat (256 g), and pig (35 kg), in just as little as 2, 4, and 29 days, respectively, by infusing the reagent through the left ventricular chamber. To accelerate the protocol even further, they constructed apparatus for the electrophoretic antibody labeling, which shortened the time required for immunolabeling, when compared with the regular rocking of specimen in staining cocktail (Figure 26i).

Several studies have already implemented BABB clearing protocol to a broad spectrum of cardiac research. Although this research was focused on answering key biological questions or

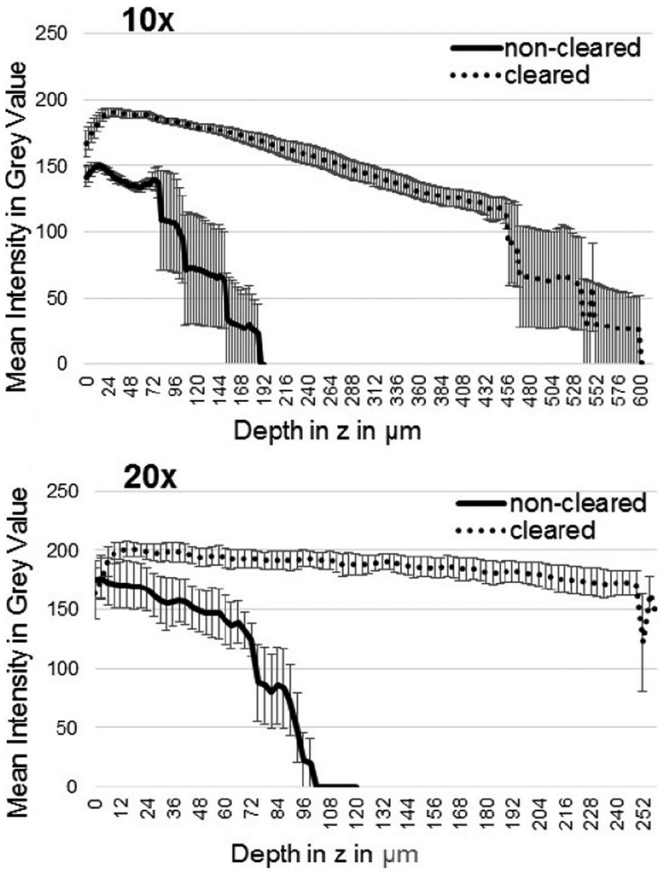

Figure 27. Simple immersion in CUBIC reagents substantially enhances imaging depth of 750-µm-thick sections stained with DAPI. Curves represent mean intensity distribution ± SD of the confocal images acquired with 10× or 20× objectives. Reproduced with permission.[136] Copyright 2016, The Optical Society.

development of LSFM setups, instead of method evaluation, a few conclusions from those studies can be drawn. First, BABB was mainly used to clear petite samples such as embryonic hearts.[144–147] BABB might be also used to clear and image >2.0 mm thick regions of adult mouse heart (Figure 26c,g), as presented by Smith et al.[148] and Sivaguru et al.[149] However, as BABB clearing does not elute heme from tissue, special attention must be paid during the perfusion step to remove as much hemoglobin as possible. Perhaps suboptimal perfusion of hearts studied by Smith and colleagues resulted in high sample absorbance related to uncleared blood clots and heme, which contributed to significant background noise during the image acquisition and, therefore, could impede or even prevent its further analysis. In contrast, addition of cardioplegic solution during the perfusion step, followed by periodic acid Shiff staining allowed Sivaguru et al.[149] to successfully clear and image the entire heart of 3-month-old mouse. Interestingly, this group also performed proof-of-concept study, in which the usefulness of TOC for localization of cells planted on decellularized murine hearts was presented, opening new avenues to study, for example, cancer cells behavior and spatial distribution of metastases in such models. Notably, the entire BABB protocol is inexpensive, does not require any specialized equipment to perform and is rapid, possible to complete within 1 day. In addition, it has to be repeated that the inherent feature of BABB-processed samples is their shrinkage. For heart, the reported linear shrinkage varied greatly, from 5–10% (for adult mouse heart and myocardial specimens[146,148]) to even 81% in the case of developmental stage 29 chick heart.[147] However, it has been generally accepted by all the authors that such shrinkage is almost isotropic and should not affect greatly the overall anatomic relations.[146–148] Recently, Trincot et al.[150] applied other solvent-clearing method, iDISCO, to study lymphatic vasculature in mice. Interestingly, they observed female mice to have significantly more lymphatic vessels than male individuals, regardless of the studied mouse genotype. Subsequently

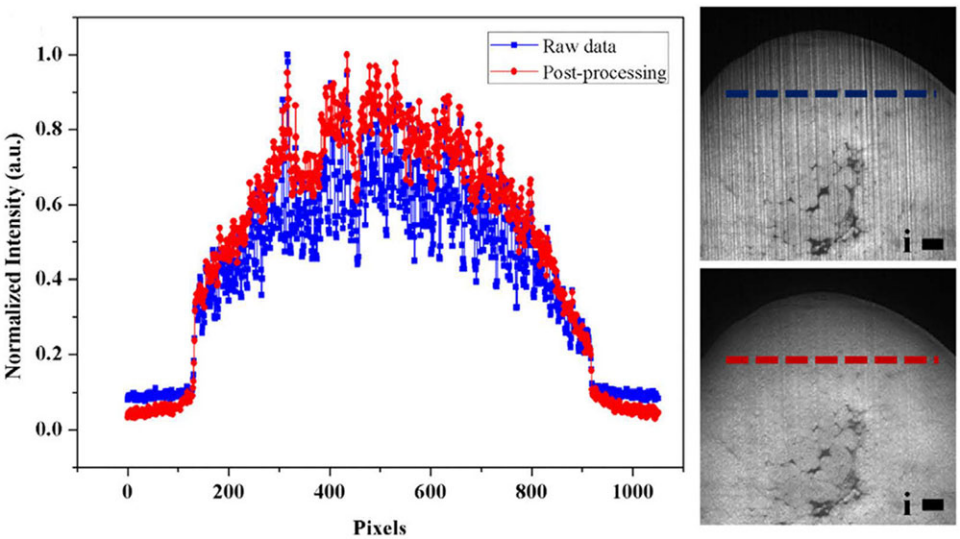

Figure 28. A variational stationary noise remover is an effective tool for the enhancement of LSFM-acquired image quality and stripping artifact removal. Scale bar: 100 µm. Reproduced under the terms of the CC-BY Creative Commons Attribution 4.0 International License (http://creativecommons.org/licenses/by/4.0/).[72] Copyright 2017, The Authors. Published by Springer Nature.

the authors reported overexpression of adrenomedullin (physiological, cardioprotective peptide) in $Adm^{hi/hi}$ mouse to increase the area of lymphatic vessels, thus decreasing the edema and improving cardiac function in the model myocardial infarction.

The next protocol suitable for adult mouse heart clearing is a modification of CLARITY.[72,151] The adaptation proposed by Sung et al.[151] relies on an increase in the concentration of polymerization reaction activator (VA-044), which allows to skip both the electrophoresis and the degassing steps of the original CLARITY. The optimized protocol of Sung and colleagues,[151] termed simplified CLARITY method (SCM), allows to achieve full transparency of hearts within 2–3 weeks (Figure 26d) and preserves signal from genetically encoded GFP. As such, SCM was already applied to study cardiac lineage and protein distribution in the whole adult mouse heart[72,152] (Figure 26h) and spatial rearrangement of fibroblasts after myocardial infarction.[153] Notably, to successfully assess spatial distribution of kidney specific renal outer medullary potassium (ROMK) channels in adult mice, the authors developed dual-sided illumination cardiac LSFM setup.[72] They found that both RIMS and 99.5% glycerol with a 6.3× zoom lens (MVX10) provide almost equal lateral (≈2.8 µm) and *XZ*- and *YZ*-plane axial resolutions (17.4 and 17.9 µm for glycerol, and 17.8, 17.9 µm for RIMS, respectively) measured as the full width at half maximum. Figure 26h presents distribution of AAV-introduced, tagged with single GFP molecule, ROMK channels in SCM-cleared 7.5 months old mouse. The GFP signal was extracted by first excitation at $\lambda = 473$ nm (which apart from GFP signal included heart autofluorescence) and second at $\lambda = 532$ nm (solely autofluorescent signal), while stripping artifacts were reduced with the variational stationary noise remover (**Figure 28**).

Recently, Perbellini et al.[154] described free-of-acrylamide SDS-based tissue clearing method (FASTClear) using 300 µm thick myocardial human and canine sections. FASTClear combines CLARITY and 3DISCO OCAs by applying first SDS as lipid removing agent and then performing tissue dehydration, and finally RI matching in DBE. Although promising, the main drawback of FASTClear perversely remains its long workflow of immunohistochemistry, which takes 3 weeks for 300 µm sections, the shortening of which led to insufficient antibody penetration. Last, RapiClear (RI = 1.49), a commercial water-soluble clearing reagent, was applied to isolated atrioventricular nodes of mouse or 500 µm human sections, which brilliantly delineated the role of macrophages in facilitation of electrical conduction in the heart.[155]

3.2. Skeletal Muscle

Even though the general composition of skeletal muscle tissue might seem similar to myocardium, it contains significantly less blood and hemoglobin after perfusion and fixation, the main molecules which contribute to the light absorbance during deep tissue imaging. However, the autofluorescence remains an issue because of myoglobin and NADH presence, the endogenously fluorescent molecules which limit skeletal muscle tissue imaging especially in ≈488 nm spectrum.[39,156] Moreover, skeletal muscle tissue alone presents with high RI mismatch between muscle fluids (RI = 1.35, 72–80% of muscle weight) and muscle proteins (RI = 1.53, 20–28% of muscle weight).[157,158] Such discrepancies between skeletal and cardiac muscle results in different trends of TOC methods utilization.

Whole-mount enzyme and KOH-based clearing of skeletal muscles aimed at revealing distribution of bone and cartilage have been of great interest for more than 50 years.[159,160] Although harsh and not applicable to perform immunostaining or XFP visualization, these techniques are still in use, even though the new applications are being proposed, such as observation of ectopic calcium deposits in dystrophin-deficient mdx mouse muscles generated upon dietary phosphorus overload.[161] Recently, KOH-based clearing approach was optimized by Sakata-Haga and colleagues,[162] who described the first fast (3 days long), and nondestructive variation of this whole-mount protocol for the efficient clearing and visualization of bone in zebrafish and *Xenopus* frog.

The first modern studies aimed at clearing of unfixed muscle and relied on application of glycerol and glucose as an OCA.[157,163–165] Approximately 10 years later, a newly generated TOC methods were applied to paraformaldehyde-fixed skeletal muscles and bio-artificial muscle constructs.[166–170] Decroix et al.[166] performed the only comparison between three, chemically distinct TOC approaches so far, namely: Clear^{T2}, Sca*l*eA2 (one of the Sca*l*e reagents), and 3DISCO. The latter protocol outperformed other techniques in every parameter tested. Treatment of such muscles as quadriceps and gastrocnemius dissected from β-actin-GFP reporter mice with 3DISCO led to good optical transparency, while tissues processed with both Clear^{T2} and Sca*l*eA2 macroscopically seemed almost intact. Moreover, 3DISCO was the fastest as it took only 4 h in comparison to 13 h and 2 weeks of Clear^{T2} and Sca*l*eA2 treatment, respectively. Macroscopic transparency of tissues was confirmed by confocal imaging with recorded penetration depths of ≈160, ≈180, ≈310, and ≈400 µm for the uncleared, Clear^{T2}, Sca*l*eA2, and 3DISCO treated samples, respectively (**Figure 29**a). The achieved imaging depth with 3DISCO becomes even more impressive, when the clearing impact on tissue size is considered. As observed, 3DISCO caused ≈20% linear shrinkage of sample, which means that the effective imaging depth obtained was around 500 µm from the surface. Explanation of such a good performance of 3DISCO cannot be based solely on comparison of the refractive indices of muscle and imaging media of the rest of tested methods. Taking natural RI mismatch between muscle fluids and muscle proteins into account, it might be speculated that the crucial advantage of 3DISCO is the removal of inherent heterogeneity of muscle RI and then matching of "dried" muscle proteins (RI = 1.58) by immersion in DBE (RI = 1.56). By coupling electrophysiological examination with Alexa Fluor 647-conjugated α-bungarotoxin injection (competitive antagonist of nicotinic acetylcholine receptors), after which the muscles were subjected to 3DISCO clearing, Yin et al.[171] performed detailed study on motor endplates in a variety of mouse muscles, their distribution under physiological conditions and remodeling in the model of denervation and nerve repair. Based on the acquired data, the authors suggested that skeletal muscles should be divided into more separate functional fields to reflect substantial differences of the motor endplates distribution. The sisterly method of clearing and optimized immunolabeling, iDISCO, was already applied for whole-mount staining and imaging of skeletal muscles and diaphragm, in particular.[172,173]

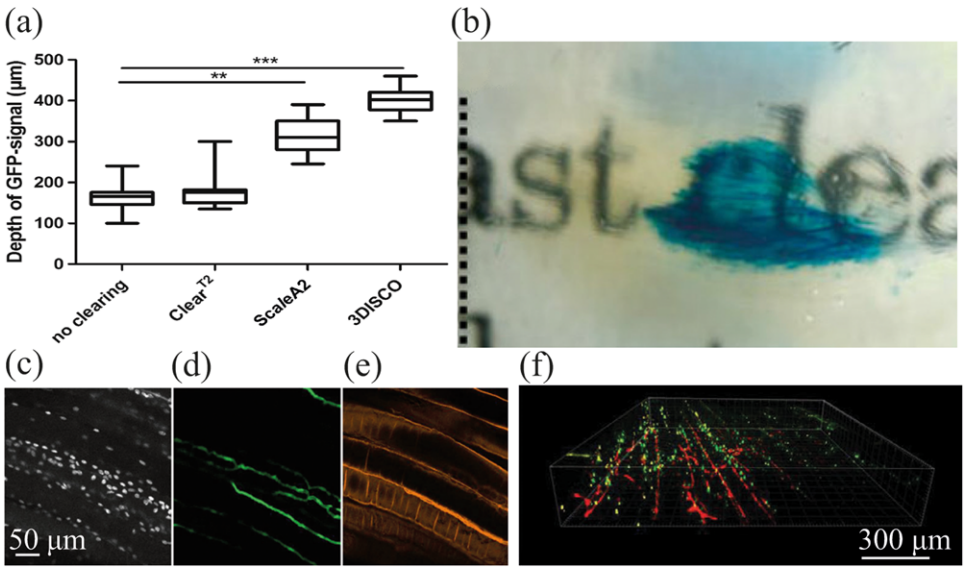

Figure 29. 3DISCO, CUBIC, and CLARITY are capable of skeletal muscle clearing. a) 3DISCO outperforms hyperhydrating Scale and Clear^{T2} in terms of imaging depth. Note that the true imaging depth of 3DISCO-treated samples is even higher, as the tissue shrinks during the clearing process. Reproduced with permission.[166] Copyright 2015, Taylor & Francis. b) Combined CLARITY/CUBIC clearing allows for the identification of a LacZ reporter after X-gal staining, as well as c–e) immunochemistry ((c): DAPI/nuclei, (d): Flk-1^{+}/GFP reporter/blood vessels, and (e): laminin/myofibers and membrane of the blood vessels, images present maximum intensity projection of 15 × 1 µm slices). b–e) Reproduced with permission.[168] Copyright 2016, Springer Nature. f) Passive skeletal-muscle CLARITY retains epitopes in skeletal muscle and allows for immunostaining and imaging up to 250 µm (red: CD31/blood vessel, yellow: NeuN/neurons, green: tyrosine hydroxylase/muscle bundles). Reproduced with permission.[169] Copyright 2018, Royan Institute, Iranian Academic Center for Education Culture and Research (ACECR).

Visualization of motor endplates was also one of the aims of recently reported modifications of CLARITY.[167,169,174] Milgroom and Raltson[167] were the first to propose CLARITY scheme designed to clear muscles relying on muscle isolation, incubation in fixative/acrylamide, bis-acrylamide hydrogel solution and finally a brief, 8-h lasting electrophoresis with 23 V applied electric field, which was the highest tested voltage, that did not cause the sample heating above 50 °C. The presented results are concise, showing an increase in the imaging depth of up to only 97 µm in comparison to untreated muscle and no staining or XFP imaging besides nuclear stain, Hoechst 33342 (**Table 1** summarizes specificity and application of stainings used with TOC), was provided. However, more recent report of Zhang et al.[169] demonstrating modified passive CLARITY for skeletal muscle addressed most of the mentioned shortages. The authors were able to show successful immunostaining of three antibodies simultaneously (tyrosine hydroxylase, CD31, and NeuN, Figure 29f) and obtained 250 µm, a 2.5-fold increase in the imaging depth, when compared to Milgroom and Raltson reports. Although the procedure is carried out at 37 °C, it does not utilize electrophoresis and therefore should reduce the protein loss during the clearing (however, comparable data were not shown); the lack of electrophoresis on the other hand contributes to the main weakness of this method, which is a 40-day-long clearing time. This rises the questions about the XFP stabilization over such a long time course and also preservation of tissue structure, which again was not provided by either Milgroom[167] or Zhang.[169] Both studies were also unsuccessful with α-bungarotoxin staining of nicotinic acetylcholine receptors, which was attributed to PFA fixation and formation of hydrogel mesh that could hamper contact with the receptors. This was, however, reinvestigated by Williams et al.[174] who showed that loss of α-bungarotoxin staining is neither because of PFA fixation nor hydrogel mesh formation, but utilization of SDS during the step of lipid removal. By using a newly developed, SDS-free pipeline termed MYOCLEAR, the authors were able to reach imaging depth of 700–800 µm and count total number of neuromuscular junctions within unsectioned extensor digitorum longus muscle.

Another interesting approach was proposed by Verma et al.,[168] to combine muscle clearing with LacZ reporters that encode β-galactosidase enzyme, which benefits from both high signal-to-noise ratio and stability over time. They present several detailed protocols for muscle clearing, immunolabeling (Figure 29b–e) and LacZ detection, which are based on CUBIC and CLARITY OCAs. Although not quantified, based on provided macrophotography (Figure 29b), it might be estimated that tissue transparency is compelling, while its size does not change remarkably.

3.3. Skin

The skin is a complex tissue, consisting of many layers with randomly distributed inhomogeneous light scatters such as melanin dust, melanosomes and high-order collagen structures and elastic fibers.[175,176] Although for many years in vivo optical clearing of skin using biocompatible agents such as glycerol, DMSO, and PEG400 remained in the center of interest,[177,178] a few modern methods have already been applied to test fixed tissue imaging and immunolabeling performance.[179,180] Liang et al.[180]

Table 1. Summary of the stainings that proved compatible with TOC methods with their utilization in exemplary studies.

Name of the dye/staining	Staining selectivity	Excitation/emission maxima [nm]	Ref.
Alizarin Red	Calcific deposition	530-60/580	[317]
Basic fuchsin	Chromosomal DNA; lignin in plant tissue samples	561/593	[190]
DAPI	Nuclear and chromosome counterstain	358/461	[143,168,195,284]
DiD	Lipophilic membrane stain (red-shifted DiI analog)	644/665	[196]
DiI	Lipophilic membrane stain	549/565	[186]
EdU staining	Proliferating cells (is efficiently incorporated into newly synthesized DNA)	NA (requires conjugation)	[204]
Heidenhain's Azan stain	Often used for staining connective tissue and epithelium. Nuclei are stained bright red; collagen, basement membrane, and mucin are stained blue; muscle and red blood cells are stained orange to red.	NA	[203]
Hoechst 33342	Emits fluorescence, when bound to dsDNA	350/461	[167]
Hoechst 34580	Emits fluorescence, when bound to dsDNA-selective	392/440	[186]
Isolectin	Variety of applications; Cao et al. used to stain blood vessels (binds to sugar residues of the glycocalyx in blood vessels)	NA (requires conjugation)	[278]
Nile Red	Used to localize and quantitate lipids	552/636 (in methanol)	[180]
Periodic acid-Shiff stain	Basement membrane, glycogen, some mucins, mucopolysaccharides, fungal cell wall	NA	[149]
Phalloidin	Filamentous actin (F-actin)	NA (requires conjugation)	[186]
Propidium iodide	DNA (a nuclear and chromosome counterstain)	493/636	[58]
SYTO 16	Nucleic acids	488/518 (DNA), 494/525 (RNA)	[58,70]
Villaneuva's Osteochrome Bone stain	Bone (e.g., osteoblasts, osteocytes)	561/593	[190]
Wheat germ agglutinin	Binds to sialic acid and *N*-acetylglucosaminyl	NA (requires conjugation)	[185]

described CUBIC protocol suitable for whole-mount clearing and staining allowing single cell resolution confocal investigation of, for example, basal and proliferating keratinocyte populations in the interfollicular epidermis and in the hair follicle, 300 µm deep into the tissue (**Figure 30**e). The entire procedure takes 12 days and keeps all of the CUBIC's inherent features such as non-toxicity, ease of handling and imaging. Additionally, they observed CUBIC skin clearing compatibility with Nile Red (lipophilic dye) staining and therefore were able to visualize sebaceous glands (Figure 30f). CUBIC is, however, ineffective agent for melanin-containing tissues clearing, such as iris and hair,[59] which is of significance in case of skin clearing and should be addressed in further studies.

Abadie et al.[181] investigated various solvent-based protocols (3DISCO, ethanol-BABB, ethanol-DBE) and Sca*l*e for clearing of human skin biopsies (**Figure 31**). Although both 3DISCO and ethanol-DBE were equally fast to achieve transparency, they were relatively modest when compared with ethanol dehydration followed by incubation in BABB, which allowed for in-depth 3D imaging of skin compartments and appendages (Sca*l*e did not clear skin even after months of incubation).[181] This, however, partially contradicts brief, comparative study between dehydrating methods and CLARITY performed by Azaripour et al.[182] They macroscopically observed that both electrophoretic and passive (11-week long) variants of CLARITY are not suitable for mouse skin clearing (Figure 30c,d), while succinct treatment with either 3DISCO or iDISCO lead to full optical transparency within 2.5 days (Figure 30a,b).

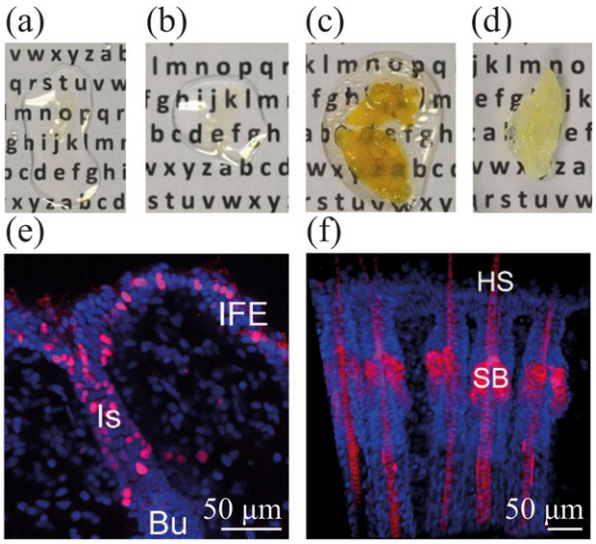

Figure 30. TOC of mouse-skin biopsies. Successful clearing of mouse skin was achieved by: a) Murray's Clear and b) iDISCO (immersed in DBE), but neither: c) electrophoretic nor d) passive variant of CLARITY (incubated for 11 weeks). a–d) Reproduced under the terms of the CC-BY Creative Commons Attribution 4.0 International License (http://creativecommons.org/licenses/by/4.0/).[182] Copyright 2016, The Authors. Published by Springer Nature. e) CUBIC is applicable to skin and allows visualization of, for example, Ki67-positive (marker of cell proliferation) keratinocytes and f) Nile Red–stained sebocytes. IFE: basal interfollicular epidermis; Is, isthmus region of the hair follicle; Bu, bulge of the hair follicle; HS, hair shaft. e,f) Reproduced with permission.[180] Copyright 2016, My JoVE Corporation.

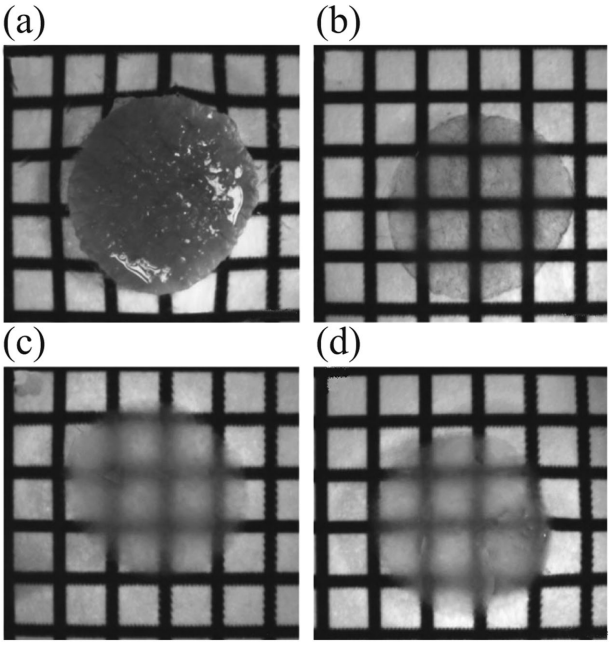

Figure 31. Comparison of organic-solvent methods for human skin biopsies. 8-mm-thick formalin-fixed human skin biopsies were treated with: a) PBS, b) ethanol-BABB/Murray's Clear, c) THF-DBE/3DISCO, and d) ethanol-DBE. Based on this, BABB should be used as RI-matching solution for such samples. Grid width: 2 mm. Reproduced with permission.[181] Copyright 2018, Springer Nature.

3.4. Bones and Connective Tissue

Bone is a heterogeneous tissue that contains solid mineral (along with soft, marrow components) and connective tissue, both of which are characterized by relatively high RIs of 1.55[183] and 1.47,[184] respectively. So far, few chemically distinct TOC methods were assessed for their clearing utility, namely, SeeDB,[185,186] CUBIC decalcification,[61] dehydrating methods,[57,187] Bone CLARITY,[188] and tuned Sca*l*eS formula for clearing of the organ of Corti[189] (**Figure 32**). In complementary studies performed by Neu[186] and Calve[185] on osteochondral tissue, 2.5-mm thick murine and bovine samples of ligament and meniscus were treated with SeeDB. Macroscopically, a satisfying transparency was achieved in the case of cartilage and meniscus, which was further confirmed by DiI and Hoechst 34580 labeling allowing for 200–300 µm deep imaging in comparison to ≈50 µm deep for untreated controls, while blood-rich subchondral and bone regions remained opaque and thus were excluded from the microscopic analysis. Immunolabeling was unsuccessful, as no specific signal could be detected at 200 µm depth. However, this might be attributed to a high molecular weight of primary antibodies, as both Neu and Calve were successful, when stainings with AlexaFluor-conjugated low molecular weight phalloidin (the F-actin stain) and wheat germ agglutinin were performed. In addition, using scanning electron microscopy, Neu with colleagues further demonstrated that SeeDB optical clearing does not alter general articular cartilage structural morphology and porosity (represented as pore area fraction).

The most comprehensive comparison of eight different TOC methods, for which RI varied from 1.45 (for Visikol) to 1.56 (for THF-DBE), for bone and joint clearing was conducted by Berke et al.[190] Detailed measurements of the average percent light transmittance and fold decrease in the number of scattering events have clearly shown that in general the higher the RI of clearing medium, the better optical properties of bone and connective tissue (Figure 32a). The only relatively low RI-bearing clearing agent, TDE (RI = 1.47), performed better than could be assumed (e.g., better than SeeDB of RI ≈1.49–1.50). As TDE significantly differs from other low RI-bearing solutions in terms of water content (only 3% vs 20–75%), it apparently strengthens reports that joints (collagen) clearing mechanisms rely not only on RI matching, but also on sample dehydration.[191] By applying basic fuchsin (BF) and Villaneuva's Osteochrome Bone Stain (OC), they observed dehydration methods (THF-DBE, ethanol-BABB and Murray's Clear) to be comparably effective, allowing to reach ≈250 µm in imaging depth. Although all listed dehydration methods were previously reported to quench fluorophores, in case of BF and OC staining only THF-DBE (3DISCO) resulted in a significant decrease in fluorescent signal intensity. However, this observation is contradicted by Acar et al.,[187] who reported that it is 3DISCO, which preserves endogenous fluorescence better, but yields lower transparency, as compared with Murray's Clear. Therefore, it seems advisable to check both protocols with particular specimens and fluorophores, before proceeding to the main experiment. Evidence obtained also from the Murray's Clear-processed mouse bone and bone marrow followed by in situ LSFM imaging served as a substructure of a revised model of megakaryopoiesis, in which spatial distribution of megakaryocytes depends upon architecture of vasculature, not the maturity of cells.[192] Very recently, the same group presented a detailed pipeline for the efficient bone decalcification, clearing, imaging and post processing of LSFM-derived images.[193]

The suitability of dehydration methods for other hard, connective tissue, gingiva, accompanied by successful anti-CD31 staining, was also reported by Azaripour et al.[194] A group led by Gradinaru[188] has recently contributed to the development of bone-specific CLARITY protocol. As compared to original CLARITY, Bone CLARITY possesses two additional steps for removal of: 1) minerals, the main bone scatterers (e.g., calcium hydroxyapatite of RI = 1.63–1.65) and 2) heme. Therefore, the Bone CLARITY workflow consists of EDTA-mediated decalcification, acrylamide mesh formation, decolorization with Quadrol (first described as CUBIC decolorizing and heme-removing agent), and finally immersion and dual-sided LSFM imaging in RIMS (refractive index matching solution) with 10× CLARITY objective (0.6 NA, Olympus XLPLN10XSVMP, with adjustment of correction collar to RI of RIMS). Major drawbacks of Bone CLARITY are long incubation time (28 days) and requirement of using highly specific instrumentation and computational pipeline for ≈500 GB generated files. Moreover, immunolabeling, although possible, requires further modifications to allow fast and, most of all, deep antigen localization. However, the mentioned limitations are readily compensated by the excellent transparency and well-tested GFP preservation, both of which allow for imaging of the entire murine bones, as long as 1500 µm deep into the tissue (Figure 32c).

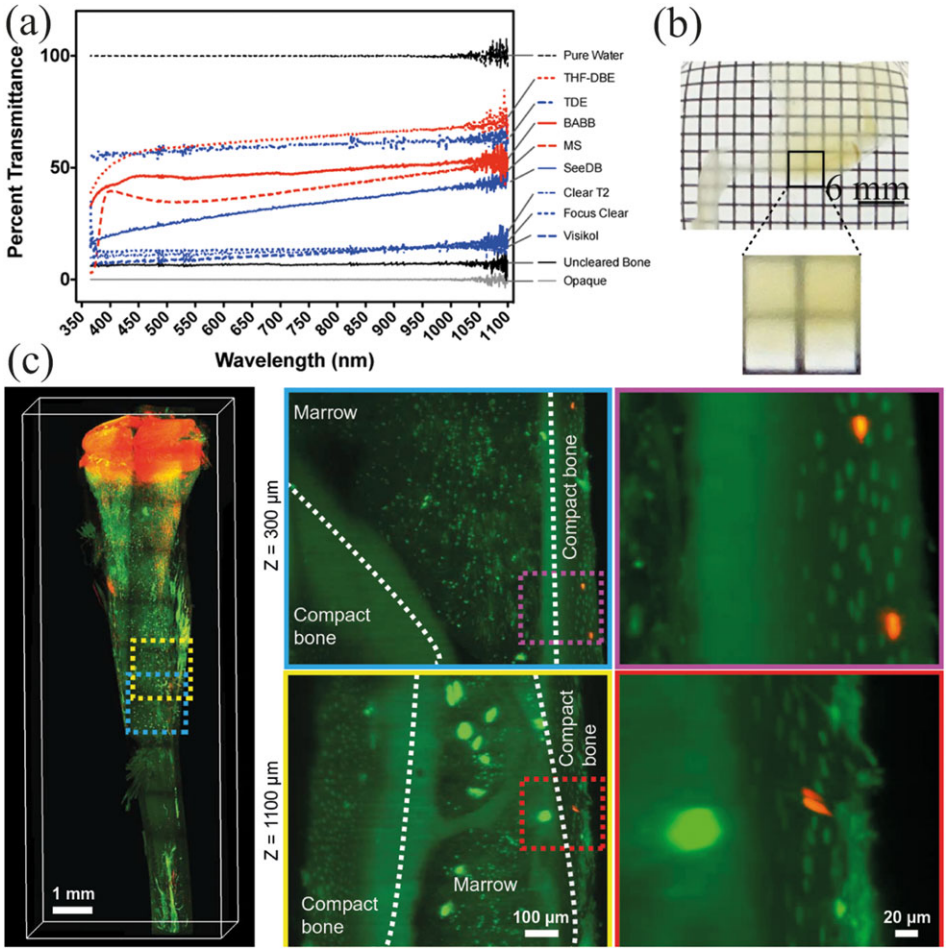

Figure 32. TOC methods for murine bone clearing. a) In general, the higher the RI of the final solution, the better the transparency of bone; thus organic solvents such as 3DISCO and Murray's Clear are better than other methods. Reproduced under the terms of the CC-BY Creative Commons Attribution 4.0 International License (http://creativecommons.org/licenses/by/4.0/).[190] Copyright 2016, The Authors. Published by PLOS. b,c) Addition of EDTA-mediated decalcification, however, allowed for successful clearing of adult hindlimb with CUBIC-B (b) or Bone CLARITY (c). Bone CLARITY preserves the endogenous fluorescent signal and achieves subcellular resolution during the entire imaging process, for example, for a tibia (red: tdTomato positive multipotent osteoblasts from Sox9CreER transgenic mouse line, green: autofluorescence). b) Reproduced under the terms of the CC-BY Creative Commons Attribution 4.0 International License (http://creativecommons.org/licenses/by/4.0/).[61] Copyright 2018, The Authors. Published by Elsevier. c) Reproduced with permission.[188] Copyright 2017, The American Association for the Advancement of Science.

Altogether it seems that efficient immunolabeling still remains a major challenge to be resolved and that BABB and Bone CLARITY are equally reasonable to be applied for bone tissue clearing.

3.5. Intestines

Intestine is a complex organ, composed of many specialized cells and distinct tissues (connective, epithelial, muscular, and nervous). Additionally, it has highly fragile structures, such a villi and mesenteries. Therefore, its optical clearing is challenging, as it should reveal various tissue types, while being gentle enough not to alter delicate histo-architecture. The first comparative study evaluating three distinct TOC techniques including glycerol, TDE, and BABB, was performed by Appleton et al.[195] A 97% TDE solution turned out to be superior over other methods in almost every aspect—it yielded maximal imaging depth (180–200 µm) of the microscopy setup used (40×, 1.3 NA, W.D. 220 µm, oil-immersion S Fluor Nikon), compatibility with DAPI and immunostaining of several epitopes, long-term sample stability, neither observable autofluorescence (which was remarkable in case of BABB-cleared tissues) nor tissue deformation. The only advantage of BABB over TDE was stability of phalloidin staining, but only when ethanol, not methanol, was used during dehydration step. Glycerol solution did not prove to be preferred under any of the tested conditions.

Starting from 2009, the group led by Tang[196] has performed copacetic series of studies appraising versatility of FocusClear (RI = 1.45–1.46) for both basic and clinical research on intestines. In a sequence of studies this group convincingly demonstrated that FocusClear could be effectively applied to image every tissue type of murine and human intestines, with a cellular resolution in 3D fashion, allowing discrimination of epithelium,[196] blood vessels,[197] and nervous tissue,[198] under both normal and pathological conditions (**Figure 33**).[199] This imaging has eventually led

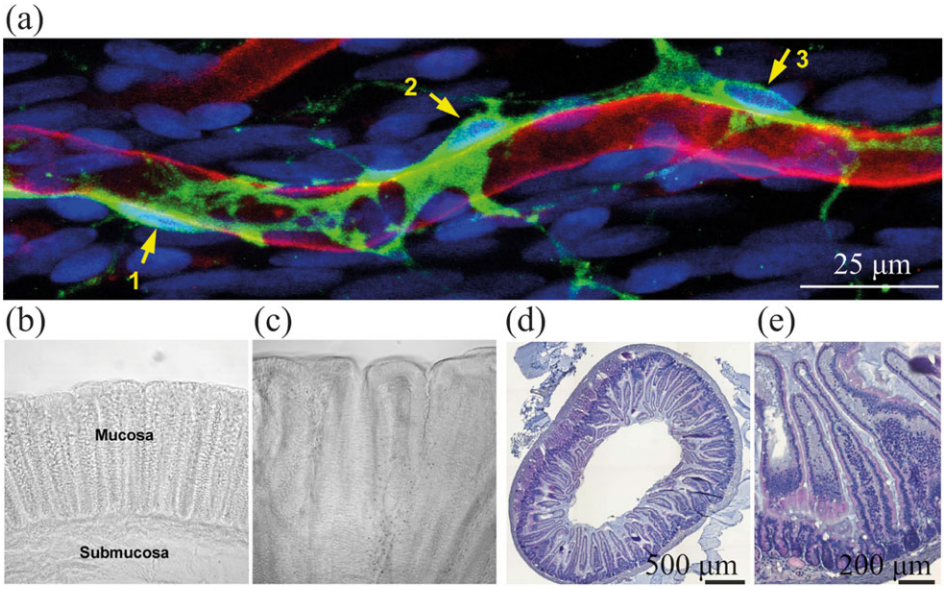

Figure 33. Application of TOC to mouse intestine tissue. a) TOC of the intestine allows us to describe new subclass of interstitial cells of Cajal, the perivascular (marked with arrows, green: c-kit, red: CD31, blue: SYTO16). b,c) FocusClear is applicable for clearing of normal mucosa (b) and colorectal carcinoma (c). d,e) Although fragile, the structure of the intestine can be fully preserved during PACT clearing as confirmed by an H&E stain. a) Reproduced with permission.[200] Copyright 2014, Elsevier. b,c) Reproduced under the terms of the CC-BY Creative Commons Attribution 4.0 International License (http://creativecommons.org/licenses/by/4.0/).[199] Copyright 2013, The Authors. Published by PLOS. d,e) Reproduced under the terms of the CC-BY Creative Commons Attribution 4.0 International License (http://creativecommons.org/licenses/by/4.0/).[203] Copyright 2016, The Authors. Published by Springer Nature.

to, for example, identification of a new, perivascular type of interstitial cells of Cajal in human colon[200] (Figure 33a) and enabled visualization of the enteric glia.[201]

It needs to be emphasized that FocusClear was compatible with nuclear dyes SYTO 16 and propidium iodide (PI), and immunostaining and unconventional stains such as gold nanorods or DiD (4-chlorobenzene sulfonate salt). It also preserved XFP proteins (e.g., in phosphoglycerate kinase 1 [PGK-1]-driven GFP and nestin-GFP transgenic mice), reached clearing plateau within as little as 30 min and outperformed other possible OCAs such as DMSO and glycerol in terms of achievable intestine transmittance (**Figure 34**). Another aqueous solutions tested for intestine clearing are SeeDB and Sca*l*eA2, which led Liu et al.[202] to develop deep mucosal imaging (DMI) approach, relying on pros and cons observed for each of the two techniques. The most notable was the observed stability of genetically-encoded fluorescent proteins. Although both protocols lead to a significant decrease of fluorescent signal, this effect is much more pronounced in the case of SeeDB-treated samples (fourfold signal decrease in membrane-localized tdTomato and about fivefold decrease in cytoplasmic GFP vs control). However, XFP instability was reported as the only weakness of SeeDB, when compared with Sca*l*eA2, which led to ≈25% sample expansion (based on interstitial crypt cross-sectional areas), greater clearing and immunochemistry times. Therefore, it was advised by the authors to perform preliminary studies with SeeDB and switch to Sca*l*eA2 only when fluorescent protein signal is too weak for particular study design.

A more recent report by Neckel et al.[203] provides a comprehensive test on CLARITY-related techniques for mouse intestine clearing and deep imaging. The two tested methods were original CLARITY and PACT. Besides excellent transparency and successful staining with over 10 antibodies, by performing hematoxylin-eosin (H&E) and Heidenhain's Azan stain, they provided critical and most detailed information about preservation of tissue histo-architecture, showing that it is PACT, but not CLARITY, to fully preserve it (even microvilli, Figure 33d,e). This conclusion was further supported by electron microscopy. However, two serious imperfections of this approach remain—long protocol time (clearing lasts for 12–14 days) and incubation at 60 °C, which although not reported, most probably will prohibit later identification of endogenous XFP markers.[94] A recent, brief report from Kaufman et al.[204] proposed a specific protocol for Click-iT EdU staining and imaging of mitotic cells in transparent murine intestine. It relies on clearing with Triton X-100/DMSO solution and further incubation in iohexol-based refractive index matching solution, proposed by Yang et al.[38]

It has to be mentioned that optically cleared and imaged samples provide researchers with huge datasets (often extending far beyond 500 GB) and thus raising a further challenge of their proper processing. One computational solution allowing automatic data analysis routine of LSFM acquired images of the unsectioned (cylindrical) intestine samples was proposed by Candeo et al.,[205] who developed a MATLAB code for virtual unfolding of such datasets. As a result, transparent intestine does not have to be cut prior to the procedure and can be imaged in its native shape and later analyzed in a layer by layer fashion.

3.6. Pancreas

Pancreas is yet another fragile and complex organ of the gastrointestinal system, with the structure determined by characteristic

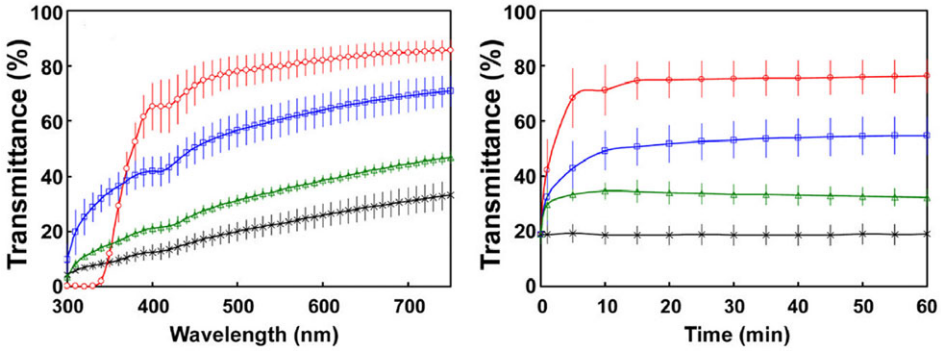

Figure 34. FocusClear (red) outperforms DMSO (green) and glycerol (blue) as a clearing agent for mouse intestines (black: control group in phosphate-buffered saline). Reproduced with permission.[196] Copyright 2009, Elsevier.

dual functions performed by exocrine and endocrine cells. Like for the intestines, the most comprehensive research on optically cleared pancreas comes from Tang and co-workers,[206] utilizing FocusClear and RapiClear as OCAs. In a series of studies, these commercial reagents were demonstrated to be suitable for rapid (90-min long to overnight) clearing and immunostaining (taking 1–2 days) of 400 µm thick slices of both murine and human pancreas.[207,208] The reported 3D visualization of pancreas provided multiple critical insights into islet vascular network,[209] sympathetic innervation,[210] and its significant remodeling in a variety of murine models of diabetes,[210] insulitis,[211] hyperphagic obesity,[212,213] duct lesion,[214] and 3D histology of microstructure, vasculature and sympathetic innervations of mouse islet grafts placed under the kidney capsule.[215,216] In all of the aforementioned studies, FocusClear allowed for ≈400 µm deep imaging with subcellular resolution, was compatible with vascular staining with either fluorescent lectin[211] or DiD[209] and preserved fluorescent signal of genetically encoded fluorophores. FocusClear was also used as an imaging medium by Muzumdar et al.[217] after electrophoretic variant of CLARITY, which assisted discovery of the role of p53 loss during initiation and expansion of low-grade pancreatic intraepithelial neoplasia. However, the newly presented modification of PACT revealed successful tracing of human pancreas neuro-insular network by immunochemistry with RIMS, as an imaging solution.[218] The major limitation of FocusClear persists its high cost, which stimulates other groups to search for the alternatives.[219]

Recently, Fowler et al.[220] adapted 3T method (transparent tissue tomography) to image human pancreas in detailed, yet inexpensive fashion. This approach relies on a brief tissue fixation, preparation of large, 600–1000 µm thick sections with vibratome, followed by short, overnight antibody staining and finally a 1-day only clearing by sequential incubation with solutions of D-fructose. Using this approach, it was possible to complete within 3 days staining and imaging up to 600 µm depth of 4 different epitopes at once, which granted detailed confocal imaging of spatial relationship between β, α, and δ cells with vascular context. In addition, D-fructose solutions were also shown to be feasible to clear snap-frozen tissues kept at −80 °C for several years, which further expands the utility of this novel and certainly rapid approach. Interestingly, 3T method was recently applied to study spatial pharmacokinetics of anti-PD-L1 antibody (one of the checkpoint inhibitors clinically approved for cancer immunotherapy) and distribution patterns of both anti-PD-L1 and PD-L1 in murine models of lung and mammary carcinoma.[221]

Similarly to intestines, along new TOC protocols, a computational segmentation workflows are being developed to aid interpretation of large datasets and assist during comparison of different organizations of multicellular structures or direct cell-to-cell interactions.[222] To summarize, FocusClear should be highlighted as the well-tested, deeply rooted technique for pancreas optical clearing, but the role of novel OCAs should also not be underestimated. However, these require further examination and particular attention should be paid to evaluate possible tissue deformation, which was not reported in sufficient detail.

3.7. Stomach and Esophagus

Until now, the TOC methods were only sparingly applied for stomach and esophagus, with apparently a single brief report focusing on the mentioned organs. It utilized LUCID (lLUmination of Cleared organs to IDentify target molecules), a clearing protocol based on TDE and originally applied to brain tissue.[82] Application of modified LUCID to porcine samples of stomach and esophageal mucosa and superficial submucosal layer took less than a week to complete and increased tissue imaging depth significantly, up to ≈400 and ≈650 µm, respectively.[223] However, it is unclear to what extent is this approach compatible with immunochemistry, as only staining with anti-Ki-67 nuclear antigen antibody was performed on histological slices of formerly cleared tissue.

3.8. Liver

Application of passive TOC to liver, the last gastrointestinal organ reviewed herein, is still scarce, especially when compared with liver transparency upon whole-organ and whole-body clearing techniques. This evident difference might be due to: 1) very high liver blood flow, which under physiological conditions accounts for ≈30% of the resting cardiac output and likely enhances the effect of perfusion-based clearing,[224] 2) the size of

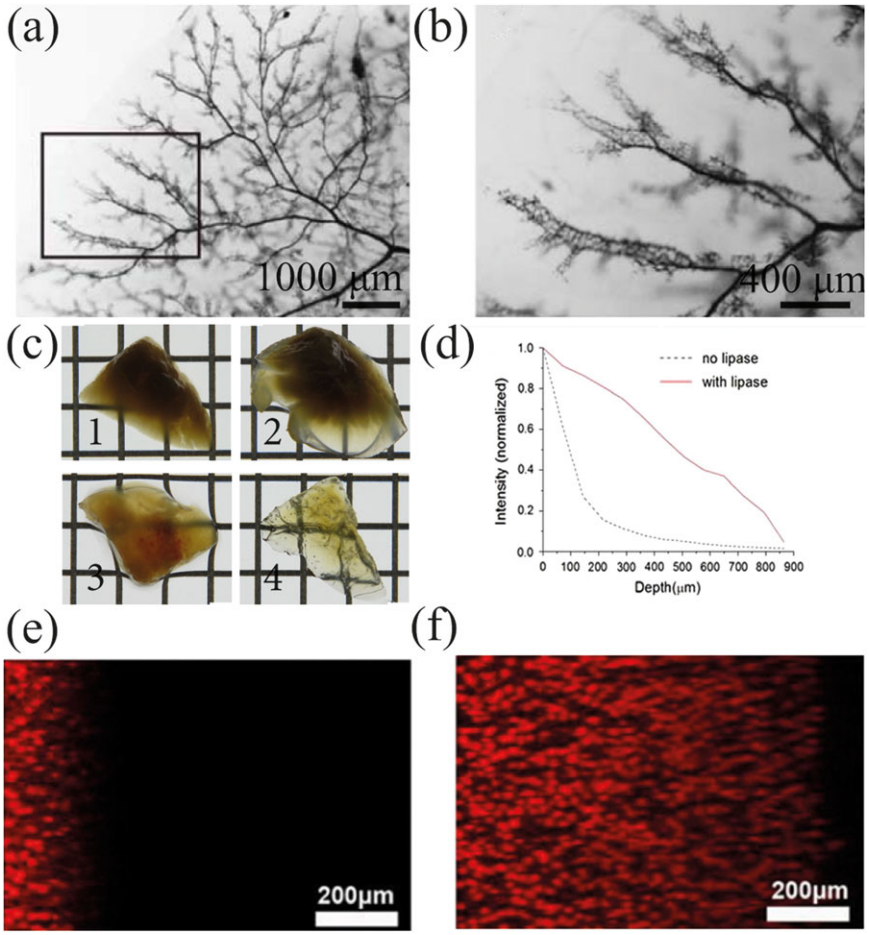

Figure 35. Representation of TOC application for liver imaging. a) Organic solvents clear the liver rapidly and are compatible with carbon ink injected into intrahepatic bile duct thus can be used to describe patterns of its development; b) magnified area. a,b) Reproduced with permission.[229] Copyright 2018, Wiley-VCH. c) Bright-field images of liver lobes in: 1) PBS and cleared with 2) Clear^{T2}, 3) SeeDB, and 4) CUBIC (scale bar: 1 mm), with the latter method allowing for deep, up to 1500 μm, imaging. c) Reproduced under the terms of the CC-BY Creative Commons Attribution 4.0 International License (http://creativecommons.org/licenses/by/4.0/).[232] Copyright 2016, The Authors. Published by PLOS. d) Lipase treatment increases transparency of thick liver sections, as confirmed by transmittance curves. e) 1-mm-thick mouse liver section CLARITY-cleared without and f) with addition of lipase treatment for the extensive lipid removal (red: Hoechst stained nuclei). d–f) Reproduced with permission.[234] Copyright 2017, Oxford University Press.

the liver, which is the biggest solid organ of mice, with relatively low surface-area-to-volume ratio,[225] or 3) combination of both. Nonetheless, a few studies did establish and utilized TOC methods for the enhanced, 3D imaging of liver,[226,227] with the main formula being BABB.[228–231] Such approaches allowed for precise macroscopic visualization of the whole architecture of the mouse biliary tree (**Figure 35**a,b) during both disease and development, when ingeniously combined with carbon ink.[229,230] Although BABB clearing of liver can encouragingly be achieved within 1 day, no further data about its applications, microscopic imaging depth, and possible limitations were presented. Fumoto et al.[232] compared liver transparency in CUBIC, SeeDB, and Clear^{T2}-treated samples to evaluate compatibility of organ TOC with gene delivery systems (Figure 35c). The observable depths of plasmid-injected ZsGreen were 70, 200, 240, and 1000 μm for PBS, Clear^{T2}, SeeDB, and CUBIC, respectively, with the latter clearing taking 10 days to complete. Additional examination by injection of two plasmids, encoding ZsGreen and tdTomato fluorescent proteins revealed that ZsGreen can be imaged deeper into the tissue (1500 μm vs 1200 μm) with the latter being also less photostable, when placed in CUBIC reagent 2. These results are corroborated by a further study of the same group led by Nishimura et al.[233] who also performed SeeDB and Clear^{T2}-based liver clearing post gene transfection using bubble liposomes with ultrasound irradiation, achieving only modest transparency allowing for ≈100 μm in depth examination of the peritoneal tissues. However, this was sufficient to reveal spatial distribution of transgene expression pattern and lack of non-target parenchymal cells staining.

The most recent study and the only one developing truly liver-specific TOC method comes from Lai et al.[234] In the proposed approach, the standard CLARITY method is supplemented with lipase treatment (Figure 35d). This is based on the well-known abundant presence of lipid droplets in liver (due to, e.g., sterol synthesis) containing highly hydrophobic core, which on the contrary to cellular membrane phospholipids, are not effectively removed by the usually used Triton X-100 and SDS as OCAs detergents. Although not detailed, this report readily presents

augmentation of liver transparency upon lipase treatment both macro- and microscopically (Figure 35e,f), which doubles imaging depth of Hoechst 33342 stained 1-mm thick samples (as inspected by Nikon A1Si confocal with CFI Plan Apo 10×, 0.45 NA, W.D. 4.0). Therefore, addition of sample incubation with lipase should be perceived as a potentially valuable step to be added for clearing also with other than CLARITY techniques and of other than liver, lipid-rich organs, such a kidney, muscle, and of course adipose tissue.

3.9. Immune Organs (Lymph Node, Spleen, Thymus)

The immune system is unique in terms of its cellular organization. Cells of the innate and adaptive immunity constantly circulate throughout the body and their tissue location and functions dynamically change. This highly migratory behavior of lymphocytes makes imaging studies very challenging. So far, the vast majority of studies investigating quantitative and qualitative alterations within lymphocyte subpopulations relied on flow cytometry. However, such analysis is deprived of any structural context and requires prior manual organ meshing for cells isolation, which is imperfect and might lead to underestimation of cells, especially tightly bound to stromal components of organs, such as dendritic cells.[235]

Recent progress in TOC and imaging opens new avenues to study cells phenotype and distribution within transparent, entire intact lymph nodes, an approach called histocytometry. Until now FocusClear,[236] CUBIC,[237] SeeDB,[238] CLARITY,[239] BABB,[240–242] and uDISCO[243] were used for lymph nodes clearing, with one study describing a completely new method for their clearing, C_e3D.[87] C_e3D is the first approach to utilize *N*-methylacetamide with histodenz for TOC, a solution selected from 32 tested possible OCAs. The observed excellent sample transparency allowed to perform detailed imaging with subcellular resolution of the lymph node stained with six antibodies and further computational discrimination of cells with the developed method for its post processing (**Figure 36**a,b). C_e3D leads to only minor tissue shrinkage, does not require any specialized equipment, takes less than a week to complete and consists of the following, effortless steps: 1) 1 day fixation in periodate-lysine-paraformaldehyde fixative,[244] 2) 3–4 days of immunostaining, 3) PBS wash, 4) < 1 day clearing, and finally 5) imaging. Notably, applicability of C_e3D as an OCA is not limited to lymph node, as using two-photon excitation microscopy the authors were also successful in reaching as deep as 3 mm into lungs stained with Alexa Fluor 647-conjugated anti-cytokeratin antibody. In addition, C_e3D clearing capacity was tested on several CD11c-YFP expressing organs (brain, thymus, lung, liver, intestines, bone, muscle), which in general showed high average cellular fluorescence intensity of cells at up to 500 µm depth (**Figure 37**). The only evident drawback of C_e3D is the use of *N*-methylacetamide, a compound, which is embryotoxic according to European Chemical Agency, and might prevent other researchers from application of C_e3D for, for example, whole-body clearing, requiring handling great volumes of the clearing solution. Overall, C_e3D is a novel, promising method for simultaneous detection of several epitopes in densely packed environment of lymph nodes.

Abe et al.[237] tested BABB, SeeDB, Clear^{T2}, and CUBIC clearing compatibility with lymph nodes, concluding CUBIC to be superior over BABB (which caused a loss of congenital GFP signal) and SeeDB and Clear^{T2} (both of which led to insufficient transparency). By applying custom-made LSFM to CUBIC-cleared and antibody-stained samples, the researchers were able to image the entire lymph nodes with cellular resolution (Figure 36d) and for the first time delineate proportion between parenchymal, perivascular and intravascular T-cells after i.v. adoptive transfer of fluorescently labeled T-cells. Interestingly, it was also shown that independently from the number of T-cells adoptively transferred (1×10^3, 1×10^4, and 1×10^5), the average percentage of T-cells obtained from a particular popliteal lymph node over total number of transferred cells was relatively constant (≈0.32–0.47%). Such 3D approach was recently applied and allowed to shed light on affinity-dependent orchestration of $CD8^+$ T-cells in spatiotemporal context and propose a role for low-affinity effector T-cells during early microbial containment.[245] CUBIC was also shown to be compatible with clearing of formalin-fixed paraffin-embedded (FFPE) lymph nodes biopsies from patients who underwent surgery for colorectal carcinoma. A detailed analysis revealed that CUBIC neither alters general histological appearance of lymph nodes nor compromises further immunostaining and standard histopathological evaluation of the cleared samples.[246] Importantly, 3D evaluation of halves of lymph node specimens (with the other halves being subjected to standard histopathology at the time of patient's diagnosis) revealed micrometastases unnoticed during histopathological examination, while providing no false positive results. Further, multicenter comparative studies between 3D and standard histopathology needs to be completed to examine the robustness of 3D technique and diagnostic role of possible newly revealed metastases in the patients staging process.

A comparative study on lymph nodes clearing comes from Song et al.,[236] who examined the effect of glycerol solutions (30%, 50%, 75%, 90% in distilled water and 100% glycerol), FocusClear and incubation times of these. Out of glycerol-treated group, 100% glycerol caused severe tissue damage, while 75% concentrated solution applied for 30 min was identified as the best compromise between clearing efficiency (increasing with glycerol concentration) and fluorophore stability (inversely correlated with incubation time) allowing for ≈250 µm and ≈300 µm in depth detection of nuclear H2B-GFP and cytoplasmic actin-DsRed, respectively. FocusClear led to a remarkably better clearing, as revealed by normalized intensity signal, which begins to fall intensively from the depth of ≈300 µm, but is still detectable at ≈500 µm (Figure 36c). The most optimal clearing time was demonstrated to be 12 h, after which the autofluorescence raised significantly with little if any improvement in imaging depth. Having confirmed FocusClear superiority to glycerol solution, the researchers also examined distribution of DsRed and GFP-bearing T and B-cells, respectively, after adoptive transfer, reaching imaging depths of ≈300 µm for both T-cell zone and B-cell follicle and germinal centers. In this particular experiment, immunochemistry was performed systemically, by either intravenous (anti-CD31) or subcutaneous injection (anti-Lyve-1) of antibodies; however, based on FocusClear experiments on, for example, intestines and pancreas, it should be assumed that passive, less expensive post-fixation immunostaining is also

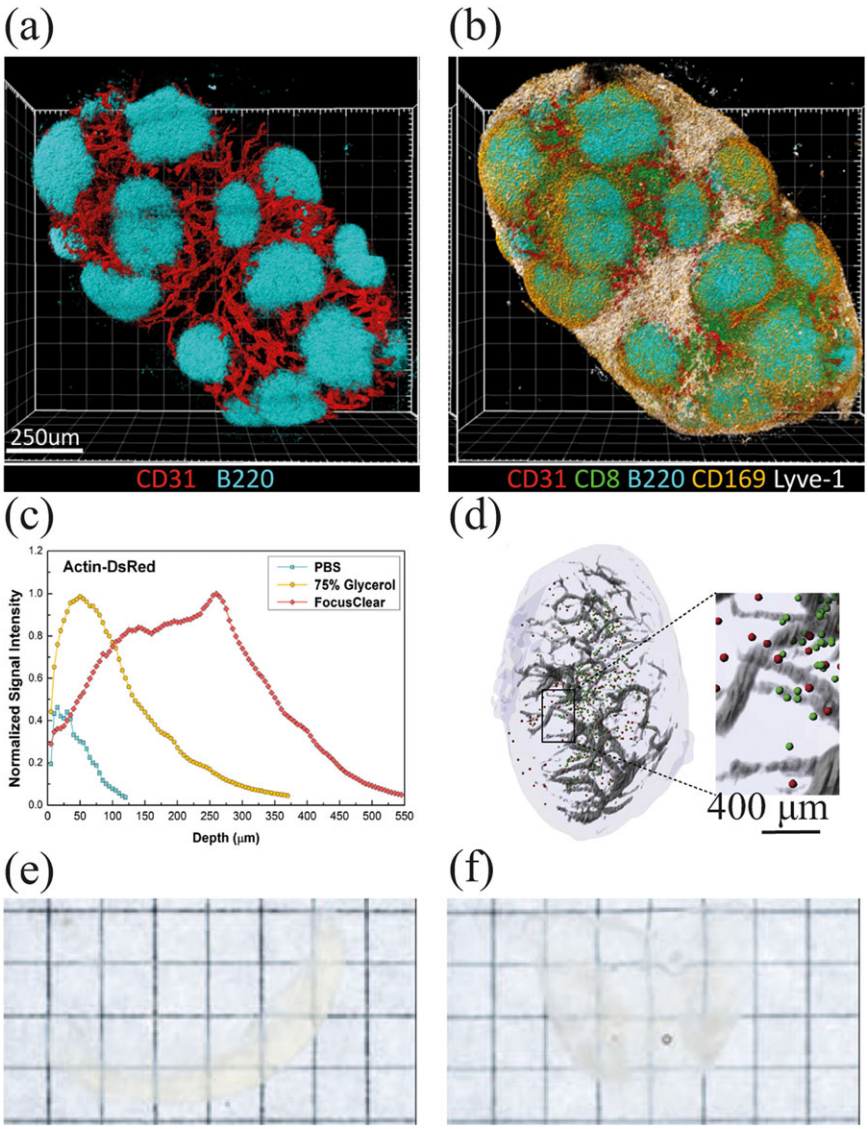

Figure 36. Application of TOC to immune system organs. a) C_e3D is a method specifically developed for clearing of lymph nodes. It is compatible with immunostaining and b) allows for simultaneous visualization of 5–6 epitopes. a,b) Reproduced with permission.[87] Copyright 2017, National Academy of Sciences. c) FocusClear and d) CUBIC (red: CellTracker Orange-labeled bone marrow-derived dendritic cells, green: GFP-expressing OT-I T cells, grey: MECA-79 stained high endothelial venules) are also reasonable for lymph node clearing. c) Reproduced with permission.[236] Copyright 2015, OSA. d) Reproduced with permission.[237] Copyright 2016, Elsevier. e) Optimized CUBIC perfusion leaves rat spleen and f) thymus almost completely transparent within a few days (scale bar: 5 mm). e,f) Reproduced with permission.[139] Copyright 2017, Wiley-VCH.

feasible. Last, Song and co-workers were able to visualize metastases of B16F10-GFP melanoma cells to inguinal lymph nodes at different time points and localize them directly beneath the capsule, proving this approach interesting to consider when studying spatiotemporal dynamics of micrometastases.

Recently, Cabeza-Cabrerizo et al.[243] have used uDISCO with multicolor fate mapping of dendritic cell progenitors to study their proliferation and differentiation in Clec9a^{Confetti} mice. Although the clearing of lymph nodes allowed for detection of various populations of dendritic cells in the T cell areas of the lymph nodes, the superimposition of colors from crowded dendritic cells in these areas precluded analysis of clustering by fluorescent proteins. Perhaps further analyses of that kind might be more informative when methods that cause slight tissue expansion, not severe shrinkage (as uDISCO), are utilized.

Passive clearing of other immune organs, spleen and thymus in particular, is far less advanced and represented by only four studies performed on spleen and one on deciphering the number of thymic epithelial cells at different developmental stages.[247] However, thymus and spleen clearing might be as useful in deciphering spatial tissue context as in any other organ, which was already demonstrated by Inra et al.[248] investigating extramedullary hematopoiesis niche of the spleen. By applying BABB clearing to 300 µm spleen sections and performing one-week-long immunochemistry, the researchers examined the cellular sources and role of two key niche factors, SCF and CXCL12 in myeloablation,

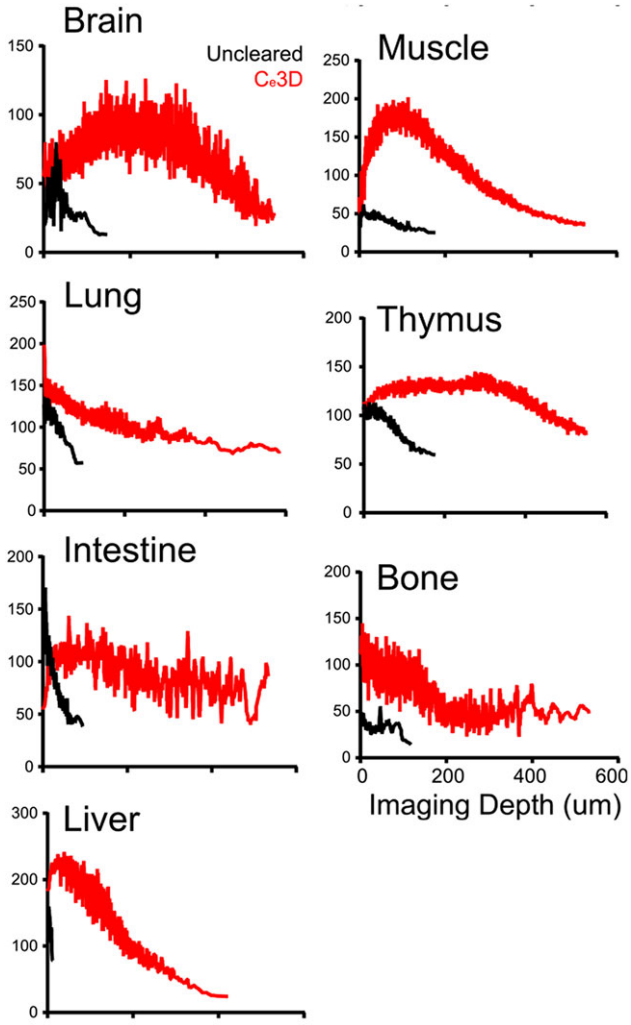

Figure 37. Fluorescence intensity of CD11c-YFP cells across C_e3D-cleared (red) and uncleared (black) peripheral organs. Reproduced with permission.[87] Copyright 2017, National Academy of Sciences.

blood loss and pregnancy, being models of hematopoietic stress mobilization. Similar clearing technique of methanol dehydration and BABB-mediated RI matching was applied by Casanova-Acebes et al.[249] to spleen, along with many other organs, that revealed new migratory capacity of neutrophils to these tissues. The second, proof of concept study, was performed by McErlean et al.,[250] who revealed that combination of spleen TOC with optical computed tomography is valuable for visualization of spleen microstructure and its alterations upon treatment with vascular disrupting agent. Such approach might be further extended and applied for fast spleen structure screening during other toxicological studies. Kieffer et al.[251] successfully studied spread dynamics of HIV infection within gut-associated lymphoid tissue, female reproductive tract and spleen, by applying PACT and CUBIC clearing, respectively. Recently, we presented that our modified perfusion-based CUBIC is an effective approach for rapid clearing of both spleen and thymus of rodents (Figure 36e,f).

Oren et al.[252] presented yet another approach for whole organ blood and lymphatic vessels imaging (WOBLI). WOBLI relies on tissue fixation/permeabilization, immunofluorescence labeling of lymphatic vasculature with anti-LYVE1 antibody (1 week for primary and 1 week for secondary antibody staining), which are followed by CLARITY clearing and RI matching in Sca*l*eA2. In the original publication, the authors examined WOBLI on uterus, ovary, lung, liver, and brain from mouse expressing tdTomato under the vascular endothelial cadherin promoter (the expression of which is restricted to endothelial cells of both developing and mature blood vessels), thus were able to limit immunolabeling to one epitope. With the developed approach, it was feasible to label and image organ's vasculature up to 2400 µm deep into the tissue and elucidate its characteristics, such as vessel's length, mean diameter or the number of branching points. Using 200 µm RapiClear-cleared sections of lymph nodes isolated from various multicolored fate-mapping mouse models, a group led by *Bajénoff*[253] *revealed that remodeling of the inflamed lymph node vasculature is dependent on clonal proliferation of high endothelial venule cells.*

Certainly, development of novel segmentation algorithms for quantification of imaged microvascular networks will be essential to organize such large datasets.[254–257] One of such promising tools is VIPAR (volume information-based histopathological analysis by 3D reconstruction and data extraction procedure), the efficacy of which was recently presented by Kiefer's group.[258] Using VIPAR, the researchers could decipher various features of complex lymphatic vasculature within human skin biopsies cleared with Murray's Clear.

3.10. Female Reproductive System

Female reproductive system is composed of organs undergoing rapid and almost lifelong morphological changes. Due to the complex, fragile 3D architecture and dynamic nature, it cannot be studied in detail using 2D histology. Up to date, every chemically distinct TOC method was applied to study organs of female reproductive system and everyone made clear contribution to better understanding of either female reproductive general physiology or pregnancy.[259,260] Study by Feng et al.[261] allowed for the first time to count the total number of five various follicles types (primordial, primary, secondary, antral and preovulatory) at five different time points throughout mice life (3, 10, 21, 60, and 360 days) and assess their spatial organization and clustering characteristics (**Figure 38**a).[261,262] Using PECAM-1 (CD31) staining, the group also examined ovarian vascular network surrounding follicles and corpora lutea throughout mouse lifetime and upon treatment with human/equine chorionic gonadotropin or axitinib (type 1–3 VEGF, c-Kit, and PDGF receptor antagonist), which increased the vasculature size and number of blood vessel branches and significantly decreased the number of ovulated oocytes, respectively. In addition, the results showed that follicles distribution is not random, but highly dependent and shaped along vascular network, having three to four main branches under general conditions. As in the case of other CLARITY-adapted protocols for peripheral organs, the major drawback remains time of tissue processing, which was extremely expanded, taking five to nine weeks.

Very recently, Kagami et al.[263] have shown that CUBIC might also be suitable for adult mouse ovary imaging. Using

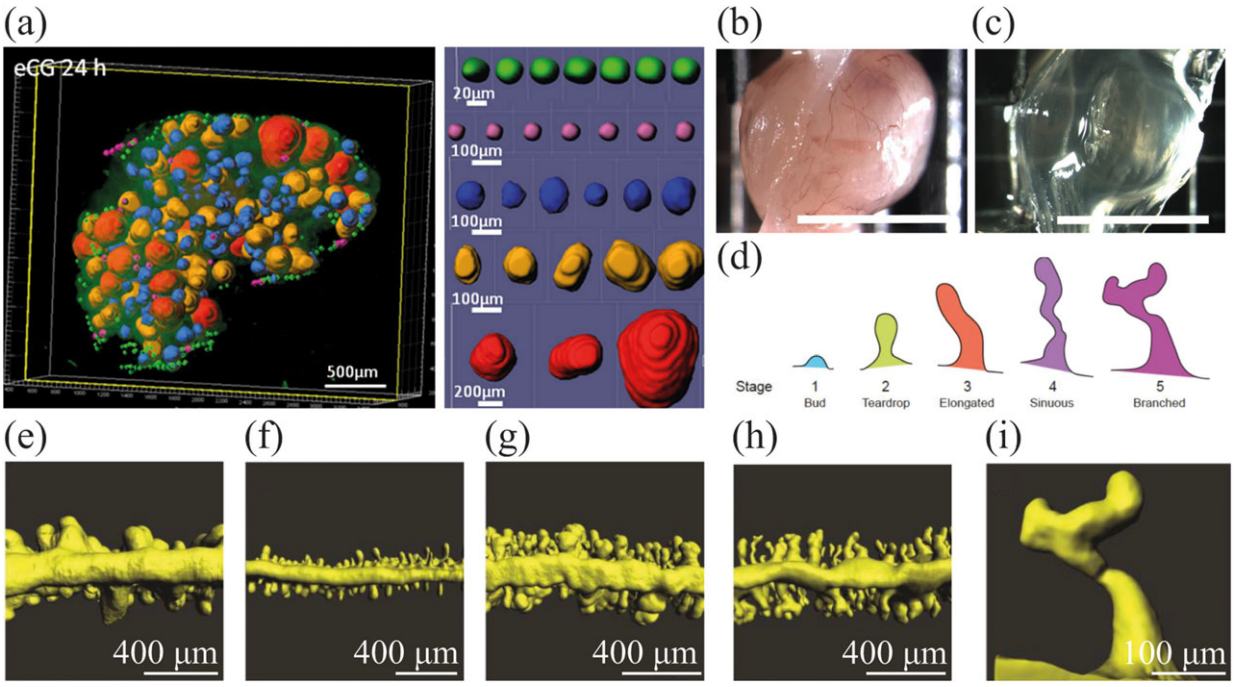

Figure 38. TOC applied to a female reproductive system. a) CLARITY allows for the visualization of the entire mouse ovary and differentiation of individual ovaries (ovary of an immature eCG-treated animal, follicles: green: primordial, purple: primary, blue: secondary, yellow: antral, red: preovulatory). Reproduced under the terms of the CC-BY Creative Commons Attribution 4.0 International License (http://creativecommons.org/licenses/by/4.0/).[261] Copyright 2017, The Authors. Published by Springer Nature. b,c) Pregnant mice uterus at E9.5 before (b) and after (c) CUBIC clearing (scale bar: 4 mm). Notably, although almost complete transparency of uterus is achieved, CUBIC does not alter the size of the tissue. Reproduced under the terms of the CC-BY Creative Commons Attribution 4.0 International License (http://creativecommons.org/licenses/by/4.0/).[264] Copyright 2017, The Authors. Published by Springer Nature. d–i) Novel staging system for individual uterine glands based on TROMA-1 stained immunofluorescent images of the uterine epithelium cleared with Sca*l*eA2 (d), bud (e), teardrop (f), elongated (g), sinuous (h), branched (i). d–i) Reproduced with permission.[265] Copyright 2018, Wiley-VCH.

CAG-EGFP transgenic mice the researchers confirmed that CUBIC treatment of 6–12 months old mice ovary does not quench EGFP significantly, is compatible with PI staining and the transparency of the entire organ can be achieved within 10 days of clearing. Interestingly, it was shown that such clearing does not cause tissue deformation, neither shrinkage nor slight expansion, with the latter being repeatedly reported upon CUBIC treatment in other organs. In another study, using similar conditions (10 days long CUBIC clearing, EGFP-mice and PI staining) this group has demonstrated that intrauterine imaging of the entire developing conceptus through the transparent uterine is also feasible and does not alter tissue size (Figure 38b,c).[264] This approach might be broadly employed, for example, to image trophoblast invading the fetomaternal junction and alterations of these during the entire pregnancy.

Sca*l*e, was already applied in a similar way to provide detailed images of adenogenesis within uterine epithelium in prepubertal mouse.[265] Volumetric analysis of the 3D uterine epithelial glands at different time points allowed the researchers to classify them into five morphologically distinct types (bud, teardrop, elongated, sinuous, and branched) and thus propose their novel 3D staging system in accordance to the results (Figure 38d–i). Clearing of the uterus was also of interest for BABB-utilizing group led by Laird,[266] who focused on investigation of uterine architecture alterations caused by fertilization and implantation. In aggregate, by performing whole-mount immunostaining and subsequent BABB clearing, the researchers were able to image progressive formation of uterine crypts generated by folding of epithelium and its orientation polarizing toward mesometrial-antimesometrial axis, along with defective crypt formation in *Wnt5a*^{cKO} mice. Application of CUBIC and Sca*l*eS was reported effective to study spatial distribution of $\gamma\delta$ T lymphocytes in murine vaginal wall.[267]

To summarize, it is already evident that TOC applied to female reproductive system is very helpful in revealing multiplex spatiotemporal changes occurring throughout life and gestation; however, novel advanced approaches are undoubtedly yet to be used, as all of the mentioned studies were reported only very recently.

3.11. Male Reproductive System

So far, the only, but comprehensive side-by-side comparison of five TOC methods (SeeDB, 3DISCO, CUBIC, PACT, RIMS) for testes clearing was performed on zebrafish transgenic line that expresses GFP in Sertoli cells.[268] Although the highest transparency was achieved with 3DISCO, this method was otherwise not recommended as GFP fluorescence decayed immediately after 15 min of DBE incubation, testes transformed into especially hard pieces prone to breaking and, as highlighted but expected, 3DISCO required handling of toxic reagents and caused

severe tissue shrinkage. Both RIMS and SeeDB treatments led to unsatisfactory clearing and thus limited imaging depth. However, treatment with either CUBIC or PACT resulted in similarly good results with respect to the all tested parameters: GFP fluorescence preservation, minimal tissue deformation, and feasibility of whole-mount two-photon imaging. The only advantage of CUBIC over PACT was significantly shorter incubation time of 5 days versus 13 days, respectively. The aforementioned limitations of solvent-based clearing, mainly rapid XFP signal decay, did not prevent its successful adoption for imaging of human prostate biopsy specimens[116] and bladder tumors.[269,270] Royen et al.[271] have shown that Murray's Clear combined with immunochemistry can be performed on both freshly dissected and FFPE prostate samples and enable as deep as 800 µm imaging. Such 3D approach allowed to shed light on architectural differences between Gleason grade (grading system specific for prostate cancer) 3 and 4 glands and thus might be soon very beneficial to increase relatively poor inter-observer concordance in such histologically challenging to verdict cases. Recently, the same group has extended this solvent-based approach. Using iDISCO protocols they characterized 3D architecture of both benign and pre-cancerous prostate lesions[272] and described two distinct growth patterns of prostate cancer in patients.[273] Notably, no group has taken up the matter of TOC of penis which, assumingly, would be valuable for deciphering of blood vessels and innervations patterns, with possible application to improve understanding of, for example, severe cases of erectile dysfunction.

3.12. Adipose Tissue

Adipose tissue is yet another composite tissue made of adipocytes, stromal cells, containing neurons, blood vessels, and immune cells. Traditionally it is divided into subcutaneous and visceral (surrounding internal organs) fat in respect to anatomy and into energy storing white and heat-generating brown adipose tissue regarding its physiology. In addition, an inducible brown fat, named beige fat, was discovered to persist within subcutaneous portion of white fat. Its activation was already associated with anti-obesity and anti-diabetes reactions, which made it an interesting and intensively studied tissue. Characterization of beige fat in terms of localization and innervation was first possible upon application of solvent-based TOC already performed by few groups.[274–277]

The most detailed 3D view on beige fat under general and cold-exposure conditions has recently been presented by Chi et al.[276] who, by building upon iDISCO, described a novel TOC method focused on adipose tissue, termed Adipo-Clear. Although consisting of numerous steps, this approach is straightforward, does not require any specialized instruments, and can be completed within 12 days for the entire posterior subcutaneous fat depot (2 days for delipidation and clearing followed by 10 days for staining with primary and secondary antibodies). Accompanied by LSFM (Ultramicroscope II, LaVision Biotec), it allowed to reveal striking differences in distribution of uncoupling protein 1 (a hallmark protein of brown fat) expressing cells within posterior subcutaneous fat depot, which was further correlated with asymmetric prevalence of sympathetic innervation (**Figure 39**a,b). A relevant advantage, which further underscores Adipo-Clear utilization for fat imaging is postdelipidation autofluorescent signal, which reflects perilipin staining and therefore might be used to detect tissue architecture and precisely delineate cells contours. This is especially important, as Adipo-Clear requires 8–10 days for immunostaining. It should be also noted that tissue treatment with methanol, a key Adipo-Clear reagent, might impair the structure of particular epitopes, as it was already shown for CD31 and CD105, common vascular epitopes. This encouraged Cao et al.[278] to search for alternatives and resulted in development of modified iDISCO technique for adipose tissue clearing, in which methanol-based permeabilization is replaced by detergent-based steps. In addition, the authors reported

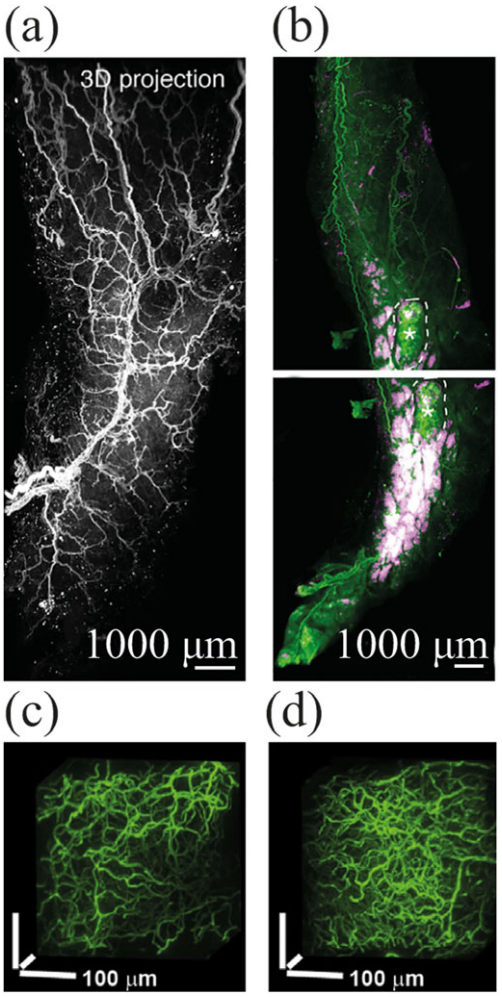

Figure 39. Organic solvents are advantageous during clearing of adipose tissue. a) Adipo-Clear is an iDISCO variation, specifically developed for efficient clearing and immunolabeling of adipose tissue. It allows, for example, for the visualization of sympathetic innervation of psWAT [a) posterior subcutaneous white adipose tissue, grey: tyrosine hydroxylase stain] or b) changes in expression of uncoupling protein 1 (purple: UCP1 stain, green: autofluorescence) after exposure of the animal to a cold environment. Tissue treatment with organic solvents might compromise the structure of several vascular epitopes. Reproduced with permission.[276] Copyright 2018, Elsevier. c) Isolectin staining is compatible with such clearing, thereby it serves as a potent alternative when, for example, vascular remodeling in adipose tissue is being studied; d) cold-induced vascular plasticity. Reproduced with permission.[278] Copyright 2018, Elsevier.

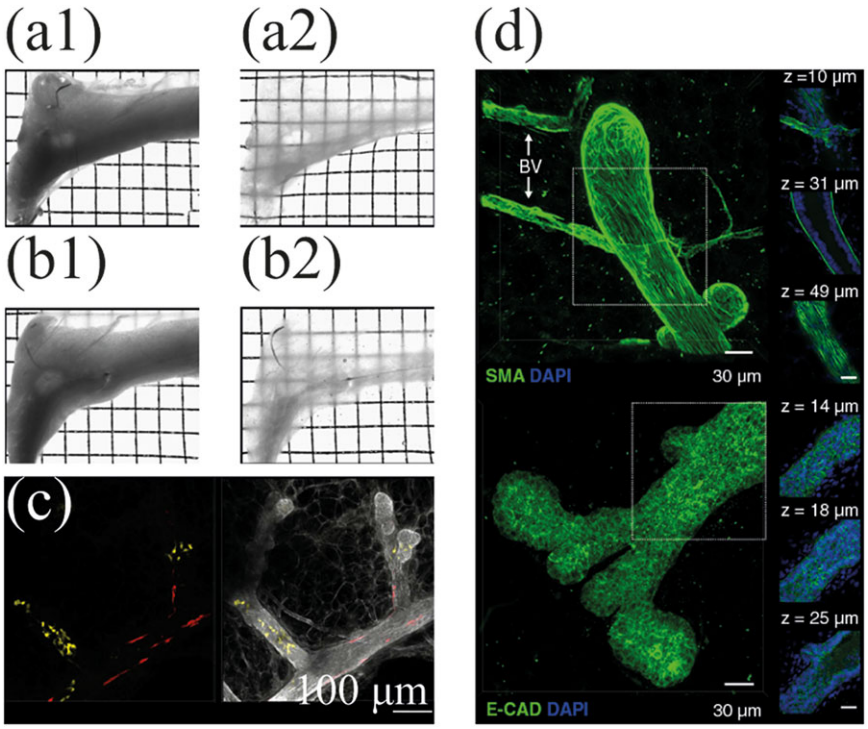

Figure 40. TOC of a mammary gland. a,b) Murine mammary glands (a1,b1) can be efficiently cleared with either CUBIC (a2) or SeeDB (b2) (grid width: 2 mm). c) Labelling pattern of the contribution of single alveolar cells to the development of alveoli observed in R26-Confetti;R26-CreERT2 pubertal mice (YFP: luminal cells, RFP: basal cells). Reproduced under the terms of the CC-BY Creative Commons Attribution 4.0 International License (http://creativecommons.org/licenses/by/4.0/).[280] Copyright 2016, The Authors. Published by Springer Nature. d) CUBIC clearing can be utilized to obtain a detailed 3D view of luminal cell markers (SMA, smooth muscle actin, E-CAD, E-cadherin) and thus compare structure of virgin (top) and lactating mammary gland (bottom). Reproduced under the terms of the CC-BY Creative Commons Attribution 4.0 International License (http://creativecommons.org/licenses/by/4.0/).[279] Copyright 2016, The Authors. Published by BioMed Central.

compatibility of such approach with intravenous injection of Alexa dye-conjugated Isolectin to effectively label endothelial cells within less than 24 h (Figure 39c). Co-staining with CD31 and imaging of *Tek-Cre; Rosa26-LSL-tdTomato* mice (in which vasculature is labeled with tdTomato) revealed that >99.9% of CD31 cells were also Isolectin positive, while only 89.4% of Isolectin positive cells were also tdTomato positive. This means that Isolectin is a highly specific and sensitive marker of endothelial cells and, interestingly, exposes imperfection of Cre-activity in a fraction of endothelial cells. Finally, the aforementioned approach allowed the authors to describe events of vascular plasticity in white adipose tissue of both wild-type and obese mice strains in a response to a cold challenge (Figure 39d), and proved this plasticity to be catecholamine-mediated.

3.13. Breast

Although adipocytes are the main stromal cells of the breast, utterly different approaches were so far proposed for its clearing, abandoning solvent-based methods for water-based ones, CUBIC and SeeDB in particular (**Figure 40**a,b). Using these protocols with minor modifications, Davis and Lloyd-Lewis with colleagues[279] were able to effectively clear and image mammary glands of both virgin, pubertal, and adult mice for up to 400 µm deep with single cell resolution (Figure 40c). Successful whole-mount immunostaining and XFP stabilization allowed them to trace single-cell lineage of mammary stem cells/progenitors and thus, reveal many unanticipated phenomena such as random distribution of progeny of a single stem cell to multiple ducts or the presence of heterogenous subpopulations of alveolar cells with their contribution to alveoli development[280] (Figure 40d), which could not be exposed otherwise. Recently, Seong et al.[281] utilized this approach to delineate process of side branching in developing mammary gland and Hume et al.[282] proved CUBIC to be an effective clearing agent for human breast tumor biopsy and further applied this method in conjunction with immunostaining to monitor structural integrity of engineered 3D in vitro adipose tissue model recapitulating breast tumor microenvironment.

As organic solvents are known to yield the highest level of transparency in heme-free organs, it would be of interest to see Adipo-Clear applied to breast tissue. However, simultaneous visualization of multiple different cell types requires many reporting proteins,[283] as present in, for example, confetti mice—mouse strain in which fluorophores of four distinct excitation spectra/"colors" can be induced selectively upon Cre activation (dependent on administration of particular substance, e.g., tamoxifen), and in which daughter cells are producing the same fluorophore, which allows to trace the lineage of single cell. Therefore, additional attempts should be made to increase XFP stability of Adipo-Clear solutions and thus overcome this limiting factor.

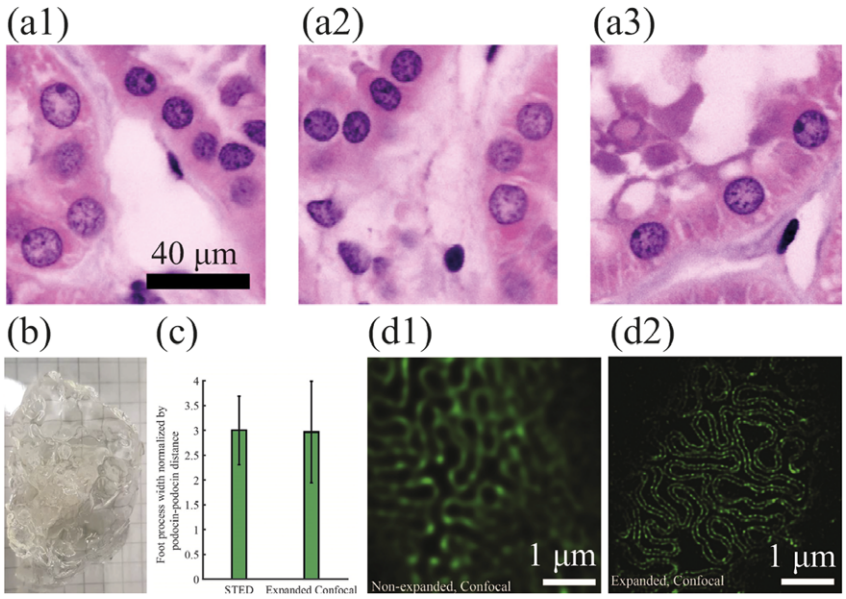

Figure 41. Application of TOC for kidney research. a) Murray's Cleared and Eosin-Y- and DAPI-stained kidney (and pseudo-colored) fully resembles classical H&E staining. Fine details can be appreciated at the full depth of the imaged tissue, that is, at 200 μm (a1), 600 μm (a2), and 1000 μm (a3). Reproduced with permission.[284] Copyright 2016, Optical Society of America. b) Expansion microscopy for a rat kidney enlarges tissue by a factor of 5 (grid width: 1 cm) while c) preserving the proportions between its intrinsic structures, thereby greatly increasing image resolution. d1) before expansion, d2) after expansion. b–d) Reproduced with permission.[79] Copyright 2018, Elsevier.

3.14. Kidney

Until now, only a few studies have focused on development and application of TOC for the kidney.[57,79,284–286] These are, however, advanced and bring novel ideas relevant to both basic science and clinical practice. Olson et al.[284] discovered that BABB clearing coupled with adjusted concentrations of 4′,6-diamidino-2-phenylindole (DAPI) to reveal cell nuclei and Eosin Y to stain cytoplasmic proteins during dehydration step results in kidney images that fully resemble those obtained by standard H&E staining. It not only replicated classical H&E staining in shorter and less burdensome way, but more importantly provided better contrast (thickness of optical slices were set to 2 μm vs 3–5 μm of standard H&E slide) within the entire sample tested for up to 1000 μm in depth (**Figure 41**a). Although the authors describe protocol as consisting of two steps: 1) ≈4 h long methanol dehydration, followed by 2) ≈1 h immersion in BABB, it lacks relevant information about methanol concentration used in the study. Such details are paramount as this approach bears potential for relatively rapid application in everyday medical practice, while reducing costs of tissue examination. However, this would require additional study to test compatibility of such clearing with rapid LSFM imaging, as imaging of one biopsy sample performed by the authors on home-built multiphoton microscope based on a Ti-Sapphire laser (with HCX Apo L 20, 0.95 NA, Leica objective) took 30 h. Although promising, this technique requires further examination, especially as it contradicts reports by Nehrhoff[140] and Hama,[60] which revealed rather poor structure preservation after BABB clearing of heart and brain, respectively. Such discrepancy might be due to the tissue differences themselves or rather the fact that Olson with colleagues performed adopted H&E staining during the clearing, while Nehrhoff and Hama completed H&E staining and tissue slicing after the clearing and therefore exposed samples to additional stress.

The only protocol elaborated specifically for LSFM imaging of transparent murine kidney is ethanol-ECi described by Klingberg et al.[57] Principles of this dehydrating approach are identical as other solvent-based methods; however, astute selection of used chemicals allowed to overcome critical limitations of previously known protocols—toxicity and stability of fluorescent reporters. In accordance, the most prominent feature of ethanol-ECi is utilization of ethyl cinnamate (food flavor) as RI matching and imaging solution instead of toxic, potential carcinogens, such as BABB and DBE. Moreover, to increase XFP signal preservation while prohibiting possible formation of explosive peroxides, THF was replaced by alkaline (pH = 9.0) ethanol. This combination is well suited for XFP stabilization for two weeks and allowed the researchers to achieve a complete transparency of murine kidney within one day and to count the total number of glomeruli in health and during nephrotoxic nephritis in a proof of concept study. Additionally, ethanol-ECi can be successfully applied to clear other organs, such as heart, bones, and calvaria (upper bones of skull). Application of ethanol-ECi to bone clearing of both mouse and human, commissioned discovery of new type of blood vessels, called trans-cortical vessels, that exhibit potential role in many important processes, such as bone turnover or the recruitment of immune cells from bone marrow.[287] Recently, Masselink et al.[102] tuned the ethanol-ECi formula by replacing ethanol with alkaline (pH 9.0) 1-propanol, that resulted in improved stability of XFPs and allowed them to successfully clear and image a variety of tissues, including cerebral organoids, adult, and larvae of axolotl, *Xenopus* and *D. melanogaster*. They called the new formula 2ECi, 2nd generation ethyl cinnamate–mediated clearing. Application of ECi has

already allowed the researchers to visualize morphological and molecular remodeling of distal convoluted tubules upon low-potassium diet[288] and to reveal new 3D quantitative endpoints in the model of crescentic nephritis.[289] ECi-based clearing was also applied to present utility of new cationic near infrared fluorescent agent, MHI148-PEI, for specific staining of vascular structures in variety of organs, for example, skin, liver and lung.[290] Altogether, ECi methods are rapid, inexpensive, not toxic and not hazardous for imaging equipment, it yields full transparency of many organs, preserves XFP signal for reasonable time and as such should be perceived as a very promising method to be applied in further studies. The only drawbacks that one could think of is strong acrid smell of ethyl cinnamate and the extent to which residual heme interferes with organs imaging. This however, should not override already disclosed advantages.

The opposite direction of kidney clearing was presented by Unnersjö-Jess et al.[285] who, instead of shrinking the sample to image its entirety, utilized clearing with modified CLARITY and MAP to expand tissue volume by a factor of ≈5 (Figure 41b), hence obtaining impressive level of the effective resolution, around ≈20 nm, during glomerular filtration barrier imaging (Figure 41d). Importantly, such heavy organ expansion neither changed relative distance between cells in microscale, as revealed by measured mean podocyte foot process width and podocyte-to-podocyte distance nor limited its immunostaining properties (Figure 41c).[79]

3.15. Eyeball and Optic Nerve

The first attempts to optical clearing of sclera were made by Tanaka et al.,[291] who developed specific protocol consisting of critical point drying of the indicated dissected tissue followed by chemical cross-linking in the originally proposed mix of 1-ethyl-3-(3-dimethylaminopropyl) carbodimide and *N*-hydroxy succimide. Optimized composition of the presented cross-linking agent allowed them to obtain rigid stabilization of adjacent collagen fibers in the sclera. This, in turn, led to prominent and permanent tissue transparency (with transmittance at 550 nm oscillating around 50%), even when put back to wet, "physiological" conditions. Such result is unique for TOC, as there exist no clearing agent, the effect of which would be irreversible once moved from RI-matching solution. Shortly, the same group obtained the formula effective also for permanent skin clearing, which was then successfully engrafted to rabbit corneal stroma in allogenic transplant model.[292] It is worth mentioning that such chemical cross-linking was shown to be biocompatible, and as such might be useful in future development of optically cleared "windows" (e.g., in dermis or skull) to increase the depth of in vivo observation.

The study by Singh et al.[293] focused on clearing and imaging of retina, rather than the whole eye. According to this recent report, CLARITY allowed to bypass superficial primary vascular plexus and for the first time enabled exploring the complexity of vascular plexuses in the entire retina. A proof of concept study was performed using rats exposed to the prolonged hyperoxia, which served as a model of angiogenesis inhibition. The results readily demonstrated that the provided protocol accompanied by LSFM, confocal imaging and Sholl analysis is capable of precise tracing of vascular network and its further quantification in the entire retina. Clearing of the whole eyeball, not just dissected elements, is challenging due to the presence of melanin in the retina, which limits utilization not only of solvent-based protocols (unable to clear pigments), but also CUBIC, otherwise possessing decolorizing capacity. Consistent with this is a brief report of Hohberger et al.,[294] who performed SeeDB protocol on halves of human and chicken eyes. Evidently, SeeDB treatment was capable of clearing both sclera and adjacent optical nerve, while leaving choroid and iris only partially transparent. A problem of light-obstructing retinal pigmented epithelium was finally overcome by Henning et al.,[295] who deftly combined: 1) bleaching step established by Kim and Assawachananont,[296] 2) iDISCO+ immunolabeling, and 3) ECi clearing. The developed protocol, named EyeCi, allows for the unobstructed visualization of the intact eyeball vasculature.

Although distant from eyeball clearing, it is plausible to adduce here the fact that TOC was already used to study murine models of optic nerve regeneration and the effects of possible drugs enhancing this process with single cell resolution.[297–299] Such 3D based approach linked with brain TOC allowed few groups to identify morphological changes in regenerating axons that follow-up injury, its high regenerating capabilities as well as circuitous, U-shaped axon growth, which significantly limits reconnection with distant brain targets, such as superior colliculus and lateral geniculate nucleus.[300]

3.16. Lung

Taking spongy structure of lungs and lack of evident pigments into account, straightforward clearing of this organ should be anticipated. Apparently, all chemically distinct approaches, namely BABB,[301,302] CUBIC,[303] CLARITY/PACT,[217,304] accompanied with whole-mount immunostaining and imaging were already applied to murine and human lung tissue (**Figure 42**). Pioneering lung BABB clearing was reported by Scott et al.,[301] who presented the first detailed view on the relationship between nerves, vessels and airways architecture, detected novel patterns of pleural innervations and connectivity patterns of pleural nerves. Solvent-based clearing proved also beneficial for the detection and analysis of lung tumor metastases.[305]

A comprehensive analysis of lung innervations was studied by Watanabe et al.,[303] who recently exercised CUBIC protocol to compare parasympathetic nervous system of mouse and chicken. Interestingly, the compatibility of highlighter ink staining with CUBIC clearing was shown, which allowed fine visualization of bronchi as well as peripheral bronchioles. Moreover, CUBIC cocktails are also applicable to study FFPE human biopsies and prominently do not alter neither their histological appearance nor immunostaining capability.[246] Thereby, similarly to lymph node examination, such TOC might be easily adapted to extend the gold standard of histopathological evaluation of patient's samples as a complementary, not alternative, approach. TOC of lungs was also essential for studies analyzing tumor-immune microenvironment, for example, 3D pattern of tumor-associated macrophages distribution (Figure 42c).[138,306] A study by Cuccarese et al.[138] was also the first to present that lengthy process of whole-mount lung immunostaining can be

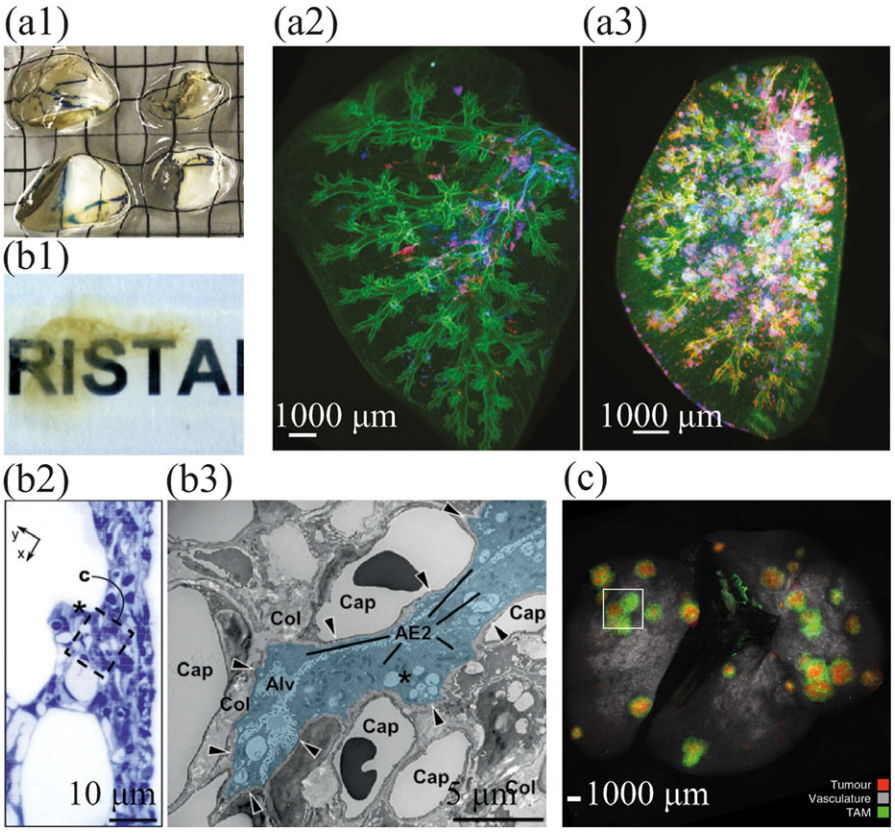

Figure 42. Application of TOC to a lung. a1) 3DISCO was reported to be better than CLARITY for lung clearing (grid width: 2 mm) and further imaging of bronchus-associated lymphoid tissue, BALT; a2) BALT from a control animal, a3) BALT from an animal infected with modified vaccinia virus ankara, red: CD3, blue: B220. Reproduced with permission.[308] Copyright 2018, Springer Nature. b1) CRISTAL, a unique method in which the organ is dehydrated and encapsulated in transparent resin, prohibiting tissue rotation, thereby allowing for correlative studies between b2) high-resolution histological imaging (blue: Toluidine blue) and b3) transmission electron microscopy (Col, collagen fibrils; Alv, alveolus; AE2, alveolar epithelial type II cell; Cap, capillary). Reproduced under the terms of the CC-BY Creative Commons Attribution 4.0 International License (http://creativecommons.org/licenses/by/4.0/).[312] Copyright 2016, The Authors. Published by Springer Nature. c) CUBIC might also be used as a lung clearing agent as confirmed by successful visualization of tumor cells (red) and tumor-associated macrophages (green). Reproduced under the terms of the CC-BY Creative Commons Attribution 4.0 International License (http://creativecommons.org/licenses/by/4.0/).[138] Copyright 2017, The Authors. Published by Springer Nature.

profitably replaced by intravenous injection of fluorophore-tagged nanoparticles.

Adoption of CLARITY allowed to observe the dynamics of infection of tdTomato-expressing *M. tuberculosis*[304] and to highlight nestin, as a potential prognostic marker of pulmonary hypertension.[307] CLARITY might, however, be challenging to apply, as reported by Mzinza et al.,[308] who failed to reach sufficient imaging depth to analyze bronchus-associated lymphoid tissue (BALT), while achieving suitable imaging conditions upon 3DISCO treatment (Figure 42a). Further application of 3DISCO (and iDISCO for immunolabeling) allowed the authors to study alterations in cellular composition of the entire induced BALT in a variety of experimental models (Figure 42a). 3DISCO was also shown to be valuable, when combined with label-free multiphoton microscopy and second harmonic generation microscopy for the 3D assessment of pulmonary fibrosis[309] and to study differences in pulmonary distribution profile of fluorescence labeled nanoparticles depending on the route of their administration (intratracheal instillation vs inhalation).[310]

Application of a much less frequently used method, Clear^{T2}, demonstrated the utility of TOC for imaging of aerosolized drugs distribution throughout lungs.[311] As a proof of concept, Texas-Red dextran was aerosolized into the murine lungs. Imaging revealed that Clear^{T2} does not alter histological appearance of tissue as confirmed by lectin intravenous administration and is suitable for detection of drug distribution. Complete preservation of tissue microstructure, although desirable, is achieved because Clear^{T2} lacks delipidation capability, which in turn results in poor imaging depth, oscillating around 100 µm, as shown in the mentioned study.

Lung was also the organ of interest for Kellner and colleagues,[312] who described utterly distinct transformation TOC approach, termed CRISTAL (curing resin-infiltrated sample for transparent analysis with light). The idea behind CRISTAL is the encapsulation of organ in colorless resin, RI of which matches RI of the specimen, which results in preparation of rigid, transparent sample that first can be imaged microscopically with cellular resolution and then directly subjected to correlative nano-scale studies with TEM (Figure 42b). CRISTAL

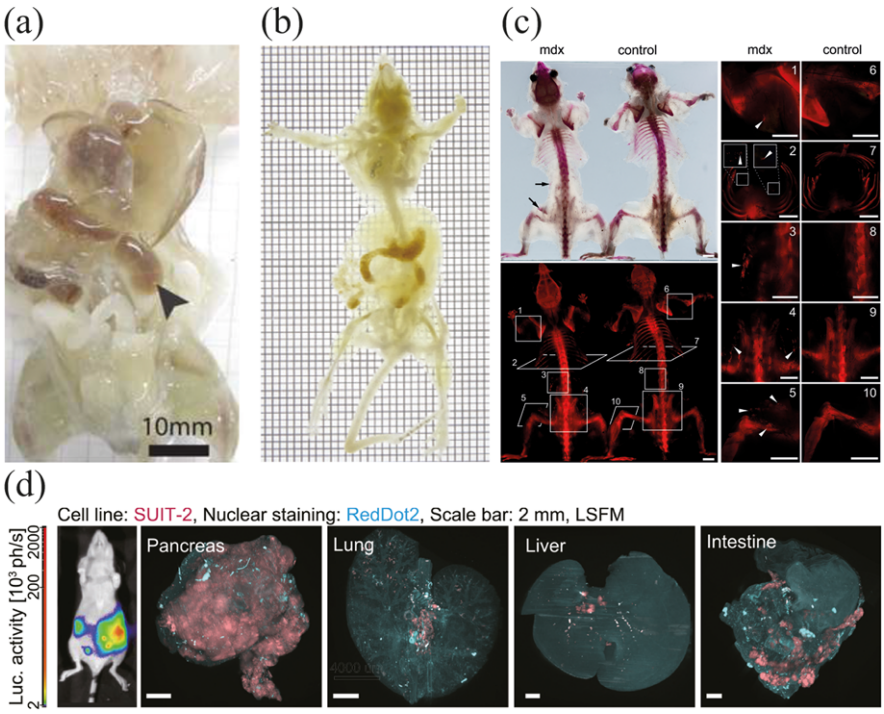

Figure 43. Application of whole-body clearing. a) Both PARS and b) CUBIC whole-body clearing approaches efficiently decolorize the entire animal (apart from the skin, which is removed prior the clearing procedure). c) CUBIC can be utilized to reveal treatment efficacy or describe the progression of Duchenne muscular dystrophy by monitoring discrete sites of calcium deposits in whole bodies of dystrophic mice strains (e.g., mdx mouse, scale bar: 1 cm), which accumulate at muscle injury sites but are not present in control animals. d) CUBIC whole-body clearing also allows for rapid, simultaneous visualization of cancer metastases within various organs. a) Reproduced with permission.[38] Copyright 2014, Elsevier. b,d) Reproduced with permission.[35] Copyright 2017, Elsevier. c) Reproduced under the terms of the CC-BY Creative Commons Attribution 4.0 International License (http://creativecommons.org/licenses/by/4.0/).[317] Copyright 2018, The Authors. Published by Biomed Central.

workflow consists of the following steps: 1) tissue fixation, 2) dehydration in increasing gradient of ethanol, and 3) gradient of xylene, 4) embedding in resin, and finally 5) polymerization/curing of the resin by exposure to UV light. Notably, after the polymerization step, no further action (apart from slicing) is done to the tissue, which creates unique opportunity to perform relevant correlative studies between light and transmission electron microscopy. Moreover, tissue embedding in rigid resin does not allow for free rotation of the specimen, thus it guarantees control over its location and selection of the same areas for studies with distinct techniques. However, both sample dehydration and prolonged (≈24 h) exposure to UV light, greatly limits feasibility of XFPs visualization. Other potential drawbacks of such methodology are inability to perform additional rounds of any staining after the resin is cured, the need for calculation and adjustment of resin's RI before every experiment (as it might be influenced by the batch and storage time of the resin), and finally long protocol time, as the entire CRISTAL takes weeks to complete. As the method relies on successful infiltration of organs by the resin, it could be suspected that CRISTAL utilization will be narrowed to porous tissues, for example, the reported lung clearing and imaging. However, by increasing the incubation times in resin for bone and brain up to two and three weeks, respectively, the authors presented that CRISTAL is an interesting alternative capable of clearing of various organs.

4. Whole-Organ and Whole-Body Clearing Techniques

So far, every chemically distinct approach was applied to whole-organ and whole-body clearing with success. The first study to try whole-body clearing was conducted by Yang et al.,[38] who perfused adapted CLARITY solutions through murine cardiovascular system, thereby developing PARS technique (**Figure 43**a). PARS not only achieves clearing of all organs simultaneously, but also provides the opportunity to perfuse antibodies and other small molecule chemical dyes through animal vasculature, which greatly accelerates the process and depths of staining, which are currently main drawbacks of passive CLARITY protocols. The additional advantage of PARS is that the intact musculoskeletal system opposes tissue swelling and deformation, which are therefore less pronounced when compared to passively cleared samples. Although robust in terms of staining, PARS still requires long incubation times (≈20 days) to clear whole body. Further optimization of hydrogel composition led to development of the improved version of this protocol, named PARS-mPACT.[313] PARS-mPACT proved to reduce the clearing times significantly (by ≈1 week) and worked well with both adult murine and rat organs. It also replaced the original RIMS solution with a tuned formula of Nycodenz-based nRIMS.

Thus far, few other optimizations of CLARITY for whole-organ clearing were reported,[314,315] with the ultimate acceleration of

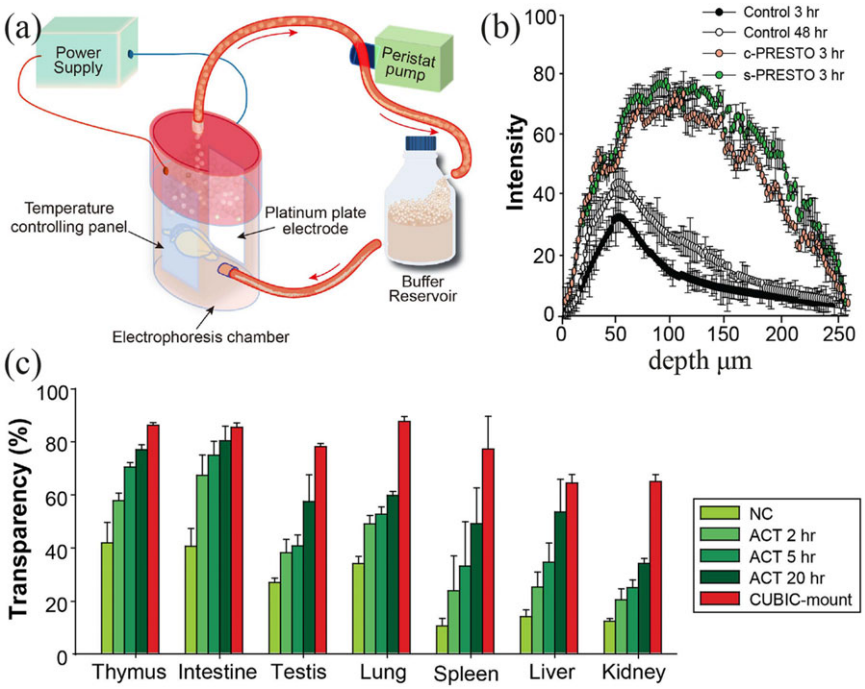

Figure 44. Active clarity technique (ACT). a) Electrophoretic tissue clearing system for ACT. b) Both centrifugal and syringe PRESTO are effective approaches for increasing immunostaining depth in ACT-cleared tissues. c) ACT achieves substantial transparency of peripheral organs. Reproduced under the terms of the CC-BY Creative Commons Attribution 4.0 International License (http://creativecommons.org/licenses/by/4.0/).[316] Copyright 2016, The Authors. Published by Springer Nature.

CLARITY-based whole-organ and whole-body clearing presented by Lee et al.,[316] who developed ACT (*a*ctive *c*larity *t*echnique) and PRESTO (*p*ressure *r*elated *e*fficient and *s*table *t*ransfer of macromolecules into *o*rgans) for rapid tissue clearing and staining, respectively. ACT is a stable variation of ETC, in which clearing is boosted by platinum plate-derived dense regular current and organs are prevented from burning by implementation of active cooling system (**Figure 44**a). Although ACT clears the majority of murine organs within 2–20 h (Figure 44c), and young 3-week old mice within 24 h, and is also capable of clearing of other organisms, such as zebrafish, rat and chick embryos, *Xenopus* and small octopus, it still requires subsequent RI-matching step in CUBIC-derived mounting solution for a few days. In addition, PRESTO protocol, relying either on standard table-top centrifuge or syringe pump, might be useful for whole-organ immunochemistry, as it was shown to obtain ≈120 μm deep labeling within ≈3 h, the range usually achievable after 2 days of passive immunostaining (Figure 44b).

A next method applied to whole-body clearing was CUBIC,[58] which offered faster (≈2 weeks) and simplified approach not requiring oxygen removal with vacuum chamber as in the case of PARS. CUBIC perfusion decolorizes all organs equally well with the exception of bones, presenting modest transparency (Figure 43b). However, this was recently shown beneficial by Bozycki et al.,[317] who applied CUBIC whole-body clearing to the mdx mouse model of Duchenne muscular dystrophy. By clearing and staining with Alizarin Red, the researchers could visualize uncleared calcium deposits accumulating at sites of muscle necrosis and characterize their discrete 3D distribution in soft tissues of the entire animal (Figure 43c). Another application of CUBIC-perfusion was performed by Kubota et al.,[35] who demonstrated the value of whole-body clearing for the monitoring of tumor metastases in the variety of cancer cell lines (Figure 43d). Recently, we reported an optimized perfusion-based CUBIC whole-body clearing, which greatly accelerates the process and allows to complete also an adult rat whole-body clearing within 4–5 days (**Figure 45**), while retaining histological appearance of the studied organs.[139]

Finally, solvent-based approach was applied for whole-body clearing by the group led by Ertürk.[36] By optimizing previously used combinations of alcohols and solvents, the researchers developed uDISCO protocol, relying on *tert*-butanol dehydration and further RI matching in BABB with addition of diphenyl ether and tocopherol (scavenger of peroxides, presence of which compromise XFP stability, **Figure 46**a). The prominent feature of uDISCO is the extensive tissue shrinkage resulting in up to 65% volume reduction of cleared organs. This, for the first time allowed not only to clear whole body of adult mice and young rats, but also to image them as the one, unsectioned piece from "head to toe" (Figure 46b). In turn, this has opened up new avenues to visualize, for example, the entire central nervous system with subcellular resolution in health and its remodeling during various pathologies, with respect to its connectivity patterns with peripheral organs. By turning all organs transparent, the researchers were able to visualize distribution of bone marrow stem cells in various organs upon intravenous and intraperitoneal injections, trace AAV-injected neurons and their decussation of the descending motor axons at the pyramidal level (Figure 46c). Moreover, uDISCO solutions outperform 3DISCO in terms of XFPs fluorescence preservation by stabilizing them over the course of months

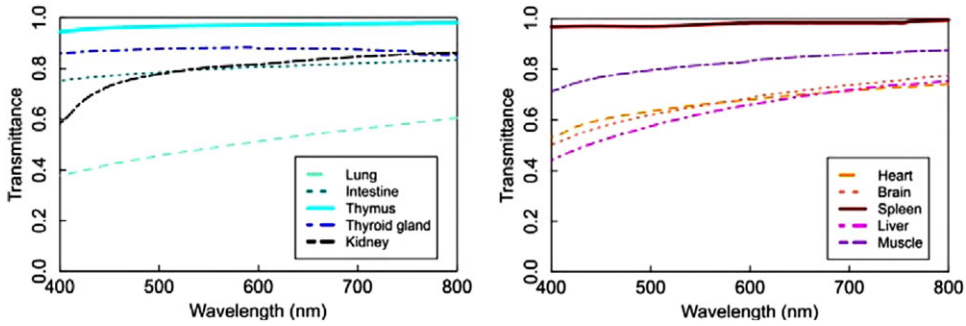

Figure 45. Clearing of the majority of rat peripheral organs is feasible as presented by transmittance curves obtained by using an optimized perfusion-based CUBIC protocol. Reproduced with permission.[139] Copyright 2017, Wiley-VCH.

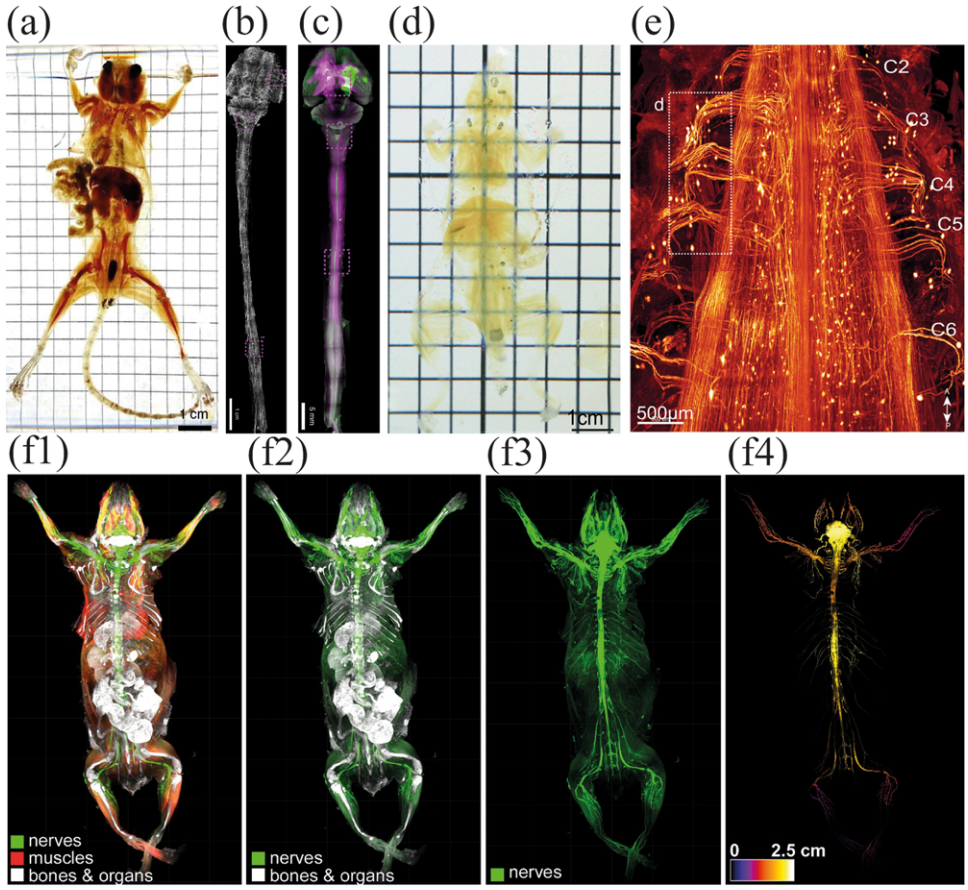

Figure 46. Organic-solvent-based whole-body clearing. a) uDISCO was the first organic-solvent method developed to clear adult mice and young rats. Although no decoloring or decalcifying agents were included, with uDISCO it was feasible to image bones and the majority of the internal organs. b,c) Up to 65% volume reduction allowed the authors to image the entire brain and spinal cord as one intact piece; b) 3D image presenting vasculature of rat central nervous system; c) AAV–Syn–RFP and AAV–Syn–GFP injected brain; note the decussation of descending motor neurons at the pyramidal level. a–c) Reproduced with permission.[36] Copyright 2016, Springer Nature. d) The PEGASOS method, in addition to solvent-based dehydration and RI matching, implements Quadrol and EDTA as decoloring and decalcifying agents, respectively, which contributes to spectacular transparency and for, for example, e) the tracing of individual neurons from the central to the peripheral nervous system. d,e) Reproduced under the terms of the CC-BY Creative Commons Attribution 4.0 license (http://creativecommons.org/licenses/by/4.0/).[55] Copyright 2018, The Authors. Published by Springer Nature. f1–f4) The newest presented whole-body clearing approach, vDISCO, is a 3DISCO variation with Quadrol, EDTA, and Atto-conjugated nanobodies added to the procedure through pressure-forced perfusion. This in turn allows one to clearly distinguish between nanobody-boosted GFP-expressing nerves (f3), propidium iodidestained internal organs (f2), and autofluorescent muscles (f1). f4) The depth color-coding of projections at different *z*-levels. f) Reproduced with permission.[39] Copyright 2018, Springer Nature.

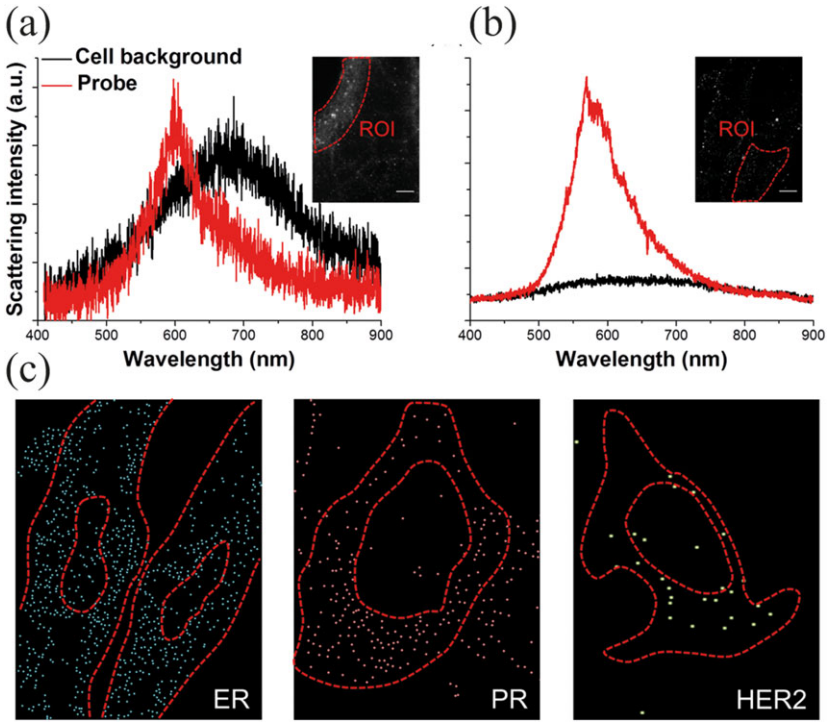

Figure 47. A single-cell optical clearing strategy enhances mRNA detection. a) A single nanoprobe is hardly distinguishable without treatment while b) modified Sca*l*eA2 clearing increases its relative intensity to the cell background and c) allows for the efficient visualization of mRNAs in ER-expressing HeLa cells. ER, estrogen receptor; PR, progesterone receptor; HER2, human epidermal growth factor receptor 2. Adapted with permission.[332] Copyright 2016, American Chemical Society.

and allow for immunostaining of both fresh (1 month) and old (14 month) fixed human biopsy samples. The main limitations of uDISCO are the necessity to handle large volumes of toxic chemicals under the fume hood for days to weeks and modest signal-to-background ratio achieved when XFP signal is being detected in densely packed, autofluorescent tissue. The latter issue was recently resolved by the same group applying bright Atto-conjugated nanobodies through pressure forced perfusion of the animal.[39] By using Atto fluorescent dyes with the peak emission in the far-red spectrum, they increased contrast and prevented the crosstalk between specific fluorescent signal and tissue autofluorescence (most pronounced around 488 nm excitation-emission region, Figure 46f). This approach, named vDISCO, enhanced fluorescent signal up to 118 times and turned it permanent, allowing long-term imaging sessions and re-imaging, as confirmed by the assessment of signal stability over the course of 18 months. Altogether, advanced clearing method, decalcification and decolorization with the diluted CUBIC reagent 1, staining with anti-XFP Atto-conjugated nanobodies serves as promising tool for performing high-contrast imaging of the entire rodents, which was already applied to study cancer metastases and the effectiveness of antibody drug targeting at the cellular level.[40]

Almost simultaneously with vDISCO, a similar whole-body clearing method called PEGASOS (poly(ethylene glycol) (PEG)-associated solvent system) was presented by Jing et al.[55] (Figure 46d,e). As vDISCO, it utilizes perfusion of EDTA for hard tissue decalcification and Quadrol (CUBIC's decolorizing agent) together with 5% ammonium solution for heme removal and organs decolorization. Fluorescent signal intensity was protected, however, by addition of poly(ethylene glycol) methacrylate/poly(ethylene glycol) diacrylate and Quadrol to BABB, the alkaline character (pH > 9.5) of which stabilized native XFPs better than the original uDISCO. PEGASOS was also the first to perform successful clearing of the hardest body tissues—enamel and dentin—the imaging of which revealed pattern of the enriched vascular network.

It should be noted that even though powerful, successful implementation of whole-body clearing techniques requires a specialized group of researchers having good understanding of tissue clearing itself, proper imaging technique with further handling and post processing of large data with high-end computer workstations, as these often exceed dozens of terabytes. Thereby, although published already 4 years ago, whole-body clearing still awaits for the first application from the group outside of the TOC community.

5. Emerging Applications

As expected, optical clearing is limited neither to brain, nor peripheral organs of mammals and as such was already successfully applied to morphological studies of other model vertebrate organisms[318,319] spheroids,[64,320,321] plant tissues,[322,323] as well as insects and crustaceans[324–326] and even implant-tissue interface.[327] Interestingly, amorphous samples such as blood clot[328] or sputum from cystic fibrosis patients[329] can also be cleared and further visualized in situ to reveal spatial distribution of bacteria with associated proteins and nucleic acids and therefore to decipher their otherwise inaccessible microenvironment.

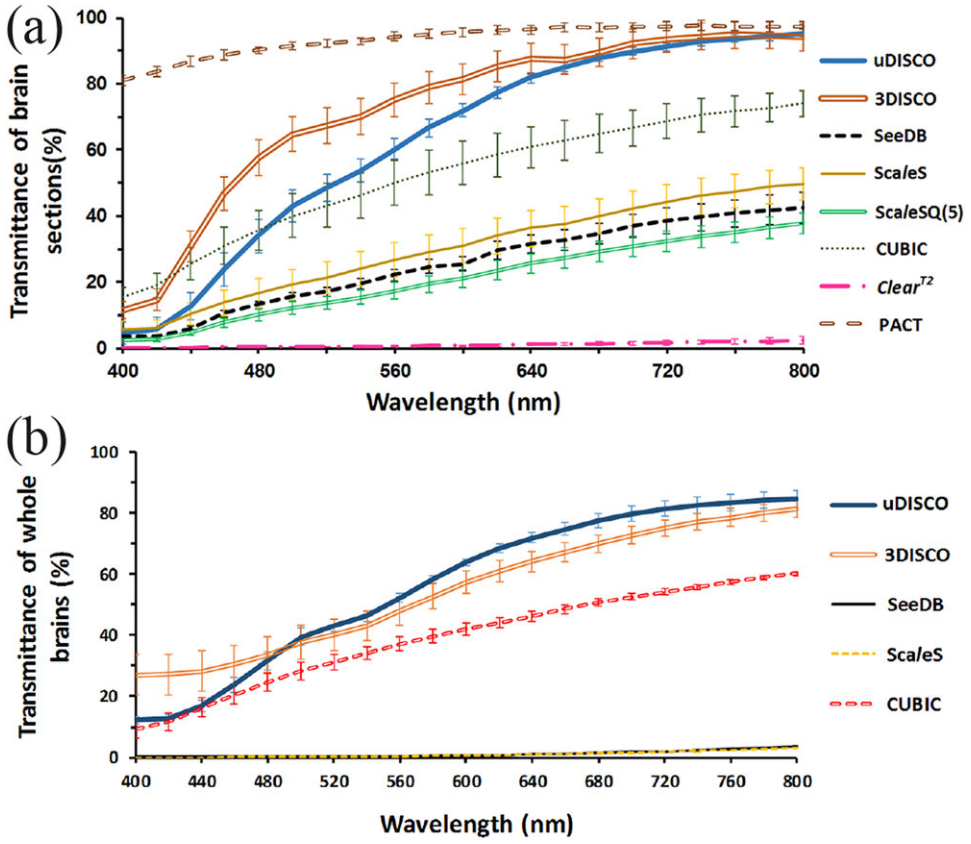

Figure 48. Clearing efficiency with a particular method might be not only organ-specific, but also organ-form dependent. a) Note that, with respect to tissue transmittance, 3DISCO outperforms uDISCO on 2-mm-thick brain slices, while b) being less effective for whole-brain clearing. Reproduced under the terms of the CC-BY Creative Commons Attribution 3.0 Unported license (https://creativecommons.org/licenses/by/3.0/).[337] Copyright 2018, The Authors. Published by SPIE.

Moreover, TOC opens ample avenues to visualize development and spread of endoparasites to study host-parasite interactions in situ at molecular level in 3D, as presented by investigation of *Trichobilharzia regent* migration through murine central nervous system[330] or tracing of malaria parasites development and their accumulation into salivary glands of mosquito vectors.[331]

Combination of optical clearing of single cells with hyperspectral dark-field microscopy leads to a significant increase in signal-to-noise ratio, which in turn allows for simplified detection of proteins, transcripts or intracellularly grown particulates (**Figure 47**), which otherwise (as in the case of in situ hybridization) require perplexing staining with multiple dyes.[332]

6. Further Directions

To conclude, it should be noted that TOC is still a novel, rapidly expanding set of methodologies that require standardization of the described protocols. Until now, the vast majority of methods were proposed as based on serendipitous observations, instead of planned actions, relying on chemical properties of the tested compounds. However, the first advanced steps upon introduction of clearing solutions based on profound, chemical screening, start to emerge and have already contributed to a wide palette of CUBIC clearing reagents.[61,62] It is crucial to develop such deliberated chemical solutions, as obviously no single method can fit all the needs, as readily presented by Kieffer et al.,[251] who already had to apply two chemically distinct approaches (CUBIC and PACT) to study dynamic spread of HIV infection. Moreover, it seems logical, and was recently supported by the detailed study by Kim et al.,[333] that as the organs differ in terms of lipid and protein content along with the cell package, they also require different TOC approaches for the optimal clearing. The authors described the workflow routine which facilitates the side-by-side assessment of contribution of 1) lipid extraction, 2) RI matching, and 3) tissue size alterations, to the final tissue transparency. Noteworthy, they reported 1-mm-thick slices of lung and kidney transparency, but not brain and liver, to be highly dependent on lipid removal. The presented approach, when applied to other organs, might be very insightful as it already helped to clarify why lipid-sparing techniques, such as SeeDB and Clear$^{T/T2}$, were shown useful for deep neuronal tracing, but failed to be broadly utilized with peripheral organs. However, it should be noted that clearing efficacy of millimeter-thick tissue slices does not obviously recapitulate whole-organ clearing conditions (which certainly differs from slices in terms of, e.g., OCAs penetration, efflux of already solvated lipids or organ size alteration, **Figure 48**).

Although the already existing palette of TOC methods is undoubtedly vast and proved to be useful, several tuned protocols such as FDISCO and 2ECi clearly show that seemingly meager

changes might still lead to significant improvements in the field. Presumably, combination of TOC with gold standard techniques, such as Golgi[334,335] or Congo red[336] stainings, will give a new life to this well established methods. Comparative studies, in which many TOC methods are being side-by-side applied to the organ of interest, will also serve as a valuable reference for choosing the most optimal approaches from the plethora of already existing techniques.[337–339]

Acknowledgements

The authors thank J. Damięcka for insightful discussions. This work was supported by Polish Ministry of Science and Higher Education, grant number DI2016 007446 to P.M. and European Commission Horizon 2020 Programme 692180-STREAM H2020-TWINN-2015 to J.G.

Conflict of Interest

The authors declare no conflict of interest.

Keywords

CLARITY, CUBIC, DISCO, light sheet fluorescence microscopy, tissue optical clearing

Received: November 2, 2018
Revised: May 12, 2019
Published online: July 15, 2019

[1] R. S. Tubbs, *Clin. Anat.* **2015**, *28*, 151.
[2] D. Stucht, K. A. Danishad, P. Schulze, F. Godenschweger, M. Zaitsev, O. Speck, *PLoS One* **2015**, *10*, e0133921.
[3] S. Yang, Z. Yang, K. Fischer, K. Zhong, J. Stadler, F. Godenschweger, J. Steiner, H.-J. Heinze, H. Bernstein, B. Bogerts, C. Mawrin, D. C. Reutens, O. Speck, M. Walter, *Front. Neuroanat.* **2013**, *7*, 31.
[4] H. S. Wasan, H. S. Park, K. C. Liu, N. K. Mandir, A. Winnett, P. Sasieni, W. F. Bodmer, R. A. Goodlad, N. A. Wright, *J. Pathol.* **1998**, *185*, 246.
[5] S. Yoshida, M. Sukeno, Y. Nabeshima, *Science* **2007**, *317*, 1722.
[6] O. E. Olarte, J. Andilla, E. J. Gualda, P. Loza-Alvarez, *Adv. Opt. Photonics* **2018**, *10*, 111.
[7] K. Tainaka, A. Kuno, S. I. Kubota, T. Murakami, H. R. Ueda, *Annu. Rev. Cell Dev. Biol.* **2016**, *32*, 713.
[8] D. S. Richardson, J. W. Lichtman, *Cell* **2015**, *162*, 246.
[9] L. Silvestri, I. Costantini, L. Sacconi, F. S. Pavone, *J. Biomed. Opt.* **2016**, *21*, 081205.
[10] T. Yu, Y. Qi, H. Gong, Q. Luo, D. Zhu, *J. Biophotonics* **2018**, *11*, e201700187.
[11] R. Shi, M. Chen, V. V. Tuchin, D. Zhu, *Biomed. Opt. Express* **2015**, *6*, 1977.
[12] X. Yang, Y. Liu, D. Zhu, R. Shi, Q. Luo, *Opt. Express* **2014**, *22*, 1094.
[13] C. Zhang, W. Feng, Y. Zhao, T. Yu, P. Li, T. Xu, Q. Luo, D. Zhu, *Theranostics* **2018**, *8*, 2696.
[14] Y. Zhao, T. Yu, C. Zhang, Z. Li, Q. Luo, T. Xu, D. Zhu, *Light: Sci. Appl.* **2018**, *7*, 17153.
[15] V. V. Tuchin, A. N. Bashkatov, É. A. Genina, Y. P. Sinichkin, N. A. Lakodina, *Tech. Phys. Lett.* **2001**, *27*, 489.
[16] E. A. Genina, A. N. Bashkatov, Y. P. Sinichkin, V. V. Tuchin, *Quantum Electron.* **2006**, *36*, 1119.
[17] A. N. Bashkatov, E. A. Genina, Y. P. Sinichkin, V. V. Tuchin, in *Functional Monitoring and Drug–Tissue Interaction*, International Society for Optics and Photonics, Bellingham, WA, USA **2002**, pp. 144–153.
[18] A. K. Bui, R. A. McClure, J. Chang, C. Stoianovici, J. Hirshburg, A. T. Yeh, B. Choi, *Lasers Surg. Med.* **2009**, *41*, 142.
[19] E. A. Genina, A. N. Bashkatov, Y. P. Sinichkin, I. Y. Yanina, V. V. Tuchin, *J. Biomed. Photonics Eng.* **2015**, *1*, 22.
[20] A. N. Bashkatov, K. V. Berezin, K. N. Dvoretskiy, M. L. Chernavina, E. A. Genina, V. D. Genin, V. I. Kochubey, E. N. Lazareva, A. B. Pravdin, M. E. Shvachkina, P. A. Timoshina, D. K. Tuchina, D. D. Yakovlev, D. A. Yakovlev, I. Y. Yanina, O. S. Zhernovaya, V. V. Tuchin, *JBO* **2018**, *23*, 091416.
[21] K. Chung, J. Wallace, S.-Y. Kim, S. Kalyanasundaram, A. S. Andalman, T. J. Davidson, J. J. Mirzabekov, K. A. Zalocusky, J. Mattis, A. K. Denisin, S. Pak, H. Bernstein, C. Ramakrishnan, L. Grosenick, V. Gradinaru, K. Deisseroth, *Nature* **2013**, *497*, 332.
[22] H. U. Dodt, U. Leischner, A. Schierloh, N. Jährling, C. P. Mauch, K. Deininger, J. M. Deussing, M. Eder, W. Zieglgänsberger, K. Becker, *Nat. Methods* **2007**, *4*, 331.
[23] A. Ertürk, C. P. Mauch, F. Hellal, F. Förstner, T. Keck, K. Becker, N. Jährling, H. Steffens, M. Richter, M. Hübener, E. Kramer, F. Kirchhoff, H. U. Dodt, F. Bradke, *Nat. Med.* **2012**, *18*, 166.
[24] H. Hama, H. Kurokawa, H. Kawano, R. Ando, T. Shimogori, H. Noda, K. Fukami, A. Sakaue-Sawano, A. Miyawaki, *Nat. Neurosci.* **2011**, *14*, 1481.
[25] M. Ke, S. Fujimoto, T. Imai, *Nat. Neurosci.* **2013**, *16*, 1154.
[26] E. A. Susaki, K. Tainaka, D. Perrin, F. Kishino, T. Tawara, T. M. Watanabe, C. Yokoyama, H. Onoe, M. Eguchi, S. Yamaguchi, T. Abe, H. Kiyonari, Y. Shimizu, A. Miyawaki, H. Yokota, H. R. Ueda, *Cell* **2014**, *157*, 726.
[27] L. Chen, G. Li, Y. Li, Y. Li, H. Zhu, L. Tang, P. French, J. McGinty, S. Ruan, *Sci. Rep.* **2017**, *7*, 12218.
[28] T. Yu, J. Zhu, Y. Li, Y. Ma, J. Wang, X. Cheng, S. Jin, Q. Sun, X. Li, H. Gong, Q. Luo, F. Xu, S. Zhao, D. Zhu, *Sci. Rep.* **2018**, *8*, 1964.
[29] H. M. Lai, A. K. L. Liu, H. H. M. Ng, M. H. Goldfinger, T. W. Chau, J. DeFelice, B. S. Tilley, W. M. Wong, W. Wu, S. M. Gentleman, *Nat. Commun.* **2018**, *9*, 1066.
[30] M. Stefaniuk, E. J. Gualda, M. Pawlowska, D. Legutko, P. Matryba, P. Koza, W. Konopka, D. Owczarek, M. Wawrzyniak, P. Loza-Alvarez, L. Kaczmarek, *Sci. Rep.* **2016**, *6*, 28209.
[31] Y. Sato, T. Miyawaki, A. Ouchi, A. Noguchi, S. Yamaguchi, Y. Ikegaya, *Anat. Sci. Int.* **2019**, *94*, 199.
[32] V. Gradinaru, J. Treweek, K. Overton, K. Deisseroth, *Annu. Rev. Biophys.* **2018**, *47*, 355.
[33] J. Seo, M. Choe, S. Kim, *Mol. Cells* **2016**, *39*, 439.
[34] E. Lee, H. J. Kim, W. Sun, *Int. Neurourol. J.* **2016**, *20*, S15.
[35] S. I. Kubota, K. Takahashi, J. Nishida, Y. Morishita, S. Ehata, K. Tainaka, K. Miyazono, H. R. Ueda, *Cell Rep.* **2017**, *20*, 236.
[36] C. Pan, R. Cai, F. P. Quacquarelli, A. Ghasemigharagoz, A. Lourbopoulos, P. Matryba, N. Plesnila, M. Dichgans, F. Hellal, A. Ertürk, *Nat. Methods* **2016**, *13*, 859.
[37] E. A. Susaki, H. R. Ueda, *Cell Chem. Biol.* **2016**, *23*, 137.
[38] B. Yang, J. B. Treweek, R. P. Kulkarni, B. E. Deverman, C.-K. Chen, E. Lubeck, S. Shah, L. Cai, V. Gradinaru, *Cell* **2014**, *158*, 945.
[39] R. Cai, C. Pan, A. Ghasemigharagoz, M. I. Todorov, B. Förstera, S. Zhao, H. S. Bhatia, A. Parra-Damas, L. Mrowka, D. Theodorou, M. Rempfler, A. L. R. Xavier, B. T. Kress, C. Benakis, H. Steinke, S. Liebscher, I. Bechmann, A. Liesz, B. Menze, M. Kerschensteiner, M. Nedergaard, A. Ertürk, *Nat. Neurosci.* **2019**, *22*, 317.
[40] C. Pan, O. Schoppe, A. Parra-Damas, R. Cai, M. I. Todorov, G. Gondi, B. von Neubeck, A. Ghasemi, M. A. Reimer, J. Coronel, B. K. Garvalov, B. Menze, R. Zeidler, A. Erturk, BioRxiv:541862, **2019**.
[41] W. Spalteholz, *Über das Durchsichtigmachen von menschlichen und tierischen Präparaten und seine theoretischen Bedingungen*. S. Hirzel, Leipzig, Germany **1911**.

[42] J. A. Dent, A. G. Polson, M. W. Klymkowsky, *Development* **1989**, *105*, 61.
[43] M. Orlich, F. Kiefer, *Histol. Histopathol.* **2018**, *33*, 181.
[44] K. Becker, N. Jährling, S. Saghafi, R. Weiler, H.-U. Dodt, *PLoS One* **2012**, *7*, e33916.
[45] A. Ertürk, K. Becker, N. Jährling, C. P. Mauch, C. D. Hojer, J. G. Egen, F. Hellal, F. Bradke, M. Sheng, H.-U. Dodt, *Nat. Protoc.* **2012**, *7*, 1983.
[46] M. K. Schwarz, A. Scherbarth, R. Sprengel, J. Engelhardt, P. Theer, G. Giese, *PLoS One* **2015**, *10*, e0124650.
[47] M. Gagaoua, K. Hafid, *Biosens. J.* **2016**, *5*, 100134.
[48] C. Dennison, R. Lovrien, *Protein Expression Purif.* **1997**, *11*, 149.
[49] C. R. E. Dennison, *S. Afr. J. Sci.* **2000**, *96*, 159.
[50] N. Renier, Z. Wu, D. J. Simon, J. Yang, P. Ariel, M. Tessier-Lavigne, *Cell* **2014**, *159*, 896.
[51] N. Renier, E. L. Adams, C. Kirst, Z. Wu, R. Azevedo, J. Kohl, A. E. Autry, L. Kadiri, K. Umadevi Venkataraju, Y. Zhou, V. X. Wang, C. Y. Tang, O. Olsen, C. Dulac, P. Osten, M. Tessier-Lavigne, *Cell* **2016**, *165*, 1789.
[52] M. Belle, D. Godefroy, G. Couly, S. A. Malone, F. Collier, P. Giacobini, A. Chédotal, *Cell* **2017**, *169*, 161.
[53] Y. Li, J. Xu, P. Wan, T. Yu, D. Zhu, *Front. Neuroanat.* **2018**, *12*, 67.
[54] Y. Qi, T. Yu, J. Xu, P. Wan, Y. Ma, J. Zhu, Y. Li, H. Gong, Q. Luo, D. Zhu, *Sci. Adv.* **2019**, *5*, eaau8355.
[55] D. Jing, S. Zhang, W. Luo, X. Gao, Y. Men, C. Ma, X. Liu, Y. Yi, A. Bugde, B. O. Zhou, Z. Zhao, Q. Yuan, J. Q. Feng, L. Gao, W.-P. Ge, H. Zhao, *Cell Res.* **2018**, *28*, 803.
[56] Y. Ma, T. Yu, J. Xu, P. Wan, Y. Qi, W. Feng, D. Zhu, in *Dynamics and Fluctuations in Biomedical Photonics XVI*, International Society for Optics and Photonics, Bellingham, WA, USA **2019**, p. 108770P.
[57] A. Klingberg, A. Hasenberg, I. Ludwig-Portugall, A. Medyukhina, L. Männ, A. Brenzel, D. R. Engel, M. T. Figge, C. Kurts, M. Gunzer, *J. Am. Soc. Nephrol.* **2017**, *28*, 452.
[58] K. Tainaka, S. I. Kubota, T. Q. Suyama, E. A. Susaki, D. Perrin, M. Ukai-Tadenuma, H. Ukai, H. R. Ueda, *Cell* **2014**, *159*, 911.
[59] E. A. Susaki, K. Tainaka, D. Perrin, H. Yukinaga, A. Kuno, H. R. Ueda, *Nat. Protoc.* **2015**, *10*, 1709.
[60] H. Hama, H. Hioki, K. Namiki, T. Hoshida, H. Kurokawa, F. Ishidate, T. Kaneko, T. Akagi, T. Saito, T. Saido, A. Miyawaki, *Nat. Neurosci.* **2015**, *18*, 1518.
[61] K. Tainaka, T. C. Murakami, E. A. Susaki, C. Shimizu, R. Saito, K. Takahashi, A. Hayashi-Takagi, H. Sekiya, Y. Arima, S. Nojima, M. Ikemura, T. Ushiku, Y. Shimizu, M. Murakami, K. F. Tanaka, M. Iino, H. Kasai, T. Sasaoka, K. Kobayashi, K. Miyazono, E. Morii, T. Isa, M. Fukayama, A. Kakita, H. R. Ueda, *Cell Rep.* **2018**, *24*, 2196.
[62] T. C. Murakami, T. Mano, S. Saikawa, S. A. Horiguchi, D. Shigeta, K. Baba, H. Sekiya, Y. Shimizu, K. F. Tanaka, H. Kiyonari, M. Iino, H. Mochizuki, K. Tainaka, H. R. Ueda, *Nat. Neurosci.* **2018**, *21*, 625.
[63] T. Kuwajima, A. A. Sitko, P. Bhansali, C. Jurgens, W. Guido, C. Mason, *Development* **2013**, *140*, 1364.
[64] E. C. Costa, A. F. Moreira, D. de Melo-Diogo, I. J. Correia, *Opt. Laser Technol.* **2018**, *106*, 94.
[65] E. C. Costa, A. F. Moreira, D. de Melo-Diogo, I. J. Correia, *J. Biomed. Opt.* **2018**, *23*, 1.
[66] E. L. Sylwestrak, P. Rajasethupathy, M. A. Wright, A. Jaffe, K. Deisseroth, *Cell* **2016**, *164*, 792.
[67] E. Poguzhelskaya, D. Artamonov, A. Bolshakova, O. Vlasova, I. Bezprozvanny, *Mol. Neurodegener.* **2014**, *9*, 19.
[68] J. B. Treweek, K. Y. Chan, N. C. Flytzanis, B. Yang, B. E. Deverman, A. Greenbaum, A. Lignell, C. Xiao, L. Cai, M. S. Ladinsky, P. J. Bjorkman, C. C. Fowlkes, V. Gradinaru, *Nat. Protoc.* **2015**, *10*, 1860.
[69] H. Zheng, L. Rinaman, *Brain Struct. Funct.* **2016**, *221*, 2375.
[70] S. Kim, J. H. Cho, E. Murray, N. Bakh, H. Choi, K. Ohn, L. Ruelas, A. Hubbert, M. McCue, S. L. Vassallo, P. J. Keller, K. Chung, *Proc. Natl. Acad. Sci. USA* **2015**, *112*, E6274.
[71] J. R. Epp, Y. Niibori, H. Liz Hsiang, V. Mercaldo, K. Deisseroth, S. A. Josselyn, P. W. Frankland, *eNeuro* **2015**, *2*, ENEURO.0022-15.2015.
[72] Y. Ding, J. Lee, J. Ma, K. Sung, T. Yokota, N. Singh, M. Dooraghi, P. Abiri, Y. Wang, R. P. Kulkarni, A. Nakano, T. P. Nguyen, P. Fei, T. K. Hsiai, *Sci. Rep.* **2017**, *7*, 42209.
[73] Y. Ono, I. Nakase, A. Matsumoto, C. Kojima, *J. Biomed. Mater. Res., Part B*, **2019**. https://doi.org/10.1002/jbm.b.34322.
[74] H. M. Lai, A. K. L. Liu, W. Ng, J. DeFelice, W. S. Lee, H. Li, W. Li, H. M. Ng, R. C. Chang, B. Lin, W. Wu, S. M. Gentleman, *PLoS One* **2016**, *11*, e0158628.
[75] K. H. R. Jensen, R. W. Berg, *J. Chem. Neuroanat.* **2017**, *86*, 19.
[76] E. Murray, J. H. Cho, D. Goodwin, T. Ku, J. Swaney, S. Kim, H. Choi, Y. Park, J. Park, A. Hubbert, M. McCue, S. Vassallo, N. Bakh, M. P. Frosch, V. J. Wedeen, H. S. Seung, K. Chung, *Cell* **2015**, *163*, 1500.
[77] Y. Park, C. H. Sohn, R. Chen, M. McCue, D. H. Yun, G. T. Drummond, T. Ku, N. B. Evans, H. C. Oak, W. Trieu, H. Choi, X. Jin, V. Lilascharoen, J. Wang, M. C. Truttmann, H. W. Qi, H. L. Ploegh, T. R. Golub, S.-C. Chen, M. P. Frosch, H. J. Kulik, B. K. Lim, K. Chung, *Nat. Biotechnol.* **2019**, *37*, 73.
[78] T. Ku, J. Swaney, J. Park, A. Albanese, E. Murray, J. H. Cho, Y. Park, V. Mangena, J. Chen, K. Chung, *Nat. Biotechnol.* **2016**, *34*, 973.
[79] D. Unnersjö-Jess, L. Scott, S. Z. Sevilla, J. Patrakka, H. Blom, H. Brismar, *Kidney Int.* **2018**, *93*, 1008.
[80] S. Alon, G. H. Huynh, E. S. Boyden, *FEBS J.* **2018**, *286*, 1482.
[81] S. Tseng, Y. Lee, Z. Chen, H. Lin, C. Lin, S. Tang, *J. Biomed. Opt.* **2009**, *14*, 044004.
[82] Y. Aoyagi, R. Kawakami, H. Osanai, T. Hibi, T. Nemoto, *PLoS One* **2015**, *10*, e0116280.
[83] T. Staudt, M. C. Lang, R. Medda, J. Engelhardt, S. W. Hell, *Microsc. Res. Tech.* **2007**, *70*, 1.
[84] P. S. Tsai, J. P. Kaufhold, P. Blinder, B. Friedman, P. J. Drew, H. J. Karten, P. D. Lyden, D. Kleinfeld, *J. Neurosci.* **2009**, *29*, 14553.
[85] M. Ke, Y. Nakai, S. Fujimoto, R. Takayama, S. Yoshida, T. S. Kitajima, M. Sato, T. Imai, *Cell Rep.* **2016**, *14*, 2718.
[86] B. Hou, D. Zhang, S. Zhao, M. Wei, Z. Yang, S. Wang, J. Wang, X. Zhang, B. Liu, L. Fan, Y. Li, Z. Qiu, C. Zhang, T. Jiang, *Front. Neuroanat.* **2015**, *9*, 19.
[87] W. Li, R. N. Germain, M. Y. Gerner, *Proc. Natl. Acad. Sci. USA* **2017**, *114*, E7321.
[88] A. J. Moy, B. V. Capulong, R. B. Saager, M. P. Wiersma, P. C. Lo, A. J. Durkin, B. Choi, *J. Biomed. Opt.* **2015**, *20*, 095010.
[89] C. Wu, T. Fu, Y. Chou, S. Yeh, *PLoS One* **2015**, *10*, e0121335.
[90] H. Diekmann, P. Kalbhen, D. Fischer, *Front. Cell Neurosci.* **2015**, *9*, 118.
[91] B. Lee, R. Johnston, Y. Yang, A. Gallavotti, M. Kojima, B. A. N. Travençolo, L. F. da Costa, H. Sakakibara, D. Jackson, *Plant Physiol.* **2009**, *150*, 205.
[92] S. Tang, Y. Fu, W. Lo, T. Hua, H. Tuan, *ACS Nano* **2010**, *4*, 6278.
[93] I. Costantini, J. Ghobril, A. P. Di Giovanna, A. L. Allegra Mascaro, L. Silvestri, M. C. Müllenbroich, L. Onofri, V. Conti, F. Vanzi, L. Sacconi, R. Guerrini, H. Markram, G. Iannello, F. S. Pavone, *Sci. Rep.* **2015**, *5*, 9808.
[94] T. Yu, Y. Qi, J. Zhu, J. Xu, H. Gong, Q. Luo, D. Zhu, *Sci. Rep.* **2017**, *7*, 38848.
[95] S. Sindhwani, A. M. Syed, S. Wilhelm, W. C. W. Chan, *Bioconjugate Chem.* **2017**, *28*, 253.
[96] F. Chen, P. W. Tillberg, E. S. Boyden, *Science* **2015**, *347*, 543.
[97] P. W. Tillberg, F. Chen, K. D. Piatkevich, Y. Zhao, C. Yu, B. P. English, L. Gao, A. Martorell, H. Suk, F. Yoshida, E. M. DeGennaro, D. H. Roossien, G. Gong, U. Seneviratne, S. R. Tannenbaum, R. Desimone, D. Cai, E. S. Boyden, *Nat. Biotechnol.* **2016**, *34*, 987.
[98] F. Chen, A. T. Wassie, A. J. Cote, A. Sinha, S. Alon, S. Asano, E. R. Daugharthy, J.-B. Chang, A. Marblestone, G. M. Church, A. Raj, E. S. Boyden, *Nat. Methods* **2016**, *13*, 679.

[99] Y. Zhao, O. Bucur, H. Irshad, F. Chen, A. Weins, A. L. Stancu, E. Oh, M. DiStasio, V. Torous, B. Glass, I. E. Stillman, S. J. Schnitt, A. H. Beck, E. S. Boyden, *Nat. Biotechnol.* **2017**, *35*, 757.
[100] J. Chang, F. Chen, Y. Yoon, E. E. Jung, H. Babcock, J. S. Kang, S. Asano, H. Suk, N. Pak, P. W. Tillberg, A. T. Wassie, D. Cai, E. S. Boyden, *Nat. Methods* **2017**, *14*, 593.
[101] J. Y. Kim, H. J. Kim, M. J. Jang, J. H. Kim, J. Lee, E. Lee, K. Park, H. Kim, J. Lee, J. Kwag, N. Kim, M. Song, H. Kim, W. Sun, *Sci. Rep.* **2018**, *8*, 8531.
[102] W. Masselink, D. Reumann, P. Murawala, P. Pasierbek, Y. Taniguchi, F. Bonnay, K. Meixner, J. A. Knoblich, E. M. Tanaka, *Development* **2019**, *146*, 1dev166884.
[103] K. D. Piatkevich, V. N. Malashkevich, K. S. Morozova, N. A. Nemkovich, S. C. Almo, V. V. Verkhusha, *Sci. Rep.* **2013**, *33*, 1847.
[104] K. M. Alkaabi, A. Yafea, S. S. Ashraf, *Appl. Biochem. Biotechnol.* **2005**, *126*, 149.
[105] D. J. Scott, N. J. Gunn, K. J. Yong, V. C. Wimmer, N. A. Veldhuis, L. M. Challis, M. Haidar, S. Petrou, R. A. D. Bathgate, M. D. W. Griffin, *Sci. Rep.* **2018**, *8*, 667.
[106] R. Tomer, L. Ye, B. Hsueh, K. Deisseroth, *Nat. Protoc.* **2014**, *9*, 1682.
[107] R. Jorand, G. Le Corre, J. Andilla, A. Maandhui, C. Frongia, V. Lobjois, B. Ducommun, C. Lorenzo, *PLoS One* **2012**, *7*, e35795.
[108] S. Saghafi, K. Becker, C. Hahn, H. U. Dodt, *J. Biophotonics* **2014**, *7*, 117.
[109] M. Pende, K. Becker, M. Wanis, S. Saghafi, R. Kaur, C. Hahn, N. Pende, M. Foroughipour, T. Hummel, H.-U. Dodt, *Nat. Commun.* **2018**, *9*, 4731.
[110] A. Masson, P. Escande, C. Frongia, G. Clouvel, B. Ducommun, C. Lorenzo, *Sci. Rep.* **2015**, *5*, 16898.
[111] J. Nylk, K. McCluskey, S. Aggarwal, J. A. Tello, K. Dholakia, *Biomed. Opt. Express* **2016**, *7*, 4021.
[112] M. C. Müllenbroich, L. Silvestri, A. P. D. Giovanna, G. Mazzamuto, I. Costantini, L. Sacconi, F. S. Pavone, *eNeuro* **2018**, *5*, ENEURO.e0124-18.2018.
[113] D. P. Ryan, E. A. Gould, G. J. Seedorf, O. Masihzadeh, S. H. Abman, S. Vijayaraghavan, W. B. Macklin, D. Restrepo, D. P. Shepherd, *Nat. Commun.* **2017**, *8*, 612.
[114] P. Fei, J. Nie, J. Lee, Y. Ding, S. Li, H. Zhang, M. Hagiwara, T. Yu, T. Segura, C. Ho, D. Zhu, T. K. Hsiai, *AP* **2019**, *1*, 016002.
[115] B. Migliori, M. S. Datta, C. Dupre, M. C. Apak, S. Asano, R. Gao, E. S. Boyden, O. Hermanson, R. Yuste, R. Tomer, *BMC Biol.* **2018**, *16*, 57.
[116] A. K. Glaser, N. P. Reder, Y. Chen, E. F. McCarty, C. Yin, L. Wei, Y. Wang, L. D. True, J. T. C. Liu, *Nat. Biomed. Eng.* **2017**, *1*, 0084.
[117] A. K. Glaser, N. P. Reder, Y. Chen, C. Yin, L. Wei, S. Kang, L. A. Barner, W. Xie, E. F. McCarty, C. Mao, A. R. Halpern, C. R. Stoltzfus, J. S. Daniels, M. Y. Gerner, P. R. Nicovich, J. C. Vaughan, L. D. True, J. T. C. Liu, BioRxiv:548107, **2019**.
[118] J. Mayer, A. Robert-Moreno, J. Sharpe, J. Swoger, *Light: Sci. Appl.* **2018**, *7*, 70.
[119] H. S. Sakhalkar, M. Dewhirst, T. Oliver, Y. Cao, M. Oldham, *Phys. Med. Biol.* **2007**, *52*, 2035.
[120] N. Tinne, G. C. Antonopoulos, S. Mohebbi, J. Andrade, L. Nolte, H. Meyer, A. Heisterkamp, O. Majdani, T. Ripken, *PLoS One* **2017**, *12*, e0184069.
[121] K. H. Dekker, J. J. Battista, K. J. Jordan, *Phys. Med. Biol.* **2017**, *62*, 2636.
[122] J. Sharpe, *Science* **2002**, *296*, 541.
[123] M. Oldham, H. Sakhalkar, T. Oliver, G. Allan Johnson, M. Dewhirst, *J. Biomed. Opt.* **2008**, *13*, 021113.
[124] L. Nolte, N. Tinne, J. Schulze, D. Heinemann, G. C. Antonopoulos, H. Meyer, H. G. Nothwang, T. Lenarz, A. Heisterkamp, A. Warnecke, T. Ripken, *PLoS One* **2017**, *12*, e0175431.
[125] C. Leuze, M. Aswendt, E. Ferenczi, C. W. Liu, B. Hsueh, M. Goubran, Q. Tian, G. Steinberg, M. M. Zeineh, K. Deisseroth, J. A. McNab, *NeuroImage* **2017**, *156*, 412.
[126] E. H. Chang, M. Argyelan, M. Aggarwal, T.-S. S. Chandon, K. H. Karlsgodt, S. Mori, A. K. Malhotra, *NeuroImage* **2017**, *147*, 253.
[127] K. Baek, S. Jung, J. Lee, E. Min, W. Jung, H. Cho, *Sci. Rep.* **2019**, *9*, 2923.
[128] A. d'Esposito, D. Nikitichev, A. Desjardins, S. Walker-Samuel, M. F. Lythgoe, *J. Biomed. Opt.* **2015**, *20*, 080503.
[129] A. Lichtenegger, D. J. Harper, M. Augustin, P. Eugui, M. Muck, J. Gesperger, C. K. Hitzenberger, A. Woehrer, B. Baumann, *Biomed. Opt. Express* **2017**, *8*, 4007.
[130] A. Lichtenegger, M. Muck, P. Eugui, D. J. Harper, M. Augustin, K. Leskovar, C. K. Hitzenberger, A. Woehrer, B. Baumann, *Neurophotonics* **2018**, *5*, 035002.
[131] J. Ren, H. Choi, K. Chung, B. E. Bouma, *Sci. Rep.* **2017**, *7*, 46306.
[132] M. N. Economo, N. G. Clack, L. D. Lavis, C. R. Gerfen, K. Svoboda, E. W. Myers, J. Chandrashekar, *eLife* **2016**, *5*, e10566.
[133] M. Wei, L. Shi, Y. Shen, Z. Zhao, A. Guzman, L. J. Kaufman, L. Wei, W. Min, *Proc. Natl. Acad. Sci. USA* **2019**, 201813044.
[134] S. Y. Ho, *Eur. J. Echocardiogr.* **2009**, *10*, i3.
[135] H. Kolesová, M. Čapek, B. Radochová, J. Janáček, D. Sedmera, *Histochem. Cell Biol.* **2016**, *146*, 141.
[136] I. Nehrhoff, D. Bocancea, J. Vaquero, J. J. Vaquero, J. Ripoll, M. Desco, M. V. Gómez-Gaviro, *Biomed. Opt. Express* **2016**, *7*, 3716.
[137] W. M. S. Qureshi, L. Miao, D. Shieh, J. Li, Y. Lu, S. Hu, M. Barroso, J. Mazurkiewicz, M. Wu, *J. Visualized Exp.* **2016**, e54303.
[138] M. F. Cuccarese, J. M. Dubach, C. Pfirschke, C. Engblom, C. Garris, M. A. Miller, M. J. Pittet, R. Weissleder, *Nat. Commun.* **2017**, *8*, 14293.
[139] P. Matryba, L. Bozycki, M. Pawłowska, L. Kaczmarek, M. Stefaniuk, *J. Biophotonics* **2018**, *11*, e201700248.
[140] I. Nehrhoff, J. Ripoll, R. Samaniego, M. Desco, M. V. Gómez-Gaviro, *Biomed. Opt. Express* **2017**, *8*, 3110.
[141] H. Kolesová, M. Bartoš, W. C. Hsieh, V. Olejníčková, D. Sedmera, *Dev. Dyn.* **2018**, *247*, 1018.
[142] J. Li, L. Miao, D. Shieh, E. Spiotto, J. Li, B. Zhou, A. Paul, R. J. Schwartz, A. B. Firulli, H. A. Singer, G. Huang, M. Wu, *Cell Rep.* **2016**, *15*, 158.
[143] Z. Wang, J. Zhang, G. Fan, H. Zhao, X. Wang, J. Zhang, P. Zhang, W. Wang, *Biomed. Opt. Express* **2018**, *9*, 423.
[144] P. Fei, J. Lee, R. R. S. Packard, K. I. Sereti, H. Xu, J. Ma, Y. Ding, H. Kang, H. Chen, K. Sung, R. Kulkarni, R. Ardehali, C. J. Kuo, X. Xu, C. Ho, T. K. Hsiai, *Sci. Rep.* **2016**, *6*, 22489.
[145] S. Ivins, C. Roberts, B. Vernay, P. J. Scambler, *J. Visualized Exp.* **2016**, e54800.
[146] G. Sommer, A. J. Schriefl, M. Andrä, M. Sacherer, C. Viertler, H. Wolinski, G. A. Holzapfel, *Acta Biomater.* **2015**, *24*, 172.
[147] C. E. Miller, R. P. Thompson, M. R. Bigelow, G. Gittinger, T. C. Trusk, D. Sedmera, *Microsc. Microanal.* **2005**, *11*, 216.
[148] R. M. Smith, A. Matiukas, C. W. Zemlin, A. M. Pertsov, *Microsc. Res. Tech.* **2008**, *71*, 510.
[149] M. Sivaguru, G. Fried, B. S. Sivaguru, V. A. Sivaguru, X. Lu, K. H. Choi, M. T. A. Saif, B. Lin, S. Sadayappan, *BioTechniques* **2015**, *59*, 295.
[150] Trincot Claire E., Xu Wenjing, Zhang Hua, Kulikauskas Molly R., Caranasos Thomas G., Jensen Brian C., Sabine Amélie, Petrova Tatiana V., Caron Kathleen M., *Circ. Res.* **2019**, *124*, 101.
[151] K. Sung, Y. Ding, J. Ma, H. Chen, V. Huang, M. Cheng, C. F. Yang, J. T. Kim, D. Eguchi, D. D. Carlo, T. K. Hsiai, A. Nakano, R. P. Kulkarni, *Sci. Rep.* **2016**, *6*, 30736.
[152] K. Sereti, N. B. Nguyen, P. Kamran, P. Zhao, S. Ranjbarvaziri, S. Park, S. Sabri, J. L. Engel, K. Sung, R. P. Kulkarni, Y. Ding, T. K. Hsiai, K.

Plath, J. Ernst, D. Sahoo, H. K. A. Mikkola, M. L. Iruela-Arispe, R. Ardehali, *Nat. Commun.* **2018**, *9*, 754.
[153] J. Yu, M. M. Seldin, K. Fu, S. Li, L. Lam, P. Wang, Y. Wang, D. Huang, T. L. Nguyen, B. Wei, R. P. Kulkarni, D. Di Carlo, M. Teitell, M. Pellegrini, A. J. Lusis, A. Deb, *Circ. Res.* **2018**, *123*, 73.
[154] F. Perbellini, A. K. L. Liu, S. A. Watson, I. Bardi, S. M. Rothery, C. M. Terracciano, *Sci. Rep.* **2017**, *7*, 5188.
[155] M. Hulsmans, S. Clauss, L. Xiao, A. D. Aguirre, K. R. King, A. Hanley, W. J. Hucker, E. M. Wülfers, G. Seemann, G. Courties, Y. Iwamoto, Y. Sun, A. J. Savol, H. B. Sager, K. J. Lavine, G. A. Fishbein, D. E. Capen, N. D. Silva, L. Miquerol, H. Wakimoto, C. E. Seidman, J. G. Seidman, R. I. Sadreyev, K. Naxerova, R. N. Mitchell, D. Brown, P. Libby, R. Weissleder, F. K. Swirski, P. Kohl, C. Vinegoni, D. J. Milan, P. T. Ellinor, M. Nahrendorf, *Cell* **2017**, *169*, 510.
[156] K. A. Jackson, D. S. Snyder, M. A. Goodell, *Stem Cells* **2004**, *22*, 180.
[157] E. A. Genina, A. N. Bashkatov, M. D. Kozintseva, V. V. Tuchin, *Opt. Spectrosc.* **2016**, *120*, 20.
[158] L. M. Oliveira, M. I. Carvalho, E. M. Nogueira, V. V. Tuchin, *J. Biophotonics* **2018**, *11*, e201700094.
[159] A. R. Burdi, *Stain Technol.* **1965**, *40*, 45.
[160] G. Dingerkus, *Stain Technol.* **1981**, *56*, 128.
[161] E. Wada, M. Yoshida, Y. Kojima, I. Nonaka, K. Ohashi, Y. Nagata, M. Shiozuka, M. Date, T. Higashi, I. Nishino, R. Matsuda, *Am. J. Pathol.* **2014**, *184*, 3094.
[162] H. Sakata-Haga, M. Uchishiba, H. Shimada, T. Tsukada, M. Mitani, T. Arikawa, H. Shoji, T. Hatta, *Sci. Rep.* **2018**, *8*, 7453.
[163] R. LaComb, O. Nadiarnykh, S. Carey, P. J. Campagnola, *J. Biomed. Opt.* **2008**, *13*, 021109.
[164] O. Nadiarnykh, P. J. Campagnola, *Opt. Express* **2009**, *17*, 5794.
[165] S. Plotnikov, V. Juneja, A. B. Isaacson, W. A. Mohler, P. J. Campagnola, *Biophys. J.* **2006**, *90*, 328.
[166] L. Decroix, V. Van Muylder, L. Desender, M. Sampaolesi, L. Thorrez, *Biotech. Histochem.* **2015**, *90*, 424.
[167] A. Milgroom, E. Ralston, *Cell Biol. Int.* **2016**, *40*, 478.
[168] M. Verma, B. S. Murkonda, Y. Asakura, A. Asakura, *Methods Mol. Biol.* **2016**, *1460*, 129.
[169] W. L. Zhang, S. H. Liu, W. C. Zhang, W. Hu, M. Jiang, A. Tamadon, Y. Feng, *Cell J.* **2018**, *20*, 132.
[170] T. Hua, T. Yang, W. Yang, K. Liu, S. Tang, *Front. Neuroanat.* **2013**, *7*.
[171] X. Yin, T. Yu, B. Chen, J. Xu, W. Chen, Y. Qi, P. Zhang, Y. Li, Y. Kou, Y. Ma, N. Han, P. Wan, Q. Luo, D. Zhu, B. Jiang, *Theranostics* **2019**, *9*, 734.
[172] M. M. Khan, D. Lustrino, W. A. Silveira, F. Wild, T. Straka, Y. Issop, E. O'Connor, D. Cox, M. Reischl, T. Marquardt, D. Labeit, S. Labeit, E. Benoit, J. Molgó, H. Lochmüller, V. Witzemann, I. C. Kettelhut, L. C. C. Navegantes, T. Pozzan, R. Rudolf, *Proc. Natl. Acad. Sci. USA* **2016**, *113*, 746.
[173] T. Straka, V. Vita, K. Prokshi, S. J. Hörner, M. M. Khan, M. Pirazzini, M. P. I. Williams, M. Hafner, T. Zaglia, R. Rudolf, *Int. J. Mol. Sci.* **2018**, *19*, 11935.
[174] M. P. I. Williams, M. Rigon, T. Straka, S. J. Hörner, M. Thiel, N. Gretz, M. Hafner, M. Reischl, R. Rudolf, *Front. Cell. Neurosci.* **2019**, *13*.
[175] J. Hirshburg, B. Choi, J. S. Nelson, A. T. Yeh, *J. Biomed. Opt.* **2006**, *11*, 040501.
[176] A. N. Bashkatov, E. A. Genina, V. I. Kochubey, V. V. Tuchin, *J. Phys. D: Appl. Phys.* **2005**, *38*, 2543.
[177] A. Bensimon-Brito, J. Cardeira, G. Dionísio, A. Huysseune, M. L. Cancela, P. E. Witten, *BMC Dev. Biol.* **2016**, *16*, 2.
[178] D. Zhu, K. V. Larin, Q. Luo, V. V. Tuchin, *Laser Photonics Rev.* **2013**, *7*, 732.
[179] H. Chang, Y. Wang, H. Wu, J. Nathans, *J. Visualized Exp.* **2014**, e51749.
[180] H. Liang, B. Akladios, C. P. Canales, R. Francis, E. H. Hardeman, A. Beverdam, *J. Visualized Exp.* **2016**, e54401.
[181] S. Abadie, C. Jardet, J. Colombelli, B. Chaput, A. David, J. Grolleau, P. Bedos, V. Lobjois, P. Descargues, J. Rouquette, *Skin Res. Technol.* **2018**, *24*, 294.
[182] A. Azaripour, T. Lagerweij, C. Scharfbillig, A. E. Jadczak, B. Willershausen, C. J. F. Van Noorden, *Prog. Histochem. Cytochem.* **2016**, *51*, 9.
[183] A. Ascenzi, C. Fabry, *J. Cell Biol.* **1959**, *6*, 139.
[184] D. W. Leonard, K. M. Meek, *Biophys. J.* **1997**, *72*, 1382.
[185] S. Calve, A. Ready, C. Huppenbauer, R. Main, C. P. Neu, *PLoS One* **2015**, *10*, e0116662.
[186] C. P. Neu, T. Novak, K. F. Gilliland, P. Marshall, S. Calve, *Osteoarthritis Cartilage* **2015**, *23*, 405.
[187] M. Acar, K. S. Kocherlakota, M. M. Murphy, J. G. Peyer, H. Oguro, C. N. Inra, C. Jaiyeola, Z. Zhao, K. Luby-Phelps, S. J. Morrison, *Nature* **2015**, *526*, 126.
[188] A. Greenbaum, K. Y. Chan, T. Dobreva, D. Brown, D. H. Balani, R. Boyce, H. M. Kronenberg, H. J. McBride, V. Gradinaru, *Sci. Transl. Med.* **2017**, *9*, eaah6518.
[189] S. Urata, T. Iida, M. Yamamoto, Y. Mizushima, C. Fujimoto, Y. Matsumoto, T. Yamasoba, S. Okabe, *eLife* **2019**, *8*, e40946.
[190] I. M. Berke, J. P. Miola, M. A. David, M. K. Smith, C. Price, *PLoS One* **2016**, *11*, e0150268.
[191] J. M. Hirshburg, K. M. Ravikumar, W. Hwang, A. T. Yeh, *J. Biomed. Opt.* **2010**, *15*, 055002.
[192] D. Stegner, J. M. M. vanEeuwijk, O. Angay, M. G. Gorelashvili, D. Semeniak, J. Pinnecker, P. Schmithausen, I. Meyer, M. Friedrich, S. Dütting, C. Brede, A. Beilhack, H. Schulze, B. Nieswandt, K. G. Heinze, *Nat. Commun.* **2017**, *8*, 127.
[193] M. G. Gorelashvili, K. G. Heinze, D. Stegner, *Methods Mol. Biol.* **2018**, *1812*, 233.
[194] A. Azaripour, T. Lagerweij, C. Scharfbillig, A. E. Jadczak, B. van der Swaan, M. Molenaar, R. van der Waal, K. Kielbassa, W. Tigchelaar, D. I. Picavet, A. Jonker, E. M. L. Hendrikx, V. V. V. Hira, M. Khurshed, C. J. F. V. Noorden, *Sci. Rep.* **2018**, *8*, 1647.
[195] P. L. Appleton, A. J. Quyn, S. Swift, I. Näthke, *J. Microsc.* **2009**, *234*, 196.
[196] Y. Fu, C. Lin, G. Enikolopov, E. Sibley, A. Chiang, S. Tang, *Gastroenterology* **2009**, *137*, 453.
[197] Y. Fu, S. Tang, *Microvasc. Res.* **2010**, *80*, 512.
[198] Y. Fu, S. Peng, H. Lin, P. J. Pasricha, S. Tang, *Am. J. Physiol.: Gastrointest. Liver Physiol.* **2013**, *304*, G1.
[199] Y. Liu, S. Pan, Y. Hou, M. Shen, S. Peng, S. Tang, Y. Chung, *PLoS One* **2013**, *8*, e81857.
[200] Y. Liu, Y. Chung, M. Shen, S. Pan, C. Kuo, S. Peng, P. J. Pasricha, S. Tang, *Cell. Mol. Gastroenterol. Hepatol.* **2015**, *1*, 102.
[201] Y. A. Liu, Y. C. Chung, S. T. Pan, M. Y. Shen, Y. C. Hou, S. J. Peng, P. J. Pasricha, S. C. Tang, *Neurogastroenterol. Motil.* **2013**, *25*, e324.
[202] C. Y. Liu, P. E. Dubé, N. Girish, A. T. Reddy, D. B. Polk, *Am. J. Physiol.: Gastrointest. Liver Physiol.* **2015**, *308*, G721.
[203] P. H. Neckel, U. Mattheus, B. Hirt, L. Just, A. F. Mack, *Sci. Rep.* **2016**, *6*, 34331.
[204] J. A. Kaufman, M. J. Castro, N. Sandoval-Skeet, L. Al-Nakkash, *J. Anat.* **2018**, *232*, 152.
[205] A. Candeo, I. Sana, E. Ferrari, L. Maiuri, C. D'Andrea, G. Valentini, A. Bassi, *J. Biomed. Opt.* **2016**, *21*, 056001.
[206] S. Tang, L. Baeyens, C. Shen, S. Peng, H. Chien, D. W. Scheel, C. E. Chamberlain, M. S. German, *Diabetologia* **2018**, *61*, 168.
[207] R. Das, A. Agrawal, M. P. Upton, E. J. Seibel, in *Optical Interactions with Tissue and Cells XXV; and Terahertz for Biomedical Applications*, International Society for Optics and Photonics, Bellingham, WA, USA **2014**, p. 89410N.
[208] M. Hara, R. F. Dizon, B. S. Glick, C. S. Lee, K. H. Kaestner, D. W. Piston, V. P. Bindokas, *Am. J. Physiol.: Endocrinol. Metab.* **2006**, *290*, E1041.

[209] Y. Fu, C. Lu, C. Lin, J. Juang, G. Enikolopov, E. Sibley, A. Chiang, S. Tang, *J. Biomed. Opt.* **2010**, *15*, 046018.
[210] Y. Chiu, T. Hua, Y. Fu, P. J. Pasricha, S. Tang, *Diabetologia* **2012**, *55*, 3252.
[211] S. Tang, Y. Chiu, C. Hsu, S. Peng, Y. Fu, *Diabetologia* **2013**, *56*, 2424.
[212] H. Chien, S. Peng, T. Hua, C. Kuo, J. Juang, S. Tang, *Int. J. Obes.* **2016**, *40*, 685.
[213] S. Tang, C. Shen, P. Lin, S. Peng, H. Chien, Y. Chou, C. E. Chamberlain, P. J. Pasricha, *Diabetologia* **2018**, *61*, 158.
[214] P. Lin, S. Peng, C. Shen, P. J. Pasricha, S. Tang, *Am. J. Physiol.: Gastrointest. Liver Physiol.* **2016**, *311*, G412.
[215] J. Juang, S. Peng, C. Kuo, S. Tang, *Am. J. Physiol.: Endocrinol. Metab.* **2014**, *306*, E559.
[216] J. Juang, C. Kuo, S. Peng, S. Tang, *EBioMedicine* **2015**, *2*, 109.
[217] M. D. Muzumdar, K. J. Dorans, K. M. Chung, R. Robbins, T. Tammela, V. Gocheva, C. M. C. Li, T. Jacks, *Nat. Commun.* **2016**, *7*, 12685.
[218] E. Butterworth, W. Dickerson, V. Vijay, K. Weitzel, J. Cooper, E. W. Atkinson, J. E. Coleman, K. J. Otto, M. Campbell-Thompson, *J. Visualized Exp.* **2018**.
[219] W. Nishimura, A. Sakaue-Sawano, S. Takahashi, A. Miyawaki, K. Yasuda, Y. Noda, *Islets* **2018**, *10*, e1451282.
[220] J. L. Fowler, S. S. Lee, Z. C. Wesner, S. K. Olehnik, S. J. Kron, M. Hara, *Endocrinology* **2018**, *159*, 1393.
[221] S. S. Lee, V. P. Bindokas, S. J. Kron, *Mol. Cancer Ther.* **2019**, *18*, 213.
[222] H. Tran Thi Nhu, R. Arrojo E. Drigo, P. Berggren, T. Boudier, *Sci. Rep.* **2017**, *7*, 44261.
[223] H. Mizutani, S. Ono, T. Ushiku, Y. Kudo, M. Ikemura, N. Kageyama, N. Yamamichi, M. Fujishiro, T. Someya, M. Fukayama, K. Koike, H. Onodera, *Pathol. Int.* **2018**, *68*, 102.
[224] L. A. Sapirstein, *Am. J. Physiol.: Legacy Content* **1958**, *193*, 161.
[225] F. Medigreceanu, *Proc. R. Soc. B* **1910**, *82*, 286.
[226] Y. Chung-Davidson, P. J. Davidson, A. M. Scott, E. J. Walaszczyk, C. O. Brant, T. Buchinger, N. S. Johnson, W. Li, *J. Visualized Exp.* **2014**.
[227] J. Font-Burgada, S. Shalapour, S. Ramaswamy, B. Hsueh, D. Rossell, A. Umemura, K. Taniguchi, H. Nakagawa, M. A. Valasek, L. Ye, J. L. Kopp, M. Sander, H. Carter, K. Deisseroth, I. M. Verma, M. Karin, *Cell* **2015**, *162*, 766.
[228] R. Torres, S. Vesuna, M. J. Levene, *Arch. Pathol. Lab. Med.* **2014**, *138*, 395.
[229] N. Tanimizu, K. Kaneko, T. Itoh, N. Ichinohe, M. Ishii, T. Mizuguchi, K. Hirata, A. Miyajima, T. Mitaka, *Hepatology* **2016**, *64*, 175.
[230] K. Kaneko, K. Kamimoto, A. Miyajima, T. Itoh, *Hepatology* **2015**, *61*, 2056.
[231] P. Protiva, J. Gong, B. Sreekumar, R. Torres, X. Zhang, G. S. Belinsky, M. Cornwell, S. E. Crawford, Y. Iwakiri, C. Chung, *Cell. Mol. Gastroenterol. Hepatol.* **2015**, *1*, 535.e14.
[232] S. Fumoto, K. Nishimura, K. Nishida, S. Kawakami, *PLoS One* **2016**, *11*, e0148233.
[233] K. Nishimura, S. Fumoto, Y. Fuchigami, M. Hagimori, K. Maruyama, S. Kawakami, *Drug Delivery* **2017**, *24*, 737.
[234] M. Lai, X. Li, J. Li, Y. Hu, D. M. Czajkowsky, Z. Shao, *Acta Biochim. Biophys. Sin.* **2017**, *49*, 465.
[235] M. Y. Gerner, W. Kastenmuller, I. Ifrim, J. Kabat, R. N. Germain, *Immunity* **2012**, *37*, 364.
[236] E. Song, H. Seo, K. Choe, Y. Hwang, J. Ahn, S. Ahn, P. Kim, *Biomed. Opt. Express* **2015**, *6*, 4154.
[237] J. Abe, A. J. Ozga, J. Swoger, J. Sharpe, J. Ripoll, J. V. Stein, *J. Immunol. Methods* **2016**, *431*, 1.
[238] L. K. Dubey, L. Lebon, I. Mosconi, C. Yang, E. Scandella, B. Ludewig, S. A. Luther, N. L. Harris, *Cell Rep.* **2016**, *15*, 1527.
[239] L. K. Dubey, P. Karempudi, S. A. Luther, B. Ludewig, N. L. Harris, *Nat. Commun.* **2017**, *8*, 367.
[240] C. Brede, M. Friedrich, A. Jordán-Garrote, S. S. Riedel, C. A. Bäuerlein, K. G. Heinze, T. Bopp, S. Schulz, A. Mottok, C. Kiesel, K. Mattenheimer, M. Ritz, V. von Krosigk, A. Rosenwald, H. Einsele, R. S. Negrin, G. S. Harms, A. Beilhack, *J. Clin. Invest.* **2012**, *122*, 4439.
[241] V. Kumar, E. Scandella, R. Danuser, L. Onder, M. Nitschké, Y. Fukui, C. Halin, B. Ludewig, J. V. Stein, *Blood* **2010**, *115*, 4725.
[242] P. Rantakari, K. Auvinen, N. Jäppinen, M. Kapraali, J. Valtonen, M. Karikoski, H. Gerke, I. Iftakhar-E-Khuda, J. Keuschnigg, E. Umemoto, K. Tohya, M. Miyasaka, K. Elima, S. Jalkanen, M. Salmi, *Nat. Immunol.* **2015**, *16*, 386.
[243] M. Cabeza-Cabrerizo, J. van Blijswijk, S. Wienert, D. Heim, R. P. Jenkins, P. Chakravarty, N. Rogers, B. Frederico, S. Acton, E. Beerling, J. van Rheenen, H. Clevers, B. U. Schraml, M. Bajénoff, M. Gerner, R. N. Germain, E. Sahai, F. Klauschen, C. R. E Sousa, *Sci. Immunol.* **2019**, *4*, eaaw1941.
[244] L. M. Muramoto, M. E. Kadin, *Am. J. Clin. Pathol.* **1987**, *88*, 589.
[245] A. J. Ozga, F. Moalli, J. Abe, J. Swoger, J. Sharpe, D. Zehn, M. Kreutzfeldt, D. Merkler, J. Ripoll, J. V. Stein, *J. Exp. Med.* **2016**, *213*, 2811.
[246] S. Nojima, E. A. Susaki, K. Yoshida, H. Takemoto, N. Tsujimura, S. Iijima, K. Takachi, Y. Nakahara, S. Tahara, K. Ohshima, M. Kurashige, Y. Hori, N. Wada, J. Ikeda, A. Kumanogoh, E. Morii, H. R. Ueda, *Sci. Rep.* **2017**, *7*, 9269.
[247] M. Hirakawa, D. Nagakubo, B. Kanzler, S. Avilov, B. Krauth, C. Happe, J. B. Swann, A. Nusser, T. Boehm, *Sci. Rep.* **2018**, *8*, 11095.
[248] C. N. Inra, B. O. Zhou, M. Acar, M. M. Murphy, J. Richardson, Z. Zhao, S. J. Morrison, *Nature* **2015**, *527*, 466.
[249] M. Casanova-Acebes, J. A. Nicolás-Ávila, J. L. Li, S. García-Silva, A. Balachander, A. Rubio-Ponce, L. A. Weiss, J. M. Adrover, K. Burrows, N. A-González, I. Ballesteros, S. Devi, J. A. Quintana, G. Crainiciuc, M. Leiva, M. Gunzer, C. Weber, T. Nagasawa, O. Soehnlein, M. Merad, A. Mortha, L. G. Ng, H. Peinado, A. Hidalgo, *J. Exp. Med.* **2018**, *215*, 2778.
[250] C. M. McErlean, J. K. R. Boult, D. J. Collins, M. O. Leach, S. P. Robinson, S. J. Doran, *Microvasc. Res.* **2015**, *101*, 96.
[251] C. Kieffer, M. S. Ladinsky, A. Ninh, R. P. Galimidi, P. J. Bjorkman, *eLife* **2017**, *6*, e23282.
[252] R. Oren, L. Fellus-Alyagor, Y. Addadi, F. Bochner, H. Gutman, S. Blumenreich, H. Dafni, N. Dekel, M. Neeman, S. Lazar, *Sci. Rep.* **2018**, *8*, 1412.
[253] I. Mondor, A. Jorquera, C. Sene, S. Adriouch, R. H. Adams, B. Zhou, S. Wienert, F. Klauschen, M. Bajénoff, *Immunity* **2016**, *45*, 877.
[254] P. Kennel, L. Teyssedre, J. Colombelli, F. Plouraboué, *J. Biomed. Opt.* **2018**, *23*, 1.
[255] E. Lugo-Hernandez, A. Squire, N. Hagemann, A. Brenzel, M. Sardari, J. Schlechter, E. H. Sanchez-Mendoza, M. Gunzer, A. Faissner, D. M. Hermann, *J. Cereb. Blood Flow Metab.* **2017**, *37*, 3355.
[256] J. Epah, K. Pálfi, F. L. Dienst, P. F. Malacarne, R. Bremer, M. Salamon, S. Kumar, H. Jo, C. Schürmann, R. P. Brandes, *Theranostics* **2018**, *8*, 2117.
[257] A. P. D. Giovanna, A. Tibo, L. Silvestri, M. C. Müllenbroich, I. Costantini, A. L. A. Mascaro, L. Sacconi, P. Frasconi, F. S. Pavone, *Sci. Rep.* **2018**, *8*, 12573.
[258] R. Hägerling, D. Drees, A. Scherzinger, C. Dierkes, S. Martin-Almedina, S. Butz, K. Gordon, M. Schäfers, K. Hinrichs, P. Ostergaard, D. Vestweber, T. Goerge, S. Mansour, X. Jiang, P. S. Mortimer, F. Kiefer, *JCI Insight* **2017**, *2*, 16.
[259] L. Richardson, G. Vargas, T. Brown, L. Ochoa, J. Trivedi, M. Kacerovský, M. Lappas, R. Menon, *Placenta* **2017**, *53*, 66.
[260] S. Malki, M. E. Tharp, A. Bortvin, *Biol. Reprod.* **2015**, *93*, 113.
[261] Y. Feng, P. Cui, X. Lu, B. Hsueh, F. Möller Billig, L. Zarnescu Yanez, R. Tomer, D. Boerboom, P. Carmeliet, K. Deisseroth, A. J. W. Hsueh, *Sci. Rep.* **2017**, *7*, 44810.
[262] W. Hu, A. Tamadon, A. J. W. Hsueh, Y. Feng, *J. Visualized Exp.* **2017**, e56141.

[263] K. Kagami, Y. Shinmyo, M. Ono, H. Kawasaki, H. Fujiwara, *Reprod. Biol. Endocrinol.* **2018**, *16*, 72.
[264] K. Kagami, Y. Shinmyo, M. Ono, H. Kawasaki, H. Fujiwara, *Sci. Rep.* **2017**, *7*, 5964.
[265] Z. Vue, G. Gonzalez, C. A. Stewart, S. Mehra, R. R. Behringer, *Mol. Reprod. Dev.* **2018**, *85*, 397.
[266] R. Arora, A. Fries, K. Oelerich, K. Marchuk, K. Sabeur, L. C. Giudice, D. J. Laird, *Development* **2016**, *143*, 4749.
[267] K. Mikolajewicz, G. Chodaczek, *Immunol. Cell Biol.* **2018**, *97*, 104.
[268] M. Frétaud, L. Rivière, É. D. Job, S. Gay, J. Lareyre, J. Joly, P. Affaticati, V. Thermes, *Sci. Rep.* **2017**, *7*, 43012.
[269] N. Tanaka, S. Kanatani, R. Tomer, C. Sahlgren, P. Kronqvist, D. Kaczynska, L. Louhivuori, L. Kis, C. Lindh, P. Mitura, A. Stepulak, S. Corvigno, J. Hartman, P. Micke, A. Mezheyeuski, C. Strell, J. W. Carlson, C. F. Moro, H. Dahlstrand, A. Östman, K. Matsumoto, P. Wiklund, M. Oya, A. Miyakawa, K. Deisseroth, P. Uhlén, *Nat. Biomed. Eng.* **2017**, *1*, 796.
[270] N. Tanaka, D. Kaczynska, S. Kanatani, C. Sahlgren, P. Mitura, A. Stepulak, A. Miyakawa, P. Wiklund, P. Uhlén, *Br. J. Cancer* **2018**, *118*, 995.
[271] M. E. van Royen, E. I. Verhoef, C. F. Kweldam, W. A. van Cappellen, G. Kremers, A. B. Houtsmuller, G. J. L. H. van Leenders, *Histopathology* **2016**, *69*, 985.
[272] E. I. Verhoef, W. A. van Cappellen, J. A. Slotman, G.-J. Kremers, P. C. Ewing-Graham, A. B. Houtsmuller, M. E. van Royen, G. J. L. H. van Leenders, *Histopathology* **2019**, *74*, 1036.
[273] E. I. Verhoef, W. A. van Cappellen, J. A. Slotman, G. Kremers, P. C. Ewing-Graham, A. B. Houtsmuller, M. E. van Royen, G. J. L. H. van Leenders, *Mod. Pathol.* **2019**, *32*, 1032.
[274] C. Barreau, E. Labit, C. Guissard, J. Rouquette, M. Boizeau, S. Gani Koumassi, A. Carrière, Y. Jeanson, S. Berger-Müller, C. Dromard, F. Plouraboué, L. Casteilla, A. Lorsignol, *Obesity* **2016**, *24*, 1081.
[275] S. Altshuler-Keylin, K. Shinoda, Y. Hasegawa, K. Ikeda, H. Hong, Q. Kang, Y. Yang, R. M. Perera, J. Debnath, S. Kajimura, *Cell Metab.* **2016**, *24*, 402.
[276] J. Chi, Z. Wu, C. H. J. Choi, L. Nguyen, S. Tegegne, S. E. Ackerman, A. Crane, F. Marchildon, M. Tessier-Lavigne, P. Cohen, *Cell Metab.* **2018**, *27*, 226.
[277] W. Zeng, R. M. Pirzgalska, M. M. A. Pereira, N. Kubasova, A. Barateiro, E. Seixas, Y. H. Lu, A. Kozlova, H. Voss, G. G. Martins, J. M. Friedman, A. I. Domingos, *Cell* **2015**, *163*, 84.
[278] Y. Cao, H. Wang, Q. Wang, X. Han, W. Zeng, *Mol. Metab.* **2018**, *14*, 71.
[279] B. Lloyd-Lewis, F. M. Davis, O. B. Harris, J. R. Hitchcock, F. C. Lourenco, M. Pasche, C. J. Watson, *Breast Cancer Res.* **2016**, *18*, 127.
[280] F. M. Davis, B. Lloyd-Lewis, O. B. Harris, S. Kozar, D. J. Winton, L. Muresan, C. J. Watson, *Nat. Commun.* **2016**, *7*, 13053.
[281] J. Seong, N. Kim, J. Kim, W. Lee, J. Seo, M. K. Yum, J. Kim, I. Park, J. Kang, S. Bae, C. Yun, Y. Kong, *Development* **2018**, *145*, dev165258.
[282] R. D. Hume, L. Berry, S. Reichelt, M. D'Angelo, J. Gomm, R. E. Cameron, C. J. Watson, *Tissue Eng., Part A* **2018**, *24*, 1309.
[283] B. Lloyd-Lewis, F. M. Davis, O. B. Harris, J. R. Hitchcock, C. J. Watson, *Development* **2018**, *145*, dev164079.
[284] E. Olson, M. J. Levene, R. Torres, *Biomed. Opt. Express* **2016**, *7*, 3089.
[285] D. Unnersjö-Jess, L. Scott, H. Blom, H. Brismar, *Kidney Int.* **2016**, *89*, 243.
[286] C. D. Schuh, M. Polesel, E. Platonova, D. Haenni, A. Gassama, N. Tokonami, S. Ghazi, M. Bugarski, O. Devuyst, U. Ziegler, A. M. Hall, *J. Am. Soc. Nephrol.* **2018**, *29*, 2696.
[287] A. Grüneboom, I. Hawwari, D. Weidner, S. Culemann, S. Müller, S. Henneberg, A. Brenzel, S. Merz, L. Bornemann, K. Zec, M. Wuelling, L. Kling, M. Hasenberg, S. Voortmann, S. Lang, W. Baum, A. Ohs, O. Kraff, H. H. Quick, M. Jäger, S. Landgraeber, M. Dudda, R. Danuser, J. V. Stein, M. Rohde, K. Gelse, A. I. Garbe, A. Adamczyk, A. M. Westendorf, D. Hoffmann, S. Christiansen, D. R. Engel, A. Vortkamp, G. Krönke, M. Herrmann, T. Kamradt, G. Schett, A. Hasenberg, M. Gunzer, *Nat. Metab.* **2019**, *1*, 236.
[288] T. Saritas, V. G. Puelles, X. T. Su, J. A. McCormick, P. A. Welling, D. H. Ellison, *Cell Rep.* **2018**, *25*, 2668.
[289] V. G. Puelles, D. Fleck, L. Ortz, S. Papadouri, T. Strieder, A. Boehner, J. W. van der Wolde, M. Vogt, T. Saritas, C. Kuppe, A. Fuss, S. Menzel, B. M. Klinkhammer, G. Müller-Newen, F. Heymann, L. Decker, F. Braun, O. Kretz, T. B. Huber, E. A. Susaki, H. R. Ueda, P. Boor, J. Floege, R. Kramann, C. Kurts, J. F. Bertram, M. Spehr, D. J. Nikolic-Paterson, M. J. Moeller, *Kidney Int.* **2019**, https://doi.org/10.1016/j.kint.2019.02.034.
[290] J. Huang, C. Brenna, A. ul M. Khan, C. Daniele, R. Rudolf, V. Heuveline, N. Gretz, *Sci. Rep.* **2019**, *9*, 521.
[291] Y. Tanaka, A. Kubota, M. Yamato, T. Okano, K. Nishida, *Biomaterials* **2011**, *32*, 1080.
[292] Y. Tanaka, D. Shi, A. Kubota, Y. Takano, N. Fuse, M. Yamato, T. Okano, K. Nishida, *Biomaterials* **2011**, *32*, 6764.
[293] J. N. Singh, T. M. Nowlin, G. J. Seedorf, S. H. Abman, D. P. Shepherd, *J. Biomed. Opt.* **2017**, *22*, 076011.
[294] B. Hohberger, C. Baumgart, A. Bergua, *Eye* **2017**, *31*, 1496.
[295] Y. Henning, C. Osadnik, E. P. Malkemper, *Exp. Eye Res.* **2019**, *180*, 137.
[296] S. Kim, J. Assawachananont, *Transl. Vision Sci. Technol.* **2016**, *5*, 6.
[297] V. Pernet, S. Joly, N. Jordi, D. Dalkara, A. Guzik-Kornacka, J. G. Flannery, M. E. Schwab, *Cell Death Dis.* **2013**, *4*, e734.
[298] X. Luo, Y. Salgueiro, S. R. Beckerman, V. P. Lemmon, P. Tsoulfas, K. K. Park, *Exp. Neurol.* **2013**, *247*, 653.
[299] E. R. Bray, M. Noga, K. Thakor, Y. Wang, V. P. Lemmon, K. K. Park, P. Tsoulfas, *eNeuro* **2017**, *4*, ENEURO.0093.
[300] B. J. Yungher, X. Luo, Y. Salgueiro, M. G. Blackmore, K. K. Park, *Gene Ther.* **2015**, *22*, 811.
[301] G. D. Scott, E. D. Blum, A. D. Fryer, D. B. Jacoby, *Am. J. Respir. Cell Mol. Biol.* **2014**, *51*, 43.
[302] M. Snitow, M. Lu, L. Cheng, S. Zhou, E. E. Morrisey, *Development* **2016**, *143*, 3733.
[303] T. Watanabe, R. Nakamura, Y. Takase, E. A. Susaki, H. R. Ueda, R. Tadokoro, Y. Takahashi, *Dev. Biol.* **2018**, *444*, S325.
[304] M. R. Cronan, A. F. Rosenberg, S. H. Oehlers, J. W. Saelens, D. M. Sisk, K. L. Jurcic Smith, S. Lee, D. M. Tobin, *Dis. Models Mech.* **2015**, *8*, 1643.
[305] B. von Neubeck, G. Gondi, C. Riganti, C. Pan, A. P. Damas, H. Scherb, A. Ertürk, R. Zeidler, *Int. J. Cancer* **2018**, *143*, 2065.
[306] N. S. Joshi, E. H. Akama-Garren, Y. Lu, D. Lee, G. P. Chang, A. Li, M. DuPage, T. Tammela, N. R. Kerper, A. F. Farago, R. Robbins, D. M. Crowley, R. T. Bronson, T. Jacks, *Immunity* **2015**, *43*, 579.
[307] F. Saboor, A. N. Reckmann, C. U. M. Tomczyk, D. M. Peters, N. Weissmann, A. Kaschtanow, R. T. Schermuly, T. V. Michurina, G. Enikolopov, D. Müller, A. Mietens, R. Middendorff, *Eur. Respir. J.* **2016**, *47*, 876.
[308] D. T. Mzinza, H. Fleige, K. Laarmann, S. Willenzon, J. Ristenpart, J. Spanier, G. Sutter, U. Kalinke, P. Valentin-Weigand, R. Förster, *Cell Mol. Immunol.* **2018**, *15*, 875.
[309] L. F. Ochoa, A. Kholodnykh, P. Villarreal, B. Tian, R. Pal, A. N. Freiberg, A. R. Brasier, M. Motamedi, G. Vargas, *Sci. Rep.* **2018**, *8*, 13348.
[310] L. Yang, A. Feuchtinger, W. Möller, Y. Ding, D. Kutschke, G. Möller, J. C. Schittny, G. Burgstaller, W. Hofmann, T. Stoeger, Daniel Razansky, A. Walch, O. Schmid, *ACS Nano* **2019**, *13*, 1029.
[311] K. Togami, A. Kitayama, T. Daisho, R. Wang, H. Tada, S. Chono, *Biol. Pharm. Bull.* **2018**, *41*, 24.

[312] M. Kellner, M. Heidrich, R. Lorbeer, G. C. Antonopoulos, L. Knudsen, C. Wrede, N. Izykowski, R. Grothausmann, D. Jonigk, M. Ochs, T. Ripken, M. P. Kühnel, H. Meyer, *Sci. Rep.* **2016**, *6*, 35606.
[313] J. Woo, M. Lee, J. M. Seo, H. S. Park, Y. E. Cho, *Exp. Mol. Med.* **2016**, *48*, e274.
[314] H. Lee, J. Park, I. Seo, S. Park, S. Kim, *BMC Dev. Biol.* **2014**, *14*, 48.
[315] S. Sindhwani, A. M. Syed, S. Wilhelm, D. R. Glancy, Y. Y. Chen, M. Dobosz, W. C. W. Chan, *ACS Nano* **2016**, *10*, 5468.
[316] E. Lee, J. Choi, Y. Jo, J. Y. Kim, Y. J. Jang, H. M. Lee, S. Y. Kim, H. Lee, K. Cho, N. Jung, E. M. Hur, S. J. Jeong, C. Moon, Y. Choe, I. J. Rhyu, H. Kim, W. Sun, *Sci. Rep.* **2016**, *6*, 18631.
[317] L. Bozycki, K. Łukasiewicz, P. Matryba, S. Pikula, *Skeletal Muscle* **2018**, *8*, 21.
[318] M. D. Rocha, D. N. Düring, P. Bethge, F. F. Voigt, S. Hildebrand, F. Helmchen, A. Pfeifer, R. H. R. Hahnloser, M. Gahr, *Front. Neuroanat.* **2019**, *13*, 2.
[319] D. N. Düring, M. D. Rocha, F. Dittrich, M. Gahr, R. H. R. Hahnloser, *Front. Neuroanat.* **2019**, *13*, 2.
[320] M. E. Boutin, T. C. Voss, S. A. Titus, K. Cruz-Gutierrez, S. Michael, M. Ferrer, *Sci. Rep.* **2018**, *8*, 11135.
[321] M. E. Boutin, D. Hoffman-Kim, *Tissue Eng., Part C* **2015**, *21*, 292.
[322] D. Kurihara, Y. Mizuta, Y. Sato, T. Higashiyama, *Development* **2015**, *142*, 4168.
[323] W. M. Palmer, A. P. Martin, J. R. Flynn, S. L. Reed, R. G. White, R. T. Furbank, C. P. L. Grof, *Sci. Rep.* **2015**, *5*, 13492.
[324] A. Konno, S. Okazaki, *Zool. Lett.* **2018**, *4*, 13.
[325] M. Smolla, M. Ruchty, M. Nagel, C. J. Kleineidam, *Arthropod Struct. Dev.* **2014**, *43*, 175.
[326] G. McConnell, W. B. Amos, *J. Microsc.* **2018**, *270*, 252.
[327] Y. Yi, Y. Men, D. Jing, W. Luo, S. Zhang, J. Q. Feng, J. Liu, W. Ge, J. Wang, H. Zhao, *Cell Proliferation* **2019**, *0*, e12578.
[328] P. Höök, T. Brito-Robinson, O. Kim, C. Narciso, H. V. Goodson, J. W. Weisel, M. S. Alber, J. J. Zartman, *Biomed. Opt. Express* **2017**, *8*, 3671.
[329] W. H. DePas, R. Starwalt-Lee, L. Van Sambeek, S. Ravindra Kumar, V. Gradinaru, D. K. Newman, *mBio* **2016**, *7*, e00796.
[330] J. Bulantová, T. Macháček, L. Panská, F. Krejčí, J. Karch, N. Jährling, S. Saghafi, H. Dodt, P. Horák, *Micron* **2016**, *83*, 62.
[331] T. Mori, M. Hirai, T. Mita, *Sci. Rep.* **2019**, *9*, 1768.
[332] Y. Cui, X. Wang, W. Ren, J. Liu, J. Irudayaraj, *ACS Nano* **2016**, *10*, 3132.
[333] J. H. Kim, M. J. Jang, J. Choi, E. Lee, K. Song, J. Cho, K. Kim, H. Cha, W. Sun, *Sci. Rep.* **2018**, *8*, 12815.
[334] K. Vints, D. Vandael, P. Baatsen, B. Pavie, F. Vernaillen, N. Corthout, V. Rybakin, S. Munck, N. V. Gounko, *Sci. Rep.* **2019**, *9*, 130.
[335] M. S. Kassem, S. Y. Y. Fok, K. L. Smith, M. Kuligowski, B. W. Balleine, *J. Neurosci. Methods* **2018**, *294*, 102.
[336] T. Liebmann, N. Renier, K. Bettayeb, P. Greengard, M. Tessier-Lavigne, M. Flajolet, *Cell Rep.* **2016**, *16*, 1138.
[337] P. Wan, J. Zhu, J. Xu, Y. Li, T. Yu, D. Zhu, *Neurophotonics* **2018**, *5*, 035007.
[338] J. Xu, Y. Ma, T. Yu, D. Zhu, *J. Biophotonics* **2018**, *0*, e201800134.
[339] G. D. P. Bossolani, I. Pintelon, J. D. Detrez, R. Buckinx, S. Thys, J. N. Zanoni, W. H. D. Vos, J. Timmermans, *Neurogastroenterol. Motil.* **2019**, *31*, e13560.